


Spring 2011

# Triple Coincidence Beam Spin Asymmetry Measurements in Deeply Virtual Compton Scattering

Mustafa Canan  
*Old Dominion University*

Follow this and additional works at: [https://digitalcommons.odu.edu/physics\\_etds](https://digitalcommons.odu.edu/physics_etds)

 Part of the [Elementary Particles and Fields and String Theory Commons](#), and the [Nuclear Commons](#)

---

## Recommended Citation

Canan, Mustafa. "Triple Coincidence Beam Spin Asymmetry Measurements in Deeply Virtual Compton Scattering" (2011). Doctor of Philosophy (PhD), dissertation, Physics, Old Dominion University, DOI: 10.25777/hnp4-k963  
[https://digitalcommons.odu.edu/physics\\_etds/36](https://digitalcommons.odu.edu/physics_etds/36)

This Dissertation is brought to you for free and open access by the Physics at ODU Digital Commons. It has been accepted for inclusion in Physics Theses & Dissertations by an authorized administrator of ODU Digital Commons. For more information, please contact [digitalcommons@odu.edu](mailto:digitalcommons@odu.edu).

TRIPLE COINCIDENCE BEAM SPIN ASYMMETRY  
MEASUREMENTS IN DEEPLY VIRTUAL COMPTON  
SCATTERING

by

Mustafa Canan  
B.S. June 2003, Middle East Technical University  
M.S. May 2006, Old Dominion University


A Dissertation Submitted to the Faculty of  
Old Dominion University in Partial Fulfillment of the  
Requirement for the Degree of

DOCTOR OF PHILOSOPHY


PHYSICS

OLD DOMINION UNIVERSITY  
May 2011

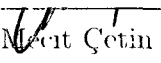
Approved by:

  
Charles E. Hyde (Director)

  
Anatoly Radyushkin

  
Moskov Amarvan

  
Svetlana Ponedvic

  
Mehmet Cetin

## ABSTRACT

# TRIPLE COINCIDENCE BEAM SPIN ASYMMETRY MEASUREMENTS IN DEEPLY VIRTUAL COMPTON SCATTERING

Mustafa Canan

Old Dominion University, 2011

Director: Dr. Charles E. Hyde

The Generalized Parton Distributions (GPDs) provides hitherto the most complete information about the quark structure of hadron. GPDs are accessible through hard-exclusive reactions, among which Deeply Virtual Compton Scattering (DVCS) is the cleanest reaction. A dedicated DVCS experiment on Hydrogen (E00-110) ran in the Hall A at Jefferson Laboratory in Fall 2004. I present here Beam Spin Asymmetry (BSA) results for the  $ep \rightarrow ep\gamma$  reaction studied in the E00-110 experiment with fully exclusive triple coincidence  $H(e, e'\gamma p)$  detection. I present a re-calibration of the electromagnetic calorimeter used to detect the high energy photon. This calibration is necessary to account for the effects of pile-up. The results show a 1-sigma disagreement with the double coincidence  $H(e, e'\gamma)p$  results, I also presents a feasibility study for measurements of neutron GPDs via the  ${}^3\overline{H}e^\uparrow(e, e'\gamma)ppn$  reaction on a polarized  ${}^3He$  target with JLab at 12 GeV. These measurements offer the prospect of a determination of all four GPDs.

©Copyright, 2011, by Mustafa Canan, All Rights Reserved

## ACKNOWLEDGMENTS

This dissertation would not have been possible without the guidance and the help of several individuals who in one way or another contributed and extended their valuable assistance in the preparation and completion of this study.

I would like to express my deepest gratitude to my advisor, Dr. Charles E. Hyde for his excellent guidance, patience and providing me comfortable atmosphere to conduct research. I would like to thank Dr. Carlos Munoz Camacho for his helps about softwares, experimental setup and any question related to DVCS experiment. I would like to thank Dr. Gagik Gavalian for his C++ guidance.

I would like thank my committee members Dr. Anatoly Radyushkin, Dr. Moskov Amaryan, Dr. Svetozar Popovic, Dr. Mecit Cetin for their patience, guidance and contributions to my thesis.

I would like to thank members of Turkish Community in Hampton Roads especially Dr. Serkan Golge, Dr. Bedri Yagiz, Dr. Mehdi Koklu, Dr. Iliteris Koc, Ibrahim Albayrak, Oguz Er, Mehmet Unlu for the great times that we shared over the years in Hampton Roads.

Any attempt to thank my brother-in-law Dr. Salim Balik, his wife Meral Balik and their daughters Hilal and Neval Balik will be inadequate. The life in abroad with them became a life similar to Turkiye.

Whatever I do to thank my parents H. Gulsen Canan, Mehmet Canan and my brother Mehmedali Canan, it will not be an adequate acknowledgement for them. Being away from them has been difficult however, being away from their son/brother must have been more difficult. Their spiritual support was the “backbone” for my studies since early childhood.

Finally, my infinite gratitude and thanks to my wife Yeter Canan and my daughter Zeynep Canan. Yeter has been source of re-motivation and the source of forgetting any demoralizing incidents. With out her support I would not be able to complete this work. For the last 17 months, my daughter Zeynep has been the joy and happiness for me so that her support was matchless.

## TABLE OF CONTENTS

	Page
List of Tables . . . . .	viii
List of Figures . . . . .	xix
 Chapter	
I Introduction . . . . .	1
II Physics Motivation . . . . .	5
II.1 The Probing Phenomenology . . . . .	5
II.2 Elastic Scattering: Electromagnetic Form Factors . . . . .	7
II.3 Deep Inelastic Scattering: Parton Distributions . . . . .	9
II.3.1 Structure Functions . . . . .	10
II.3.2 Hard Scattering Reactions and Factorization . . . . .	12
II.4 Generalized Parton Distributions (GPDs) . . . . .	16
II.4.1 From Compton Amplitude to GPDs . . . . .	16
II.4.2 GPD Kinematical Variables . . . . .	18
II.4.3 Characteristics of GPDs . . . . .	19
II.5 Phenomenology of GPDs . . . . .	22
II.5.1 Deeply Virtual Compton Scattering . . . . .	25
II.5.2 Cross Section for the Electroproduction of the Photon . . . . .	26
II.5.3 Beam Spin Asymmetry (BSA) . . . . .	29
III Experimental Studies on DVCS . . . . .	32
III.1 Collider Experiments . . . . .	32
III.2 Fixed-Target Experiments . . . . .	32
III.3 DVCS at JLab . . . . .	34
III.3.1 Hall A DVCS Program . . . . .	34
III.3.2 CLAS DVCS Program . . . . .	37
III.4 Future of DVCS Measurements . . . . .	38
III.4.1 Jefferson Lab 12 GeV . . . . .	38
III.4.2 DVCS Measurements with Higher Beam Energies . . . . .	40
IV Experimental Setup . . . . .	42
IV.1 CEBAF at Jefferson Lab . . . . .	42
IV.2 Experimental Hall A . . . . .	44
IV.2.1 High Resolution Spectrometers . . . . .	45
IV.2.2 Beamline Instrumentation . . . . .	46
IV.2.3 The Target System . . . . .	54
IV.2.4 Dedicated DVCS Detectors . . . . .	56
IV.2.5 Data Acquisition . . . . .	63
V DVCS Monte Carlo Simulation . . . . .	76
V.1 Overview of the DVCS Simulation . . . . .	76
V.2 Generation of Scattered Electron Events . . . . .	77
V.3 Generation of Hadronic Reaction Events . . . . .	77

VI	HRS and Calorimeter Waveform Analysis . . . . .	79
VI.1	Hall A HRS Data Analysis . . . . .	79
VI.1.1	VDC analysis: Tracking and Reconstruction . . . . .	79
VI.1.2	Optics Design, Momentum and Vertex reconstruction . . . . .	80
VI.2	Waveform Algorithm . . . . .	83
VI.2.1	The Amplitude of the Ideal Case . . . . .	83
VI.2.2	Real Case Implementations . . . . .	84
VI.2.3	One-Pulse fit . . . . .	85
VI.2.4	Multi-Pulse Fit . . . . .	85
VI.3	Electromagnetic Calorimeter . . . . .	86
VI.3.1	Vertex Position Reconstruction . . . . .	86
VI.3.2	Clustering Algorithm . . . . .	87
VI.4	Proton Array . . . . .	88
VII	Data Analysis . . . . .	92
VII.1	Kinematic Settings . . . . .	92
VII.2	Global Calibration of Detectors . . . . .	92
VII.2.1	HRS Calibration . . . . .	92
VII.2.2	Calorimeter Calibration . . . . .	94
VII.2.3	Proton Array . . . . .	98
VII.3	Selection of Electron Events . . . . .	102
VII.3.1	Electron Identification . . . . .	102
VII.3.2	Electron Events Cuts . . . . .	102
VII.4	Selection of Photon Events . . . . .	105
VII.4.1	Clustering Time Window . . . . .	105
VII.4.2	Geometrical Acceptance of Calorimeter . . . . .	106
VII.5	Selection of Proton Events . . . . .	109
VII.5.1	Photon Energy Exclusivity Re-Normalization and Proton Prediction . . . . .	109
VII.5.2	Energy Threshold . . . . .	111
VII.5.3	Background and Accidentals . . . . .	113
VII.5.4	Missing Mass Squared Study . . . . .	116
VII.6	$M_X^2$ in Electromagnetic Calorimeter . . . . .	123
VII.7	Re-Calibration . . . . .	126
VII.7.1	Re-Normalization Factor . . . . .	127
VII.7.2	Re-Normalization . . . . .	129
VII.7.3	Smearing . . . . .	130
VIII	Results and Discussion . . . . .	133
VIII.1	Results . . . . .	133
VIII.2	Discussion . . . . .	135
VIII.3	VGG calculation of BSA . . . . .	139
IX	Polarized DVCS Observables . . . . .	145
IX.1	Cross Sections with Polarized and Angular Dependence . . . . .	145
IX.1.1	Interference of Bethe-Heitler and DVCS Amplitudes . . . . .	145
IX.1.2	Angular Harmonics in terms of GPDs . . . . .	147

IX.2	VGG Calculation of GPDs . . . . .	148
IX.2.1	Kinematics . . . . .	151
IX.3	Results . . . . .	152
IX.3.1	Cross Sections . . . . .	152
IX.3.2	Difference in Cross Section . . . . .	152
IX.3.3	Discussion . . . . .	156
X	Summary . . . . .	161
VITA	. . . . .	170



## LIST OF TABLES

	Page
1	Three kinematical settings of the E00-110 experiment. Three different $Q^2$ settings were chosen aiming to maximize the highest $Q^2$ value and $Q^2$ range which keeps above the main resonance. . . . . 37
2	Calorimeter waveform analysis parameters. $\chi^2$ of the fit computed in a 40 ns window which is centered around the minimum of the pulse though pulses were searched in a 45 ns time window (See Fig.55) . . . 86
3	Proton Array waveform analysis parameters. Raw ARS data was analyzed with the same algorithm as in the case for calorimeter, however as it can be seen the parameters are different. $\chi^2$ of the fit computed in a 40 ns window which is centered around the minimum of the pulse and different than the calorimeter case, the pulses were searched in 40 ns time window. . . . . 90
4	Fit parameters of Eq.(139) for $H(e, e'\gamma p)$ events with detected proton in the exclusive predicted block. . . . . 140
5	Fit parameters of Eq.(139) for $H(e, e'\gamma p)$ events in the group of nine. 140
6	Fit parameters of Eq.(139) for $H(e, e'\gamma)X$ events with the proton prediction in core region of proton array. . . . . 140
7	Kinematics for VGG calculation of polarized DVCS observables. Calculation is performed for each kinematics for two different $t$ values shown in table. Besides, for each kinematical settings calculations are repeated for different $J_u$ and $J_d$ values. . . . . 151

## LIST OF FIGURES

		Page
1	Increasing the resolution by increasing the $Q^2$ , (changing the virtuality of the photon) yields different pictures of the proton. As illustrated, in this case of $Q_2^2 > Q_1^2$ , one can see quark structure and coherent proton respectively with these two different $Q^2$ values. For example, at Jefferson Lab, by using associated wavelength $\lambda = \frac{\hbar c}{q}$ which allows to probe $10^{-16}$ meter with a $Q^2 = 1\text{GeV}^2$ . . . . .	6
2	Elastic scattering of an electron from a nucleon through one-photon exchange. Here in this illustration, $k_i$ is the four momenta of incoming electron beam, $k_f$ is the four momenta of the scattered electron, and $\gamma^*$ is the exchange virtual photon carries the four momentum transfer $q$ .	8
3	Illustration of a typical inclusive Deep-Inelastic Scattering event in which an incident electron transfers momentum $q$ to the target and the hadronic final states, $X$ , are not distinguished. DIS is an inclusive reaction which only the scattered electron is detected. DIS can be restricted on single-photon exchange as a result of the fact that the electromagnetism in this reaction dynamics is very weak in contrast to strong interactions. . . . .	9
4	Hadronic tensor of the deep inelastic scattering cross section determining the imaginary part of the forward Compton Scattering amplitude $\gamma^*(q)N(p) \rightarrow \gamma^*(q)N(p)$ . . . . .	13
5	Handbag diagram for the forward Compton Scattering. With the absorption of virtual photon, at $t=0$ , a quark taken out from hadron as a result it accelerates, then re-emits another virtual photon, at a later time $t > 0$ , then decelerates and acquires same initial momentum state. The point of absorption and emission are separated by a light like distance. . . . .	14
6	Handbag diagram for Deeply Virtual Compton Scattering. Factorization of the $\gamma^*p \rightarrow \gamma p$ DVCS amplitude in the Bjorken limit of large $Q^2$ and $t \ll Q^2$ . In this exclusive process, the virtual photon interacts with a quark of momentum fraction $x + \xi$ and goes back in to the nucleon with a different momentum $x - \xi$ . This change in longitudinal momentum occurs as a result of the momentum transfer $\Delta$ and the emission of real photon. . . . .	19
7	Illustration of the encoded physics in GPDs in impact parameter space. DVCS probes partons at transverse position $\mathbf{b}$ , with the initial and final proton state proton localized around zero but shifted relative to each other by $2\xi\mathbf{b}/(1 - \xi^2)$ case. This picture is the representation of $\xi$ region of $\xi <  x  < 1$ which gives the location where a quark or an anti-quark is pulled out of and put back into the proton. . . . .	23
8	Electro-production of real photon $ep \rightarrow ep\gamma$ . . . . .	24

9	Illustration of one particular GPD model [32, 33] for the GPD $H$ as a function of $x$ and $\xi$ for $t = 0$ . One identifies at $\xi = 0$ a standard quark density distribution, with the rise around $x = 0$ corresponding to the diverging sea quark contribution and the negative $x$ part is related to anti-quarks. It is seen that the evolution with $\xi$ is not trivial and that measuring the integral over $x$ of a GPD, at constant $\xi$ will not define it uniquely.(Figure is taken from [32]) . . . . .	27
10	Kinematics of Electroproduction of Real Photon in the target rest frame. The three momentum of the virtual photon ( $\gamma^*$ ) is along the $z$ -direction. The lepton three momenta form the leptonic scattering plane, while the recoiled proton and outgoing real photon define the hadronic scattering plane. In this reference system the azimuthal angle between the leptonic plane and the recoiled proton is $\phi$ . . . . .	31
11	$Q^2$ -depdence of the differential $\gamma^*p \rightarrow \gamma p$ cross section measured by H1 and ZEUS. In addition to the H1 and ZEUS data, the solid curve shows NLO $pQCD$ calculation using a GPD parametrization based on MRST2001 PDFs and a $Q^2$ dependent $t$ -slope $b(Q^2)$ describing the factorized $t$ -dependence [58]. . . . .	33
12	The $\phi_{\gamma\gamma}$ dependent BSA measurements performed at HERMES [56] and CLAS [57]. Since the charge of the lepton beams used in these two facilities were opposite, the opposite sign in BSA is observed. GPD models [59, 60] have been overlayed (solid lines) and show that theory and data are in good agreement. Dashed lines show a phenomenological fit to the data [61]. . . . .	33
13	CLAS longitudinal target spin asymmetry [69]. The experiment performed for average kinematics of $\langle Q^2, x_B, t \rangle = (1, 82 \text{ GeV}^2, 0.16, -0.31 \text{ GeV}^2)$ . The solid curve is a fit to the data. The dashed and dotted curves are from $\xi$ -dependent VGG model with $E = 0$ and $\tilde{E} = 0$ . The dotted curve includes only H. The dashed curve includes both $H$ and $\tilde{H}$ . . . . .	35
14	Helicity dependent (top) and independent (bottom) cross section at $Q^2 = 2.3 \text{ GeV}^2$ for the Hall A DVCS. The values of $-t$ from right to left 0.17, 0.23, 0.28, and $0.33 \text{ GeV}^2$ . Each distribution is fitted with the form of Eq.(59).[70] . . . . .	35
15	Imaginary part of the effective interference term $C_{ump}^I$ extracted from the helicity dependent data of Fig.(14). . . . .	36
16	Experimental constraints on the total up and down quark contributions to the proton spin. JLab Hall A Neutron experiment [73] and HERMES transversely polarized proton [63]. The theory/model values displayed [75, 76, 77, 78, 79] respectively as listed in the figure. . . . .	36
17	Beam spin asymmetry $\sin(\phi_{\gamma\gamma})$ moment from the CLAS DVCS experiment [80] . . . . .	39
18	Kinematics coverage for fixed target experiments.COMPASS at 190 GeV, HERMES 27.6 GeV, JLab 6 GeV (now), with upgrade 11 GeV. . . . .	40

19	Continuous Electron Beam Facility at JLab The electron beam is produced at the injector by illuminating a photo-cathode and then accelerated to 60 MeV. The beam is then further accelerated in North and South linacs. . . . .	43
20	Experimental Hall A . . . . .	44
21	Side-view the most frequently used individual elements of the detector system are indicated in the configuration. The position DAQ of each detector package, VDC support frame, and the S1, Črenkov, S2 plates relative positions are drawn. . . . .	47
22	Schematic top view of experimental Hall A, indicating the location of Compton and Møller polarimeters, the beam current monitors (BCM) and the beam position monitors (BPM) upstream of the target. In addition to beam line components, the locations of the components of one the high-resolution spectrometers (Q1, Q2, dipole, Q3 and the shield house), the beam dump and the truck access ramp are indicated.	48
23	Schematic layout of the Compton polarimeter at Hall, A showing the four dipoles of the chicane, the optical cavity, and the photon and the electron detectors. . . . .	51
24	Top and side view of the Møller polarimeter at Hall A. The trajectories displayed belong to a simulated event of Møller scattering at $\theta_{CM}=80^\circ$ and $\phi_{CM} = 0^\circ$ at a beam energy of 4 GeV. . . . .	51
25	Top view of Experimental Hall A, showing the location of the scintillator array (proton array), the electromagnetic calorimeter, L-HRS, and scattering chamber. The R-HRS is not shown, and it is parked at a large angle. The support frame for both detectors is not shown. . . .	57
26	Backside view of Calorimeter layout, showing the XY table, which functions as LED carrier, the mechanical system to control the motion of LED system and the cable tray . . . . .	59
27	Correlation between $\theta_{\gamma\gamma^*}$ and $\theta_{\gamma^*p}$ is shown for the $Q^2$ values of 2.5 $GeV^2$ , 2.0 $GeV^2$ , 1.5 $GeV^2$ for $x_B = 0.35$ . $\theta_{\gamma\gamma^*}$ is the angle between emitted photon and the virtual photon $\theta_{\gamma^*p}$ is the angle between the virtual photon and the recoil proton. The experimental acceptance for $\theta_{\gamma^*p}$ the can be seen in Fig. 28 . . . . .	60
28	The Experimental Acceptance for Proton Array and $\theta_{\gamma^*p}^{lab}$ is the angle between virtual photon and recoil proton in lab frame . . . . .	61
29	Proton Array with Scattering Chamber. Relative position of the proton array to the scattering chamber and the L-HRS. The exit beam pipe, not shown here, is in between PA and L-HRS. . . . .	62
30	Proton array consists of 20 towers and each towers is combination of 5 scintillator blocks and PMTs at the end. Here single PA tower is shown. Each tower covers $13.5^\circ$ in azimuthal angle ( $\phi$ ) and each scintillator block covers $4^\circ$ in polar angle ( $\theta$ ). . . . .	63

31	The compact design that can be seen in Fig. 29 ensues the condition of being in direct view of target, and being exposed to the radiation effect from the beamline. As it can be seen here, radiation effects can highly be observed in first 3 or 4 towers from each end of the PA. Although the radiation doesn't effect the all 5 blocks, it is major issue for the closest towers. One immediate consequences of beam pipe radiation in this triple coincidence analysis is that we removed the two towers in both ends of the PA (will be explained in the coming chapters). In this analysis, a new calibration of the calorimeter performed and it is shown that the beam pipe radiation effects are not negligible for the calorimeter blocks closer to the beam pipe. . . . .	64
32	The Schematic view of the scattering chamber, proton array, calorimeter, Big Bite stand along with beam line. The Big Bite stand which was used for as DVCS stand allowed the circular motion of the DVCS detectors with precise adjustment of the desired kinematical angles. . . . .	65
33	Typical waveform recorded by an ARS channel, yielding two pulses. A waveform analysis is performed to get the information about the two separate pulses. . . . .	67
34	AC coupled signal in different blocks. Depending on the position of the block,the behavior of signal varies as can be seen in this example. The block zero is in the far edge of the calorimeter from the beamline. On the other hand the block 126 is in the closest column to the beamline.	71
35	Basic schema of the DVCS trigger module [98]. The HRS trigger is generated by the coincidence between S1 and S2m and the signal to trigger the calorimeter ADC integration is generated based on the coincidence between Čerenkov and S2m. Since both coincidences include the s2m, both cases have the same time reference. Here is the S2m is an upgraded version of the standard S2. S2m provides improved timing resolution. The significant feature of this custom trigger module is the coincidence trigger between the HRS trigger and the Calorimeter Trigger. In the case of no coincidence, none of the ARS channel needs to be read, it takes about 500 ns to get the DAQ ready for the new event. When the ARS is read out, DAQ will be busy for about 128 $\mu s$ .	72
36	Calorimeter block numbers and an example of two overlapping 4 blocks clusters. After the digitization of each individual calorimeter block by using a 7 bit Fast ADC, the pedestals are subtracted. Then, all the sums of the 4 adjacent blocks are computed. . . . .	73

37	The digitized ADC values in each 4 adjacent block set are computed and to a threshold. During the experiment, substantial amount of data were taken with a threshold of 57 ADC channels which corresponds to an energy value of 1 GeV. ARSs with energy higher than threshold area recorded. A typical result of computed ADC channels is shown here in the solid line box where each 9 blocks in the box shows the result of ADC integration. Here in this event 4 overlapping 4 adjacent blocks formed a calorimeter tower, having the block in the center with an ADC value of 41. As it can be seen in this event, no individual block has a higher ADC value than threshold, and this is typical example of showering. In this case of having individual threshold for each block, the accurate information for deposited energy, for instance, from the photon of this particular $e\gamma$ might be garbage. . . . .	74
38	Proton Array Blocks Projected to Calorimeter Towers The back view of the calorimeter towers and the proton array, the beam is on the right hand side. There are 132 blocks in the calorimeter, however, the number of towers is 110. Left edge bottom corner tower is tower number 0, and the right edge upper corner tower is tower number 109. The symmetric direction of the emitted photon and the recoil proton with respect to the virtual photon can be seen here. For example, while the tower is the left bottom corner, the predicted position where proton would hit is right upper corner of the proton array. Because of the geometry of proton array the projected proton array events in the blocks located on the left hand side are very few. . . . .	75
39	Target coordinate system, L is the distance from the Hall center to the HRS sieve plane, while D is the horizontal displacement of the spectrometer axis from its ideal position. Spectrometer central angle is denoted by $\Theta_0$ . Note that $x_{tg}$ is vertically down (in to the page). . . . .	83
40	Illustration of the cellular automata procedure. At every step each cell takes the value of its highest energy neighbor. When a cell gets the value of one of the local maximum first determined, it does not change anymore. At the end the process, all cells with the same value form a cluster. . . . .	89
41	Calorimeter ARS wave form analysis for kinematics 3. The number of pulses fit presented here as an average over the whole calorimeter. As consequence of higher backgrounds the blocks closer to the beam line have higher number of pulses fit. . . . .	90
42	Proton array ARS wave form analysis for kinematics 3. The number of pulses fit presented here as average over the whole detector. As consequence of higher backgrounds the blocks closer to the beam line have higher number of pulses fit. . . . .	91

43	Top: angle between the virtual photon and the electron beam as a function of $x_B$ ; curves for constant $Q^2$ and constant $s$ are plotted. Bottom: scattered electron momentum magnitude as a function of the scattering angle; curves for constant $Q^2$ , constant $s$ and constant $x_B$ are also plotted. Shadowed zones in both figures corresponds to experimental constraints.(Figures are taken from [61]) . . . . .	93
44	TDC corrected time for two different bunches of 16 wires of one VDC plane, before (top) and after (bottom) the offsets optimization. The TDC offset observed in the upper plot is corrected after the optimization.(Figure taken from [61]) . . . . .	94
45	Cross calibration with cosmic data. The dispersion distribution width is 2.7 % of its mean. . . . .	96
46	Calorimeter cross-calibration as measured by LEDs for the HV calculated with cosmic runs. . . . .	97
47	Left plot is the proton momentum versus the scattering angle for each elastic settings. Cuts applied to select elastic events are shown in red. The corresponding impact point on the calorimeter is showwn in the right plot. . . . .	98
48	Energy resolution obtained in both elastic calibration: 2.4%, the average energy of the incident electron is 4.2. GeV. The results of the second calibration when first calibration coefficients are used are also plotted to show the necessity of a careful monitoring of the coefficients between these two calibration points. . . . .	99
49	Deposited energy versus momentum distribution generated by using the kinematics 3 of E-00110 experiment. Each plot consists of two proton array blocks: 41 & 46 outer lane blocks, 42 & 47 middle lane blocks and 43 & 48 inner lane blocks of the core region of the proton array. (See Fig. 60) . . . . .	100
50	Simulated light and momentum in Proton Array . . . . .	101
51	Measured energy versus predicted proton momentum for all proton array blocks after the calibration performed. . . . .	101
52	Measured energy versus predicted energy for proton array block number 53 after the calibration performed. . . . .	102
53	Distribution of the sum of all Čerenkov mirrors, for each kinematic settings. The first peak in this distribution corresponds to 1-photoelectron signal due to the electronic noise. In order remove this contamination a Čerenkov cut is applied at Čerenkov sum value of 150 ADC. . . . .	103
54	The upper figure illustrates the resolution of the vertex reconstruction on a multi-foil target. The bottom figure illustrates the central foil fit leads to $\sigma=1.9$ mm. The foil thickness is 1mm and the HRS was at $37.69^\circ$ during this run. The measured $\sigma$ at this angle is 1.87 mm that means a $\sigma$ value of 1.2 mm at $90^\circ$ . Therefore, the introduced $\sigma$ value of $1/\sqrt{12}$ for foil thickness can be ignored. . . . .	104

55	The 45 ns time window of the waveform analysis for the calorimeter blocks in kinematic 3 with $E > 300\text{MeV}$ . Here in this plot the coincidence [-3.3] time window used for clustering is shown by solid lines. The time resolution is 0.6 ns. . . . .	105
56	Number of calorimeter clusters in the coincidence time window for kinematics 3. . . . .	106
57	Simulated triple coincidence events in corresponding calorimeter towers. The nature of the triple coincidence particle detection in E00-110 experiment causes the fact that not all DVCS photons, detected in the electromagnetic calorimeter, have the corresponding recoil proton detected in the proton array simply because of the detector's geometry. Furthermore, the geometrical acceptance of the calorimeter is affected by the core region cut that is applied to proton array. . . . .	107
58	The extended solid lines represent the geometrical limits expressed in (112) which removes 42 edge calorimeter blocks in total. The blocks in the dashed line region (blue) and the ultra-fine dashed line region (red) grouped in four in order to study the missing mass squared in the calorimeter. As can be seen in Fig. 57 not all calorimeter blocks have the triple coincidence event because of the proton array geometry. Therefore, the calorimeter blocks in the limits of (112) grouped in four to study the missing mass squared. . . . .	108
59	Photon energy exclusivity re-normalization . . . . .	110
60	Showing fiducial cut implemented to the proton array based on the fact that expressed in Fig. (31). Thereafter in the text, the region displayed by solid lines is referred as the core region of the proton array. The coordinates shown as $x_i$ and $y_i$ proton array coordinates to extract block number. . . . .	110
61	Proton array time distribution displayed here is after the applied energy threshold is 30 MeVee (MeV electron equivalent, a deposited energy of 1 MeV generates 1 MeVee in light output at linear light yield). . . . .	111
62	Predicted block is the central block and we look for the eight surrounding blocks . . . . .	112
63	Energy deposited in proton array blocks with grouping in nine algorithm. Corresponding block position to the numbers in each block can be seen in Fig. (62) Dashed curves are before the background subtraction and the filled curves is after the subtraction. The deposited energy distribution in the central block shows that algorithm that we developed works and an energy threshold value of 30 MeVee is reasonable to perform the analysis. . . . .	114
64	Symmetric and asymmetric $\pi_0$ decay . . . . .	115



- 65 Missing mass squared ( $M_X^2$ ) for  $H(e, e'\gamma)X$  events. The  $M_X^2$  denoted by star is the distribution which has no subtraction. The  $M_X^2$  denoted by triangle corresponds to the  $N_{calo}^{acc} + N^{\pi_0}$  events. The solid line is obtained from star distribution by subtracting the triangle distribution. The solid circle plot is obtained by Monte Carlo Simulation normalized to the same maximum value as the solid line. . . . . 118
- 66 Missing mass squared distribution of  $H(e, e'\gamma p)$  events for the group-of-nine selection. The  $M_X^2$  denoted by star is the distribution which has no subtraction. The  $M_X^2$  denoted by triangle corresponds to the  $N_{pa}^{acc} + N^{\pi_0}$  events. The solid line is obtained from star distribution by subtracting the triangle distribution. The solid circle plot is obtained by Monte Carlo Simulation normalized to the same maximum value as the solid line. . . . . 119
- 67 Missing mass squared distribution of  $H(e, e'\gamma p)$  events with detected proton in the exclusive predicted block. The  $M_X^2$  denoted by star is the distribution which has no subtraction. The  $M_X^2$  denoted by triangle corresponds to the  $N_{pa}^{acc} + N^{\pi_0}$  events. The solid line is obtained from star distribution by subtracting the triangle distribution. The solid circle plot is obtained by Monte Carlo Simulation normalized to the same maximum value as the solid line. . . . . 119
- 68 The square  $M_X^2$  spectrum is the  $H(e, e'\gamma)X$  events after the subtraction of  $N_{calo}^{acc} + N^{\pi_0}$ . The solid line  $M_X^2$  spectrum is the  $H(e, e'\gamma p)$  events for the group-of-nine and after the subtraction of  $N_{pa}^{acc} + N^{\pi_0}$ . The dashed line  $M_X^2$  spectrum is the  $H(e, e'\gamma p)$  events with events with detected proton in the exclusive predicted block and after the subtraction of  $N_{pa}^{acc} + N^{\pi_0}$ . . . . . 120
- 69 The displayed spectrum is the  $M_X^2$  spectrum in Fig. 68 but binned in azimuth. The dashed  $M_X^2$  spectrum is the  $H(e, e'\gamma)X$  events after the subtraction of  $N_{calo}^{acc} + N^{\pi_0}$ . The solid  $M_X^2$  spectrum is the  $H(e, e'\gamma p)$  events for the group-of-nine and after the subtraction of  $N_{pa}^{acc} + N^{\pi_0}$ . The star  $M_X^2$  spectrum is the  $H(e, e'\gamma p)$  events with exclusive predicted block is the central block of group-of-nine requirement and after the subtraction of  $N_{pa}^{acc} + N^{\pi_0}$ . In this configuration, azimuthal angle increases from right to left, polar angle increases from bottom to top and each histogram constitutes two proton array blocks in core region. . . . . 121
- 70 The mean of the Gaussian fit of the  $M_X^2$  spectra of  $H(e, e'\gamma p)$  events for the proton detected in the exclusive predicted block. The left (right) spectra corresponds to simulation (data). The simulation mean values are stable relative to data. The variation in simulation mean values show consistent trend for the middle and outer ring. However, the variation in data mean values for all rings show inconsistent trend. . . 122

71	The width of Gaussian fit ( $\sigma(M_X^2)$ ) of the $M_X^2$ spectra of $H(e, e'\gamma p)$ events for the proton detected in the exclusive predicted block. The left (right) spectra corresponds to simulation (data). The variation in these spectra shows inconsistent trend so much so that some blocks have smaller $\sigma(M_X^2)$ than simulation . . . . .	122
72	$M_X^2$ spectra in electromagnetic calorimeter. Each histogram constitutes four calorimeter blocks. The histogram with dashed line frame correspond to the dashed line region, and the histogram with solid lines correspond to the fine dashed line region of the calorimeter shown in Fig.(58) . . . . .	123
73	$M_X^2$ distribution in individual calorimeter blocks. These blocks correspond to the dashed line region in the calorimeter shown in Fig. 58. . . . .	125
74	The Gaussian fit peak, $\langle M_X^2 \rangle_G$ , position before the re-calibration as a function of calorimeter block . The calorimeter blocks in this plot correspond to the dashed line region in calorimeter shown Fig. (58). .	126
75	The Gaussian width $\sigma(M_X^2)$ for $M_X^2$ distribution as a function of calorimeter block. The calorimeter blocks in this plot correspond to the dashed line region in calorimeter shown Fig. (58). . . . .	127
76	The Gaussian fit peak position for $M_X^2$ distribution after all iterations as a function of calorimeter block. The calorimeter blocks in this plot correspond to the dashed line region in calorimeter shown Fig. (58). .	131
77	The Gaussian width $\sigma(M_X^2)$ for $M_X^2$ distribution after all iterations as a function of calorimeter block. The calorimeter blocks in this plot correspond to the dashed line region in calorimeter shown Fig. (58). .	131
78	$t$ dependence on $x_B$ . . . . .	134
79	$t_{min} - t$ dependence on $x_B$ . . . . .	135
80	The projection of $t_{min} - t$ on the surface of the calorimeter with the missing mass squared range of $0.4 < M_X^2 < 1.2 GeV^2$ . From left to right corresponding $t_{min} - t$ intervals of: $[0,0.05]$ , $[0.05,0.1]$ , $[0.1,0.15]$ , $[0.15,0.2]$ , $[0.2,0.25] GeV^2$ . . . . .	136
81	Beam Spin Asymmetry measurement for the $t_{min} - t$ bin interval of $[0.00,0.05] GeV^2$ which corresponds to the central region of the calorimeter (Fig.80). . . . .	136
82	Beam Spin Asymmetry measurement for the $t_{min} - t$ bin interval of $[0.05,0.10] GeV^2$ . Corresponding calorimeter region to bin interval, can be seen in Fig.(80). . . . .	137
83	Beam Spin Asymmetry measurement for the $t_{min} - t$ bin interval of $[0.10,0.15] GeV^2$ . Corresponding calorimeter region to bin interval, can be seen in Fig.(80). . . . .	137
84	Beam Spin Asymmetry measurement for the $t_{min} - t$ bin interval of $[0.15,0.20] GeV^2$ . Corresponding calorimeter region to bin interval, can be seen in Fig.(80). . . . .	138

85	Beam Spin Asymmetry measurement for the $t_{mn} - t$ [0.20,0.25] $GeV^2$ .Corresponding calorimeter region to bin interval, can be seen in Fig.(80). . . . .	138
86	Fit parameter $\alpha$ of Eq. (139) as a function of $t_{mn} - t$ . The squares denotes the $H(e, e'\gamma p)$ events with detected proton in the exclusive predicted block, the up pointing triangle denotes $H(e, e'\gamma p)$ events in the group of nine, and the down pointing triangle denotes $H(e, e'\gamma)X$ events with the proton prediction in core region of proton array. . . .	141
87	The deviation of triple coincidence BSA measurements from the double coincidence BSA measurements as a function of $t_{mn} - t$ bin. . . . .	141
88	VGG calculation for triple coincidence beam spin asymmetry. The $t_{mn} - t$ bin interval is $t_{mn} - t \in [0.00, 0.05] GeV^2$ . . . . .	142
89	VGG calculation for triple coincidence beam spin asymmetry. The $t_{mn} - t$ bin interval is $t_{mn} - t \in [0.05, 0.10] GeV^2$ . . . . .	143
90	VGG calculation for triple coincidence beam spin asymmetry. The $t_{mn} - t$ bin interval is $t_{mn} - t \in [0.10, 0.15] GeV^2$ . . . . .	143
91	VGG calculation for triple coincidence beam spin asymmetry. The $t_{mn} - t$ bin interval is $t_{mn} - t \in [0.15, 0.20] GeV^2$ . . . . .	144
92	VGG calculation for triple coincidence beam spin asymmetry. The $t_{mn} - t$ bin interval is $t_{mn} - t \in [0.20, 0.25] GeV^2$ . . . . .	144
93	The kinematics of the electro-production in the target rest frame. The- $z$ direction is chosen counter-along the three-momentum of the incoming virtual photon. The electron three momenta from the lepton scattering plane, while the recoiled proton and outgoing real photon define the hadron scattering plane. In this reference system the azimuthal angle of the scattered lepton is $\phi_l = 0$ , while the azimuthal angle between the lepton plane and the recoiled proton momentum is $\phi_N = \phi$ . When the hadron is transversely polarized (in this reference frame) $S_{\perp} = (0, \cos \Phi, \sin \Phi, 0)$ , the angle between the polarization vector and the scattered hadron is denoted as $\varphi = \Phi - \phi_N$ . . . . .	146
94	Calculated cross section for target polarization of $TP_x$ . The upper histogram displays the $DS$ and bottom one displays $TS$ . . . . .	153
95	Calculated cross section for target polarization of $TP_y$ . The upper histogram displays the $DS$ and bottom one displays $TS$ . . . . .	154
96	Calculated cross section for target polarization of $LP$ . The upper histogram displays the $DS$ and bottom one displays $TS$ . . . . .	155
97	Kinematics-1 difference in cross section. The upper histogram $t_{mn} - t$ value is $0.05 GeV^2$ , and the bottom histogram's $t_{mn} - t$ value is $0.15 GeV^2$ . . . . .	157
98	Kinematics-2 difference in cross section. The upper histogram $t_{mn} - t$ value is $0.05 GeV^2$ , and the bottom histogram's $t_{mn} - t$ value is $0.15 GeV^2$ . . . . .	158

99	Kinematics-3 difference in cross section. The upper histogram $t_{min} - t$ value is $0.05 \text{ GeV}^2$ , and the bottom histogram's $t_{min} - t$ value is $0.15 \text{ GeV}^2$ . . . . .	159
100	Kinematics-4 difference in cross section. The upper histogram $t_{min} - t$ value is $0.05 \text{ GeV}^2$ , and the bottom histogram's $t_{min} - t$ value is $0.15 \text{ GeV}^2$ . . . . .	160

# CHAPTER I

## INTRODUCTION

The complicated structure of matter has been studied since the 18<sup>th</sup> century. The more we learn about matter, the deeper we want to study this structure. This has entailed an avalanche of knowledge which opened many areas in physics, including probing the structure of the atomic nucleus. Much of the knowledge that we know about the internal structure of the nucleon has been revealed within the last 5 decades through scattering of electrons on proton and nuclei. The dynamics of the nucleon's constituents are defined by Quantum Chromodynamics (QCD), and according to asymptotic freedom, the constituents of the nucleon, quarks and gluons are free at asymptotically high virtualities in the nucleon. The size of the proton is approximately  $10^{-15}$  m which means in order to investigate the dynamics of a free parton one need to have a probing particle which has a wavelength smaller than this nucleon size. According to the momentum wavelength relation,  $p\lambda = h$ , the bigger the momentum a particle carries, the smaller the wavelength it has. Based on this phenomenology there exist two complementary experimental processes to probe the nucleon, elastic scattering and Deep Inelastic Scattering (DIS). These two processes provide us precise but limited results; Elastic Form Factors (FFs) and Parton Distribution Functions (PDFs). The former contains information on the charge and magnetization distributions in the transverse plane and the later contains information on the longitudinal momentum of the partons in the fast moving hadron.

The recently developed formalism of Generalized Parton Distributions (GPDs) shows that information on quark-quark correlation, the transverse quark momentum distribution can be observed in the deep exclusive reactions. GPDs provide a unique formalism for the interpretation of the fundamental quantities of hadronic structure in a unified way. For example, elastic nucleon FFs appear in the limiting case of GPDs, and the PDFs appear in the first moment of GPDs. Thus deep exclusive reactions provide a complete 3-dimensional picture of the nucleon structure. In particular, the GPDs allows a possible determination of the total angular momentum of quarks in the nucleon.

---

This dissertation follows the style of *The Physical Review*

Among the known deep exclusive reactions, the Deeply Virtual Compton Scattering (DVCS,  $ep \rightarrow ep\gamma$ ), is not only the cleanest way to access the GPDs experimentally but also the simplest and the most promising reaction in connection with GPDs. DVCS is a challenging process:

- Unlike the DIS, all final states needs to be detected;
- DVCS cross section is very small;
- Identifying different channels and removing background requires good experimental resolution;

However, since DVCS provides a wealth information about GPDs, experimentalist started to work on the feasibility to be able to run this promising experiment in the available experimental facilities. The initial conclusion was that dedicated experimental setup would allow to perform this experiment with much more statistics.

A dedicated experiment ran in the Hall A at Jefferson Laboratory in Fall 2004. Running in the Hall A and construction of two dedicated detectors (electromagnetic calorimeter and proton array), provides remedies to above mentioned challenges, nevertheless, it ensued the issue of running at a high luminosity while detecting the three final states. Because of the experimental constraints, the detector apparatus was installed at small angles and very close to the scattering chamber. Consequently, electromagnetic and hadronic background became the issue which substantially solved by the dedicated electronics and acquisition system.

In this dissertation, the characteristic the E00-110 experiment detectors is outlined. The missing mass squared study for the triple coincidence ( $H(e, e'\gamma p)$ ) is discussed in details along with a new calibration of the deeply virtual Compton scattering photon. The main objective of this dissertation is to check the exclusivity of double coincidence ( $H(e, e'\gamma X)$ ) via studying the consistency between the beam spin asymmetry measurement of ( $H(e, e'\gamma p)$ ) and ( $H(e, e'\gamma X)$ ).

In Chapter II, the theoretical framework is discussed briefly. The very core concept in high energy physics the probing phenomenology is discussed along with elastic scattering, and deep inelastic scattering and relation to electromagnetic form factors structure functions respectively. A brief overview of the transition from deep inelastic scattering to hard exclusive scattering discussed with factorization. The notion of generalized parton distributions is outlined with their limit properties. Finally, the

phenomenology of generalized parton distributions is outlined, and specifically the theory of deeply virtual Compton scattering is summarized.

In Chapter III, a summary of the experimental studies in deeply virtual Compton scattering is provided. The published results from different accelerator facilities including Jefferson Laboratory is provided. The future experiments specifically the 12 GeV experiments are very briefly discussed.

In Chapter IV, the experimental setup is explained. An overview of the Continuous Electron Beam Accelerator Facility at Thomas Jefferson National Accelerator is provided. The experimental Hall A at Jefferson Laboratory is discussed in detail by providing information on, high resolution spectrometers, beam line instruments, the target system, and data acquisition. In addition to the standard Hall A equipment, the dedicated E00-110 electromagnetic calorimeter and proton array are discussed along with the dedicated data acquisition installed for this experiment.

In Chapter V, the Monte Carlo Simulation of E00-110 experiment is briefly discussed. The electron generation, and the hadronic reaction generation is outlined.

In Chapter VI, HRS and Calorimeter wave form analysis is discussed. The standard experimental Hall A equipment data analysis is outlined. Details of waveform algorithm which is improved for E00-110 experiment is provided. The initial electromagnetic calorimeter analysis as well as for the proton are discussed.

In Chapter VII, data analysis for the triple coincidence events is discussed in detail. The kinematics which the experiment conducted is provided, and the global calibration of each three detectors is summarized. The electron event selection is outlined. The implementation of the clustering and geometrical cuts for the photon event selection is discussed. The steps in recoil proton selection: photon energy exclusivity re-normalization, the proton direction, energy threshold, background, accidentals, the missing mass squared study both in proton array and calorimeter are discussed in detail. Finally, the procedure for the re-calibration of the data and Monte Carlo simulation is provided.

In Chapter VIII, the triple coincidence beam spin asymmetry measurements of deeply virtual Compton scattering is presented. The bins of this study, the fit that is implemented to the data and the exclusivity test is discussed.

In Chapter IX, the polarized deeply virtual Compton scattering observables are calculated based on VGG model. The main objective of this calculation to study the sensitivity of the polarized deeply virtual Compton scattering observables to the

E-type GPDs. The interference term and angular harmonics for polarized targets, and the details of the VGG model that is used, is discussed in details. The projected cross section results are presented for four different kinematics on a polarized  ${}^3\text{He}$  target.

Chapter X concludes the dissertation with a summary of the experiments and the studies performed in the context of this dissertation.



## CHAPTER II

### PHYSICS MOTIVATION

Over the course of history, the ramifications in Physics are the natural consequence of the avalanche of Physic knowledge. Moreover, from these ramifications ensued the perception of there being an open ended process for advancements in Physics, unlike the early stages of science in history. On account of this fact, in this chapter I will briefly discuss the significant milestones in the study of the composite structure of the nucleon.

#### II.1 THE PROBING PHENOMENOLOGY

The discovery of  $\beta$  and  $\alpha$  particles introduced the concepts of scattering in studying atomic structure, passing a beam of  $\beta$  particles through atoms let Lenard observe the empty space within atoms. Then a beam of  $\alpha$  particles led Rutherford to observe the deflection of these particles with large angles as a result of collisions within the atom [1].

Electron scattering [2] was introduced as a tool to investigate the composite structure of matter and since then it has become a powerful probe in the studies of hadron substructure. When an electron scatters from a target it is called electromagnetic reaction and the transfer of energy and momentum to the target is done via an electromagnetic probing particle, a virtual photon Fig.(1) & Fig.(2).

Knowing the probing particle provides finer control of variables, and decreases the complexity of the interaction [3]. The elastic electron scattering reaction can be expressed as:

$$e + p \rightarrow e' + p \quad (1)$$

in this reaction by knowing the electron and using the virtual photon, one can vary the squared momentum  $q^2$  where the four momentum transfer  $q$  can be written as:

$$q = k_i - k_f \quad (2)$$

where  $k_i$  and  $k_f$  are the four momenta of the incoming and scattered electron respectively.

$$k_i \equiv k_i^\mu = (\epsilon_i, \vec{k}_i) \quad (3)$$

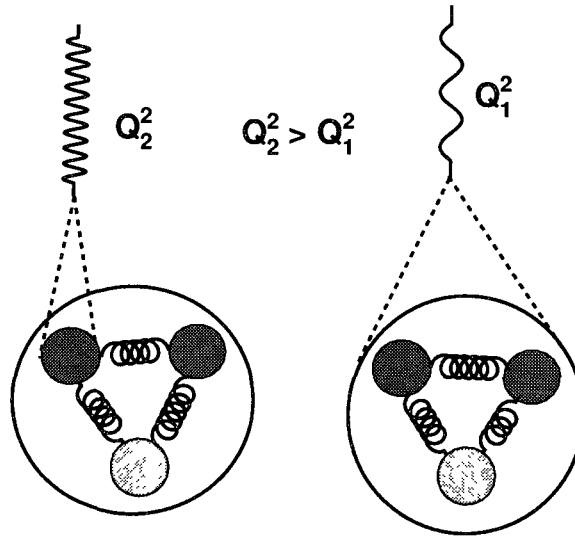


FIG. 1: Increasing the resolution by increasing the  $Q^2$ , (changing the virtuality of the photon) yields different pictures of the proton. As illustrated, in this case of  $Q_2^2 > Q_1^2$ , one can see quark structure and coherent proton respectively with these two different  $Q^2$  values. For example, at Jefferson Lab, by using associated wavelength  $\lambda = \frac{\hbar c}{q}$  which allows to probe  $10^{-16}$  meter with a  $Q^2 = 1\text{GeV}^2$ .

and

$$k_f \equiv k_f^\mu = (\epsilon_f, \vec{k}_f) \quad (4)$$

When large momentum and energy are transferred then, by the uncertainty principle, the current can resolve very small space-time distances and hence the reveal the **parton** substructure of the target [4] (see Fig. 1). The change in momentum between the incoming electron and scattered electron allows us to write the virtuality of the photon as:

$$Q^2 = -q^2 = -(k_i - k_f)^2 \quad (5)$$

Then the transverse distance probed by the virtual photon in hadron will be in the order of

$$\delta z_\perp \sim \frac{1}{Q} \quad (6)$$

meaning that if the virtuality of the photon,  $Q^2$ , is sufficiently high, it will probe more fine structure.

## II.2 ELASTIC SCATTERING: ELECTROMAGNETIC FORM FACTORS

The first concrete indication of the composite structure of nucleon was the observation of the strong deviation in the measured values of magnetic moments of proton and neutron contrary to their expected values which relied on the assumption that proton and neutron were point-like Dirac particles [5].

The revealed information was not a simple deviation from expected values rather it suggested a picture of spatial composite structure, the transverse distribution of nucleon's constituents in coordinate space. A remarkable measurement based on elastic scattering [2] of relativistic electrons from a nucleon (e.g. proton) first revealed this structure Eq.(1). The one-photon exchange mechanism of this process is illustrated in Fig. (2).

The cross section for the scattering from a point-like charge is given by Mott the cross section [6]

$$\left(\frac{d\sigma}{d\Omega}\right)_{Mott} = \frac{\alpha^2}{4\epsilon^4 \sin^4 \frac{\theta}{2}} \cdot \frac{\epsilon'}{\epsilon} \cos^2 \frac{\theta}{2} \quad (7)$$

Here  $\alpha = \frac{e^2}{\hbar c} \approx \frac{1}{137}$ ,  $\theta$  is the scattering angle (the angle between  $k_i$  and  $k_p$  see fig. 2) and  $\epsilon$  and  $\epsilon'$  are the incident and scattered electron beam energies.

For a spin 1/2 target with an extended structure and an anomalous magnetic moment one obtains the Rosenbluth cross section [7]

$$\frac{d\sigma}{d\Omega} = \left(\frac{d\sigma}{d\Omega}\right)_{Mott} \left\{ F_1^2(Q^2) + \frac{Q^2}{4M^2} [F_2^2(Q^2) + 2(F_1(Q^2) + F_2(Q^2))^2 \tan^2 \frac{\theta}{2}] \right\} \quad (8)$$

which introduces the Dirac form factor  $F_1(Q^2)$  and Pauli form factor  $F_2(Q^2)$ . The latter carries the information about the anomalous magnetic moment of the target nucleon. The linear combination of these form factors are the Sachs form factors:

$$G_E(Q^2) = F_1(Q^2) - \frac{Q^2}{4M^2} F_2(Q^2), \quad (9)$$

$$G_M(Q^2) = F_1(Q^2) + F_2(Q^2), \quad (10)$$

also referred to as electric ( $G_E$ ) and magnetic ( $G_M$ ).

In the non-relativistic limit the squares of the electric and magnetic form factors  $G_{E,proton}(Q^2)$  and  $G_{M,proton}(Q^2)$  are the Fourier transforms of the spatial distributions of charge and magnetic moment, respectively. And their normalization at  $Q^2 = 0$  are:

$$G_{E,proton}(0) = 1, \quad G_{M,proton}(0) = \mu_{proton} = 2.973; \quad (11)$$

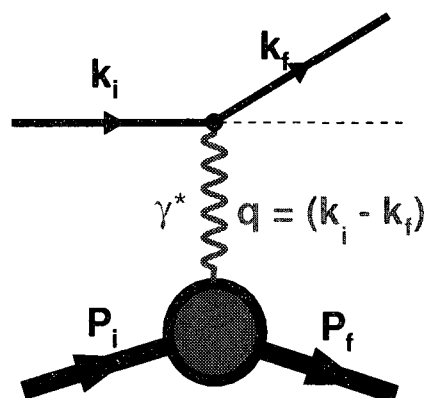


FIG. 2: Elastic scattering of an electron from a nucleon through one-photon exchange. Here in this illustration,  $k_i$  is the four momenta of incoming electron beam,  $k_f$  is the four momenta of the scattered electron, and  $\gamma^*$  is the exchange virtual photon carries the four momentum transfer  $q$ .

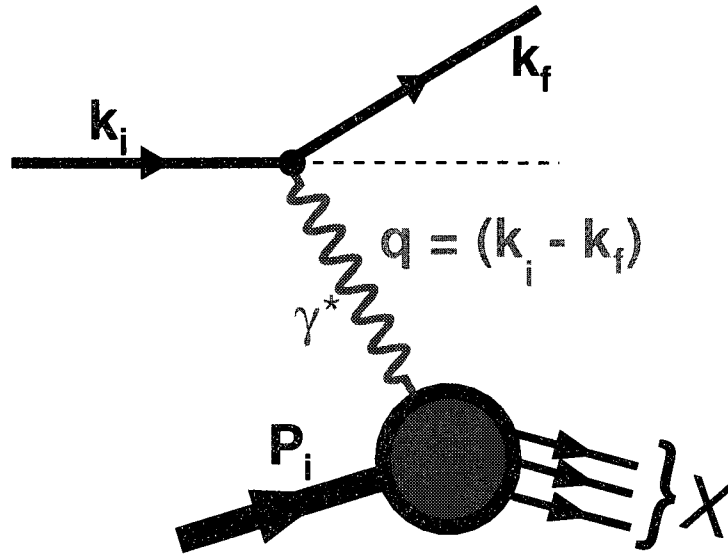


FIG. 3: Illustration of a typical inclusive Deep-Inelastic Scattering event in which an incident electron transfers momentum  $q$  to the target and the hadronic final states,  $X$ , are not distinguished. DIS is an inclusive reaction which only the scattered electron is detected. DIS can be restricted on single-photon exchange as a result of the fact that the electromagnetism in this reaction dynamics is very weak in contrast to strong interactions.

$$G_{E,neutron}(0) = 0, \quad G_{M,proton}(0) = \mu_{neutron} = -1.913. \quad (12)$$

### II.3 DEEP INELASTIC SCATTERING: PARTON DISTRIBUTIONS

Having measured the form factors as explained in II.2, now a more detailed picture of this composite structure can be acquired by increasing the  $-q^2 (\equiv Q^2)$  of the virtual photon to improve the resolution power of the probing particle (details can be seen in II.1). Consider an interaction of electron beam with a hadronic target through single photon exchange as illustrated in Fig. (3). Similar to the II.2 the momentum transfer

is denoted by  $q$  ( $q^\mu = (\nu, \vec{q})$ ), and the target momentum is  $P_i$  ( $P^\mu = (M, \vec{0})$ ) in the lab frame, so one can write the invariant mass squared of the final hadronic state ( $X$  in Fig. 3) is

$$W^2 = (P_i + q)^2 = M^2 + 2P_i \cdot q - Q^2 \quad (13)$$

and if we force the  $W^2$  to a fix value, such as resonance mass,  $M_R$ , then the  $Q^2$  for this reaction becomes

$$Q^2 = (M^2 - M_R) + 2M\nu \quad (\nu = \epsilon - \epsilon') \quad (14)$$

The kinematical region, where  $Q^2 > 1 \text{ GeV}^2$  and  $W^2 > 4 \text{ GeV}^2$ , refers to as the deep inelastic regime. In particular, very large momentum transfer means that we can resolve objects with a size of  $0.1 \text{ fm}$  at  $Q^2 = 4.0 \text{ GeV}^2$ . Thus, by going into this deep inelastic region, we can probe the energy and momentum of the fundamental constituents of hadronic structure. In the deep regime where having the final state  $X$  (Fig.(3)) as excited hadronic states other than proton, requires a parametrization of the hadronic tensor in a general way, which eventually entails the study of the cross section of this inclusive process [8].

### II.3.1 Structure Functions

In the electron hadron deep inelastic scattering as illustrated in Fig.(3), right before the interaction with the target, incoming electron beam decays in to an electron and a photon,  $e \rightarrow e'\gamma^*(q)$ , which is followed by the absorption of the photon on the target initial state  $|p\rangle_N$  and creating a number of hadrons in the final state,  $\langle n|$  with the total momentum  $P_n = \sum_k p_k$ . In this single-photon exchange approximation, the transition matrix element associated with the Feynman diagram in Fig.(3) is

$$\Upsilon_n = L_\mu(e, e') \langle n | j^\mu(0) | p \rangle \quad (15)$$

where the leptonic current for electron is

$$L^\mu(e, e') = \frac{1}{q^2} \bar{u}(e') \gamma^\mu u(e) \quad (16)$$

and  $\langle n | j^\mu(0) | p \rangle$  is hadronic transition amplitude via the local quark electromagnetic current

$$j^\mu(x) = \sum_{q=u,d} e_q \bar{\psi}_q(x) \gamma^\mu \psi_q(x) \quad (17)$$

The measurement is totally inclusive with respect to the final states and only the scattered electron detected. Neglecting the phase space factor, one can write the cross-section of the deep inclusive inelastic scattering

$$\sigma_{DIS} = |\Upsilon_n|^2 (2\pi)^4 \delta^4(p + q - P_n) \sim L_\mu^\dagger L_\nu W^{\mu\nu} \quad (18)$$

The hadronic tensor [9] is introduced as

$$W^{\mu\nu} = \frac{1}{4\pi} \int d^4 z e^{iq \cdot z} \langle p | j^\mu(z) j^\nu(0) | p \rangle \quad (19)$$

The decomposition of the hadronic tensor in independent Lorentz tensors introduces the structure functions. The most general form of  $W^{\mu\nu}$  tensor can be expressed as

$$W^{\mu\nu} = A^{\mu\nu} W_1(\nu, Q^2) + B^{\mu\nu} \frac{W_2(\nu, Q^2)}{M^2} \quad (20)$$

which is the linear combination of spin independent structure functions  $W_1$  and  $W_2$ . The kinematic tensors  $A^{\mu\nu}$ ,  $B^{\mu\nu}$ , are described e.g. [9]. Bjorken [10, 11] proposed to study the spin independent structure functions in the limit of  $Q^2 \rightarrow \infty$ ,  $\nu \rightarrow \infty$  where in the case of having the  $\frac{\nu}{Q^2}$  ratio fixed. In addition to that, Bjorken introduced a new variable

$$x_B = \frac{Q^2}{2M\nu} \quad (21)$$

### Scaling

The analysis of the deep inelastic scattering experiment in the Bjorken's proposed limit led to the discovery of scaling phenomenon [12] which states that in these limits the structure functions become functions of ratio  $x$  which is defined in Eq. (21)

$$\begin{aligned} MW_1(\nu, Q^2) &= F_1(x_B) \\ \nu W_2(\nu, Q^2) &= F_2(x_B) \end{aligned} \quad (22)$$

The experimental observation was the pioneer evidence of so-called scaling, e.g.  $Q^2$  independence, property of the spin independent structure functions of proton. The dependence on a dimensionless variable  $x_B$  is named as scaling because of the fact that, no energy or length scale governs the interaction. One other interpretation of DIS, based on scaling, can be an elastic scattering of an electron beam on a free point-like particle, quark (Fig. (1)), carrying a momentum fraction  $x_B$  of the parent proton.

## Parton Model

In the deeply inelastic scattering as mentioned in II.1, the photon interacting with the target acts a probe meaning that resolution is set by the inverse of the photon's virtuality,  $Q^2$ . At higher  $Q^2$  the cross section will be dominated by the beam scattering incoherently and elastically from the nuclear constituents rather than the nucleon itself [13]. Based on this fact Feynman proposed a model [14] where the proton consists of quasi-free point like partons in the infinite momentum frame where nucleon's momentum, proton, along the z direction approaches infinity. Moreover, in this momentum reference frame, relativistic time dilation implies the motion of the constituents are slowed down so that the constituents are perceived to be non-interacting with one another during the absorption of the virtual photon so that the process can be classified with the impulse approximation. The essential physical conclusion from this scattering is that the scattering reflects the properties and characteristics of the motion of the constituents. In the following years after Feynman, the new interpretation of this observation became the asymptotic freedom proved by QCD [15, 16].

## Forward Compton Scattering Amplitude

The cross section of the DIS can be computed by optical theorem from the imaginary part of the forward Compton amplitude

$$W^{\mu\nu} = \frac{1}{2\pi} \Im T^{\mu\nu} \quad (23)$$

(as shown in Fig. 4 see appendix C in [9] for detailed descriptions) where  $T^{\mu\nu}$

$$T^{\mu\nu} = i \int d^4z e^{iq \cdot z} \langle p | T \{ j^\mu(z) j^\nu(0) \} | p \rangle \quad (24)$$

is determined by the time-ordered product of quark electromagnetic current in Eq. (17). The Compton amplitude can be computed as a virtual photon interacting with a single quark. Therefore, the DIS is described by the diagonal elements of the Compton Amplitude matrix elements.

### II.3.2 Hard Scattering Reactions and Factorization

The hadronic tensor  $W^{\mu\nu}$  in the cross section (Eq.23) depends upon the full QCD dynamics of the target.



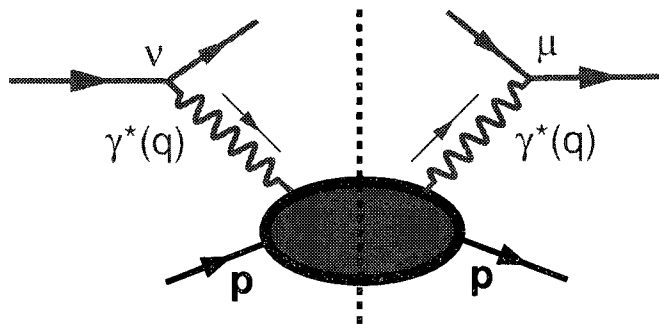


FIG. 4: Hadronic tensor of the deep inelastic scattering cross section determining the imaginary part of the forward Compton Scattering amplitude  $\gamma^*(q)N(p) \rightarrow \gamma^*(q)N(p)$

The number of partons that carry the bulk of the hadron momentum is small, therefore, the photon usually will see only one parton per collision. For a system constituting  $n$  partons, the coherent scattering probability is suppressed by the  $n$ th power of the photon virtuality,

$$P_n \sim \left(\frac{|\delta z_\perp|^2}{\pi R_N^2}\right)^n \sim \frac{1}{(Q^2 \pi R_N^2)^n} \quad (25)$$

where  $\pi R_N^2$  is the transverse area of the nucleon. This is also named higher twist approximation in which at high  $Q^2$  values one can restrict all considerations to the photon scattering on a single parton which is known as handbag approximation for hard scattering.

The essential physical picture can be seen in Fig. 5 for the forward Compton scattering on a quark [17]. The points of photon absorption and re-emission are separated by a light like distance. The characteristics of the relevant distances in Compton amplitude in the limit  $Q^2 \rightarrow \infty$ , (large virtualities),  $Q^2$ , large energies,  $\nu \sim p \cdot q$ , and at Bjorken variable  $x_B = \frac{Q^2}{p \cdot q}$  fixed, probe short-distance and time

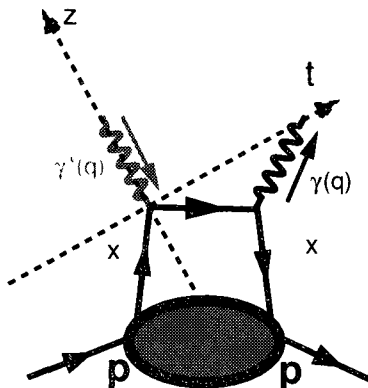


FIG. 5: Handbag diagram for the forward Compton Scattering. With the absorption of virtual photon, at  $t=0$ , a quark taken out from hadron as a result it accelerates, then re-emits another virtual photon, at a later time  $t > 0$ , then decelerates and acquires same initial momentum state. The point of absorption and emission are separated by a light like distance.

structure of the process, respectively. The derivation of the relevant distances in DIS has shown e.g. in [9] in a reference frame where the target proton is at rest and the virtual photon's three-momentum points in the direction opposite to the  $z$ -axis, Fig.5. The integrand in Eq. (24) is an oscillatory function and thus gives vanishing results unless the distances involved are

$$z^- \sim \frac{1}{Mx_B}, \quad z^+ \sim \frac{Mx_B}{Q^2} \quad (26)$$

Therefore, the only region which contributes to the integral is close to the light-cone  $z^2 = (z^0)^2 - \mathbf{z}^2 = z^+z^- - z_{\perp}^2 \approx 0$ , with all coordinates negligible except  $z^-$  where

Thus hard process occupies a small space-time volume and the scales that are involved in the formation of the hadron non-perturbative wave functions are much larger, of order of a typical hadronic scale (1 GeV) and it is quite likely that the two scales are uncorrelated and will not interfere.

The optical theorem (II.3.1) allows to sum over all final states in DIS as the intermediate state of the forward Compton amplitude (Fig. 4). As a consequence of the small spatial scale (Eq.26) this intermediate states behaves as a free parton, with higher twist corrections from parton-parton interactions (Eq.25).

The information about the internal structure of the proton and the long-distance physics can be expressed by introducing a function  $q_i(x)$  which depends on the momentum fraction  $x$  (Fourier conjugate to  $z^-$ ) of the parent proton, and in the lowest order approximation  $x \equiv x_B$ . The, incoherence property of the deep inelastic scattering at short distances allows us to compute DIS cross section as the incoherent sum over all electron-parton scattering cross sections:

$$\left(\frac{d\sigma}{dx dQ^2}\right)_{DIS} = \sum_i \int dx e_i^2 q_i(x) \left(\frac{d\sigma}{dx dQ^2}\right)_{e q_i \rightarrow e q_i}, \quad (27)$$

which formally known as factorization [19] for hard scattering reactions. Here in Eq. (27)  $q_i(x)$  is the parton momentum density of the parton type  $i$  with the charge  $e_i$  inside the proton. The  $\left(\frac{d\sigma}{dx dQ^2}\right)_{e q_i \rightarrow e q_i}$  in Eq. (27) can be written as

$$\left(\frac{d\sigma}{dx dQ^2}\right)_{e q_i \rightarrow e q_i} = \sum_i e_i^2 q_i(x) \frac{2\pi\alpha^2}{Q^4} \left[1 + \left(1 - \frac{Q^2}{xs}\right)^2\right] \quad (28)$$

where  $s = (P + k)^2$ , and  $x$  is the momentum fraction defined in Eq. 21.

After absorbing the virtual photon, in addition to being non-interacting, the scattered parton should be on the mass shell and having a small mass compared to  $s$  and  $Q^2$ . As a consequence we can write that

$$(xP + q)^2 = x^2 M^2 - Q^2 + 2xP \cdot q \approx 0 \quad (29)$$

and neglecting the the small quantity  $x^2 M^2$  (compared with  $Q^2$  and  $\nu$  which are both very large), the Eq. (29) becomes

$$x = \frac{Q^2}{2P \cdot q} \quad (30)$$

Thus, we see that the momentum fraction  $x$  is just the previously defined Bjorken variable  $x_B$ .

To summarize, in DIS, the nucleon is seen as a collection of non-interacting, point-like constituents, one of which must have fraction  $x$  of the momentum of the parent nucleon in order to absorb the virtual photon. Since they are point like and non-interacting, the nucleon cross section is just the sum of the cross sections for scattering from individual partons,  $i$ , weighted by the number density of partons of type,  $i$ , with the momentum fraction  $x$  which in Eq. (28) denoted by  $q_i(x)$  called parton distributions. The relation [6] between structure functions and the parton distributions can be expressed as

$$F_1(x) \sim \frac{1}{2} \sum_i e_i^2 q_i(x) \quad (31)$$

and

$$F_2(x) \sim x \sum_i e_i^2 q_i(x) \quad (32)$$

Therefore, the measurement of the structure functions allow us to access the parton distributions, the probability density of a parton in the nucleon with a certain longitudinal momentum fraction  $x$ .

## II.4 GENERALIZED PARTON DISTRIBUTIONS (GPDs)

The previously mentioned methods to explore the internal structure of the proton are: 1. elastic reaction which measures electromagnetic form factors (see II.2), and (deep) inelastic knock-out scattering experiments which allows access to momentum distribution of nucleon's constituents (see II.3). Although being complementary, these two approaches have similar deficiencies. The form factors do not contain dynamical information on the constituents, such as their speed and angular momentum whereas the momentum distributions do not provide information on the constituents' spatial location. More complete description of a microscopic structure, like nucleon, in fact lies in the correlation between the momentum and spatial distribution.

In this section I will summarize the notion of Generalized Parton Distributions (GPDs): the theoretical background; and the following section will be the phenomenology of GPDs: the exclusive reactions specifically DVCS.

### II.4.1 From Compton Amplitude to GPDs

Both observables addressed in the sections II.2 and II.3 provide only one-dimensional picture of the nucleon [20]. In both scattering processes only the magnitude of the scattering amplitude is accessed but its phase is lost. The orthogonal spaces are probed simultaneously in GPDs, which arise in the description of Deeply Virtual Compton Scattering (DVCS),  $ep \rightarrow ep\gamma$ . The steps for generalization of the handbag diagram for DIS in the Bjorken limit can be illustrated as: Fig.4  $\rightarrow$  Fig. 5  $\rightarrow$  Fig.6

According Feynman rule [21], the illustrated amplitude in Fig.(6) correspond to the Compton amplitude (Eq. (24)) with the exception of having a different proton final state:

$$T^{\mu\nu} = i \int d^4z e^{iqz} \langle p' | T \{ j^\mu(z) j^\nu(0) \} | p \rangle. \quad (33)$$

Following the discussion in [21] Compton amplitude (33) takes the form

$$\begin{aligned}
T^{\mu\nu}(p, q, \Delta) = & \frac{1}{2}(g^{\mu\nu} - \tilde{p}^\mu n^\nu - \tilde{p}^\nu n^\mu) \int_{-1}^1 dx \left( \frac{1}{x - \xi + i\epsilon} + \frac{1}{x + \xi - i\epsilon} \right) \\
& \left[ H(x, \xi, t) \bar{u}(p') \gamma \cdot n u(p) + E(x, \xi, t) \bar{u}(p') \frac{i\sigma^{\alpha\beta} n_\alpha \Delta_\beta}{2M} u(p) \right] \\
& + \frac{i}{2} \epsilon^{\mu\nu\alpha\beta} \tilde{p}_\alpha n_\beta \int_{-1}^1 dx \left( \frac{1}{x - \xi + i\epsilon} + \frac{1}{x + \xi - i\epsilon} \right) \\
& \times \left[ \tilde{H}(x, \xi, t) \bar{u}(p') n \cdot \gamma \gamma_5 u(p) + \tilde{E}(x, \xi, t) \frac{\Delta \cdot n}{2M} \bar{u}(p') \gamma_5 u(p) \right] \quad (34)
\end{aligned}$$

where  $H$ ,  $\tilde{H}$ ,  $E$ ,  $\tilde{E}$  are the GPDs.

The Fourier transform of the nucleon matrix elements of the bilinear parton operators are described as the GPDs [22, 23]. These quark and gluon operators are separated by a light-like interval  $z^2 = 0$  [17].

The reference frame in which  $P^\mu$  has only time and z components, both positive is used in this parametrization. So, the light-cone vectors in this reference frame can be written as

$$n^\mu = \frac{[1, 0, 0, -1]}{\sqrt{2}P^+}, \quad \tilde{p}^\mu = \frac{[1, 0, 0, 1]P^+}{\sqrt{2}} \quad (35)$$

where  $P^\mu = (p + p')^\mu/2$ . In the forward limit of the DVCS  $-2\xi$  is the “+” fraction of both the momentum transfer to the target and the virtual photon:

$$\Delta^+ = \Delta \cdot n \approx -2\xi P^+ \approx q \cdot n = q^+ \quad (36)$$

The quark GPDs  $H$  and  $E$ , are the matrix elements of the vector containing  $\gamma \cdot n = \gamma^+$ , can be written as [24]:

$$\begin{aligned}
& \int \frac{P^+ dz^-}{2\pi} e^{ixP^+z^-} \langle p' s' | \bar{\Psi}_f(-z^-/2) \gamma \cdot n \Psi_f(z^-/2) | s, p \rangle \\
& = \bar{U}(p', s') \left[ H_f(x, \xi, t) \gamma \cdot n + E_f(x, \xi, t) \frac{i}{2M} n_\alpha \sigma^{\alpha\beta} \Delta_\beta \right] U(p, s), \quad (37)
\end{aligned}$$

and the  $\tilde{H}$  and  $\tilde{E}$  GPDs are defined as the matrix elements of the axial operator containing  $n \cdot \gamma \gamma_5 = \gamma^+ \gamma_5$ :

$$\begin{aligned}
& \int \frac{P^+ dz^-}{2\pi} e^{ixP^+z^-} \langle p' s' | \bar{\Psi}_f(-z^-/2) \gamma \cdot n \gamma_5 \Psi_f(z^-/2) | s, p \rangle \\
& = \bar{U}(p', s') \left[ \tilde{H}_f(x, \xi, t) n \cdot \gamma \gamma_5 + \tilde{E}_f(x, \xi, t) \frac{n \cdot \Delta}{2M} \gamma_5 \right] U(p, s), \quad (38)
\end{aligned}$$

where the  $U(p, s)$  are the nucleon spinor and subscript  $f$  denotes the flavor- $f$  dependent GPDs. The positive and negative momentum fractions refer to quarks and anti-quarks, respectively. In the kinematic regions

- $x > \xi > 0$  the initial and final partons are quarks,
- $x < -\xi < 0$  the initial and final partons are anti-quarks,
- $-\xi < x < \xi$ , a  $q\bar{q}$  is exchanged.

#### II.4.2 GPD Kinematical Variables

The GPDs depend on three variables  $x$ ,  $\xi$  and  $t$ :  $x$  and  $\xi$  parametrize the independent longitudinal momentum fractions of the partons relative to the average proton momentum ( $\frac{1}{2}(p + p')$ ) as can be seen in Fig. 6 where  $x$  is the average longitudinal momentum fraction of the struck parton in the initial and final state, and the skewness parameter

$$\xi = \frac{-\bar{q}^2}{2\bar{q} \cdot P} \quad (39)$$

is the longitudinal momentum transfer where  $\bar{q} = (q_\mu + q'_\mu)/2$ . Moreover, the generalized Bjorken variable  $\xi$  has the same form with respect to the symmetric variables  $P$  and  $\bar{q}$  as does  $x_B$  with respect to the DIS variables  $p$  and  $q$ . In the Bjorken limit

$$\xi \rightarrow \frac{x_B}{2 - x_B} \quad \text{as} \quad \frac{t}{Q^2} \rightarrow 0 \quad (40)$$

the  $t$  dependence takes into account the transverse momentum transfer to the proton

$$t = (p' - p)^2 = \Delta^2 \quad (41)$$

The essential physical correspondence of these variables can be better understood by the generalization of the previously introduced Forward Compton Scattering.

#### Generalization of Forward Compton Scattering

The amplitude expressed in Eq. (24) is the forward Compton amplitude (see Fig. (5)) The generalization of this amplitude is important regarding the final states: a real photon rather than a virtual photon and a proton in a different momentum final state  $p'$ . Thus the non-perturbative dynamics, which is not described by the ordinary parton distribution, can be described with the generalized parton distributions. Among the possible corresponding exclusive reactions which have the required final states, Virtual Compton Scattering in the Bjorken limit

$$\gamma^* p \rightarrow p' \gamma \quad (42)$$

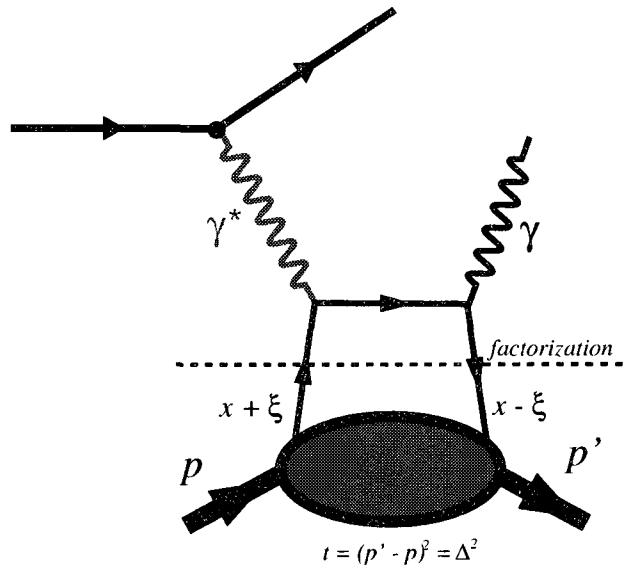


FIG. 6: Handbag diagram for Deeply Virtual Compton Scattering. Factorization of the  $\gamma^*p \rightarrow \gamma p$  DVCS amplitude in the Bjorken limit of large  $Q^2$  and  $t \ll Q^2$ . In this exclusive process, the virtual photon interacts with a quark of momentum fraction  $x + \xi$  and goes back in to the nucleon with a different momentum  $x - \xi$ . This change in longitudinal momentum occurs as a result of the momentum transfer  $\Delta$  and the emission of real photon.

is dominated by the leading twist handbag diagram illustrated in Fig. (6) and named as Deeply Virtual Compton Scattering (DVCS). It has been proved by factorization theorem that the DVCS amplitude is calculable as a product of GPDs which makes the GPDs experimentally accessible [19, 25].

#### II.4.3 Characteristics of GPDs

The richness of the physical content of generalized parton distributions can be illustrated by several relations such as the forward limit, the form factor limit (known as

first moment) and second moments of GPDs. I will discuss the physics in transverse plane ( $\xi = 0$ ) which is known as impact parameter space parton distribution. These relations not only provide access to specific physics content of the GPDs but also GPDs are become partially known in certain kinematical regions by satisfying these remarkable constraints.

### The Forward Limit

In the forward limit ( $p = p'$ ,  $t \rightarrow 0$ ,  $\xi \rightarrow 0$ ) GPDs are reduced to ordinary parton distributions

$$\lim_{t \rightarrow 0, \xi \rightarrow 0} H(x, \xi, t) = q(x), \text{ or } -\bar{q}(-x) \text{ if } x < 0 \quad (43)$$

and

$$\lim_{t \rightarrow 0, \xi \rightarrow 0} \tilde{H}(x, \xi, t) = \Delta q(x), \text{ or } \Delta \bar{q}(-x) \text{ if } x < 0 \quad (44)$$

As expected from the definitions of GPDs, the ordinary parton distributions, both unpolarized and polarized ( $q(x)$  and  $\Delta q(x)$ ) are nothing but the limiting case of GPDs. It is important to emphasize that, although GPDs are defined functions for  $\xi = 0$  or  $t = 0$ , these variables take only finite, non-zero values in any experiment. The E and  $\tilde{E}$  GPDs have no connection with ordinary parton distributions because of this fact, these GPDs are not constrained by deeply inelastic scattering, which corresponds to this forward limit.

### The Form Factor Limit

Another interesting limit of GPDs reduces them to the hadronic form factors.

$$\int_{-1}^1 dx H_q(x, \xi, t) = F_1^q(t), \quad \int_{-1}^1 dx E_q(x, \xi, t) = F_2^q(t) \quad (45)$$

$$\int_{-1}^1 dx \tilde{H}_q(x, \xi, t) = G_A^q(t), \quad \int_{-1}^1 dx \tilde{E}_q(x, \xi, t) = G_P^q(t) \quad (46)$$

After integrating over  $x$ , the first moments of GPDs, reveal the GPDs' constraints by the form factors. The well known electromagnetic Dirac  $F_1(t)$ , Pauli  $F_2(t)$ , axial  $G_A$  and pseudo-scalar  $G_P$  form factors are obtained as the lowest  $x$ -moments of the GPDs.



## GPDs and the Proton Spin Puzzle: Ji's Sum Rule

The GPDs profound relation to the distributions of angular momentum of quarks and gluons in proton renders them an appealing notion for study. The famous EMC measurement demonstrated that the contribution of the quark spin to the proton spin only about 20% of the anticipated result which was based on the naive quark model [26].

The spin crisis triggered a huge theoretical and experimental activity among one of which is Ji's sum rule [27]:

$$\frac{1}{2} \int_{-1}^1 dx \cdot x \cdot (H_f + E_f)(x, \xi, t) = A_f(t) + B_f(t) = J_f(t) \quad (47)$$

where the  $J_f$  is the total angular momentum, in other words, the sum of intrinsic spin and orbital angular momentum, carried by the quarks of flavor  $f$ . In the limit of the sum rule as  $t \rightarrow 0$ , the total quark contribution to the nucleon spin is obtained. The contribution of the quark intrinsic spin ( $\frac{1}{2}\Delta\Sigma$ ) was measured at CERN/SMC, SLAC and DESY/HERMES. The gluon spin contribution ( $\Delta G$ ) is determined at CERN/COMPASS, RHIC/(STAR & PHEMIX) and SLAC. JLab at 12 GeV will also constraint the high  $x$  contribution to  $\Delta G$ .

## GPDs in Impact Parameter Space

As mentioned in II.4.2 GPDs depends on two longitudinal parton momentum fractions and on invariant transverse momentum transfer to the proton. Here we exemplify a particular case where the skewness parameter or the longitudinal momentum transfer,  $\xi$ , is zero. In this particular case, the GPDs, which are transformed to impact parameter [28] space, have the interpretation of a density of partons with longitudinal momentum fraction  $x$  and the transverse distance  $b$ , the impact parameter, from proton's center. The very well expected question to ask how could this particular case be related to GPDs since the longitudinal momentum transfer is the key parameter for all process where GPDs are accessible (detailed answer for this question can be found in [28] and [29]).

If the nucleon is in infinite momentum frame, its effective mass is also infinity. Therefore, its spatial structure in the transverse directions can be obtained directly from the Fourier transformation of the form factors.

So far the impact parameter space discussion is based on zero longitudinal momentum transfer. Once this restriction is removed, GPDs become genuine quantum

mechanical interference terms rather than being densities. The usual parton densities are given by squared wave functions and represent probabilities. On the other hand, GPDs are correlate wave functions for different parton configurations. In the case of having non-zero longitudinal momentum transfer, there exist an interesting physics encoded in GPDs in impact parameter space resulting from the Fourier transform from  $(p' - p)_\perp$  to transverse position  $b_\perp$  which can be seen in Fig. (7). In this representation GPDs describe simultaneously the longitudinal momentum of partons and their distance from the transverse center of the proton which means providing a fully three-dimensional picture of partons in a hadron.

The essential physical notion acquired from the presence of a non-zero momentum transfer in the t-channel identify the transverse separation of incoming and out going partons (Fig. 7). Thus, the overlap between these states decreases with higher momentum transfer. Moreover, the transverse shift of the partons depends on only  $\xi$  not on the momentum fraction  $x$ . Therefore, the information on transverse location of partons in the proton is not washed out when GPDs are integrated over  $x$ . As introduced in [30, 31], scattering amplitudes of hard exclusive processes allows to exploit the non-forward behavior of GPDs thus they become accessible through hard exclusive lepto-production of a photon which leaves the target intact.

## II.5 PHENOMENOLOGY OF GPDs

The indispensable scientific reality is that the richness in physics of GPDs become meaningful by experimental measurements. The previously mentioned essential tools, DIS and Drell-Yan ( $\pi p \rightarrow e^+e^-X$ ) processes etc., explores certain aspects of the hadron structure and offered a lot to re-form the experimental interpretation of the hadrons. Yet, we were missing out important pieces of physics informations encoded in GPDs of which the theoretical context provides a simultaneous embodiment for several types of processes such as:

- Compton induced processes,
  - leptonproduction of a real photon;
  - photoproduction of a lepton pair;
  - photoproduction of an electroweak boson;
- Hard re-scattering processes,

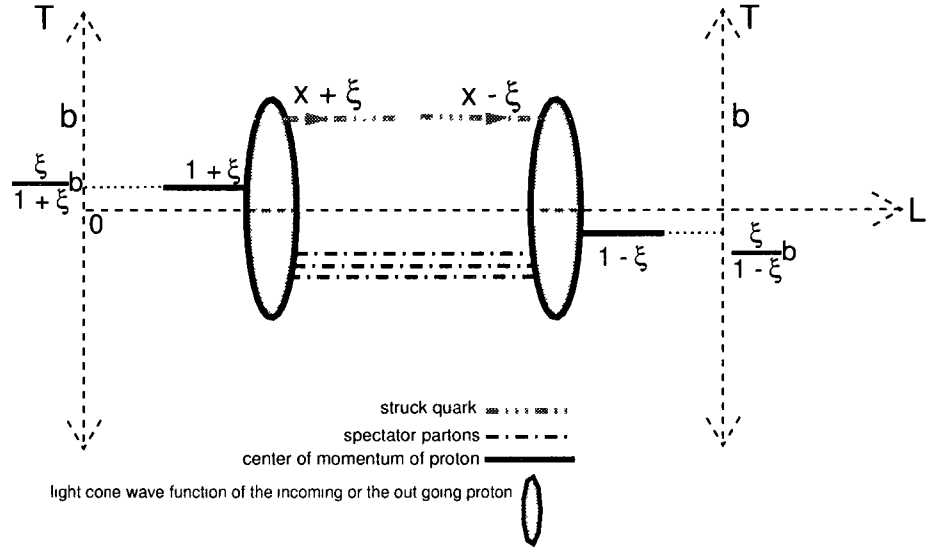


FIG. 7: Illustration of the encoded physics in GPDs in impact parameter space. DVCS probes partons at transverse position  $\mathbf{b}$ , with the initial and final proton state proton localized around zero but shifted relative to each other by  $2\xi\mathbf{b}/(1 - \xi^2)$  case. This picture is the representation of  $\xi$  region of  $\xi < |x| < 1$  which gives the location where a quark or an anti-quark is pulled out of and put back into the proton.

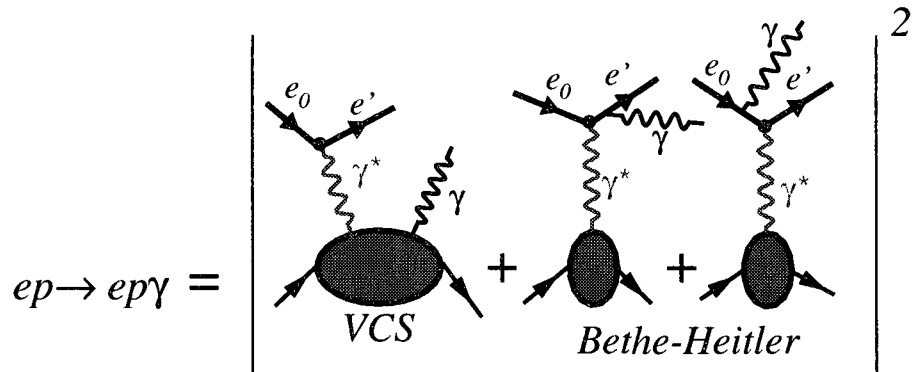


FIG. 8: Electro-production of real photon  $ep \rightarrow ep\gamma$

- leptonproduction of a light meson;
- leptonproduction of a meson;
- photoproduction of a heavy meson;
- Diffractive processes,
  - photoproduction of two jets;
  - leptonproduction of pion pairs.

The electro-production of real photon

$$ep \rightarrow ep\gamma \quad (48)$$

which has two contributing sub-processes Deeply Virtual Compton Scattering (DVCS) and Bethe-Heitler (BH) scattering (Fig. 8) is the main interest of GPDs studies together with the leptonproduction of mesons. In the context of this thesis, in this section I will discuss mainly DVCS and azimuthal angular dependence of electroproduction of real photon cross section.

### II.5.1 Deeply Virtual Compton Scattering

Among the known exclusive reactions, DVCS [21, 34, 35, 36, 37, 38, 39] is the cleanest to access to GPDs and it is the process of which theory is the most detailed and advanced, for example, effects to next-to-leading order [40, 41, 42] and sub-leading twist [43, 44, 45] are theoretically under control. Compton scattering itself is important because of the difference in the initial and final state of the proton. Along with the well established factorization, the DVCS process share similarities with the inclusive DIS, of which cross section is directly proportional to the imaginary part of the forward Compton amplitude. In conjunction with this similarity, it is known that DVCS (VCS in DIS kinematics) is dominated by single-quark scattering, and therefore the amplitude can be expressed in terms of the off-forward parton distribution, in other words GPDs [49, 50, 51]. Moreover, the information on the polarization of the virtual photon is contained in the azimuthal angle  $\phi$  between the hadron and lepton planes in the electroproduction of real photon. This angle corresponds to an azimuthal rotation around the momentum of the virtual photon, thus it is related with the angular momentum in this direction.

This cleanest and detailed access to the GPDs' exclusive dynamics at the amplitude level is provided by DVCS. However, in this exclusive process DVCS is not alone. Together with BH, DVCS contributes to the electroproduction of a real photon Fig.(8).

The two subprocesses, Fig.(8), of exclusive electroproduction of a real photon off the nucleon are two separate mechanism, however, the final state of the B-H is indistinguishable from that of the DVCS process. Thus, both mechanisms have to be added on the amplitude level and the differential real-photon electroproduction cross section is

$$d\sigma^{electroproduction} \propto |T_{BH}|^2 + |T_{DVCS}|^2 + I \quad (49)$$

where the interference term,  $I$  is  $T_{DVCS}T_{BH}^* + T_{DVCS}^*T_{BH}$  Fig. (10).

#### The Bethe - Heitler (BH) Process

The Bethe-Heitler (BH) process, or radiative elastic scattering, is illustrated in Fig. (8) in which the real photon is emitted by the either by incoming electron or the scattered electron rather than a quark. The BH amplitude is completely calculable in QED, together with the knowledge of the elastic nucleon form factors at small values

of  $t$ . The BH process has significance in the kinematics such as this experiment, E00-110, ran by enhancing the cross section through interference term, which ultimately provides accessibility to GPD where the DVCS cross section is small.

### II.5.2 Cross Section for the Electroproduction of the Photon

The most important task is to utilize the BH and Compton amplitudes to unravel the GPDs. In this regard, here in this sub-section I will discuss how to access the GPDs.

#### From Theory to Experiment

The GPDs depend on three variables,  $(x, \xi, t)$  only two of which are experimentally accessible. For example:

- the longitudinal momentum transfer,  $\xi$  is defined through detection of the scattered electron ( $\xi = \frac{x_B}{2-x_B}$ );
- the transverse momentum transfer,  $t$  is defined through detection of either the recoil proton or the emitted photon.

Yet, the longitudinal momentum fraction,  $x$  is integrated over, in consequence of the loop in the handbag diagram in Fig. (6). Another aspect which can be seen in Fig. 9, the evolution with  $\xi$  is not trivial and that measuring the integral over  $x$  of a GPD, at constant  $\xi$  will not define it uniquely. This means that GPDs enter the  $\gamma^*p$  amplitude through integrals of type

$$\mathbb{T}^{DVCS} \approx \int \frac{dx}{x - \xi + i\epsilon} GPD(x, \xi, t). \quad (50)$$

On account of time reversal invariance, GPDs are real valued, therefore the real and imaginary parts of this expression contain very distinct information on GPDs. The integral in Eq. (50) decomposes into real and imaginary part as

$$\int \frac{dx}{x - \xi + i\epsilon} GPD(x, \xi, t) = P \int \frac{dx}{x - \xi} GPD(x, \xi, t) - i\pi GPD(\xi, \xi, t) \quad (51)$$

In other words, the integrals (with a propagator as a weighting function) of GPDs are measured in order to access observables. One can access the separate terms in Eq. (51) through different spin and charge dependent observables. For example,

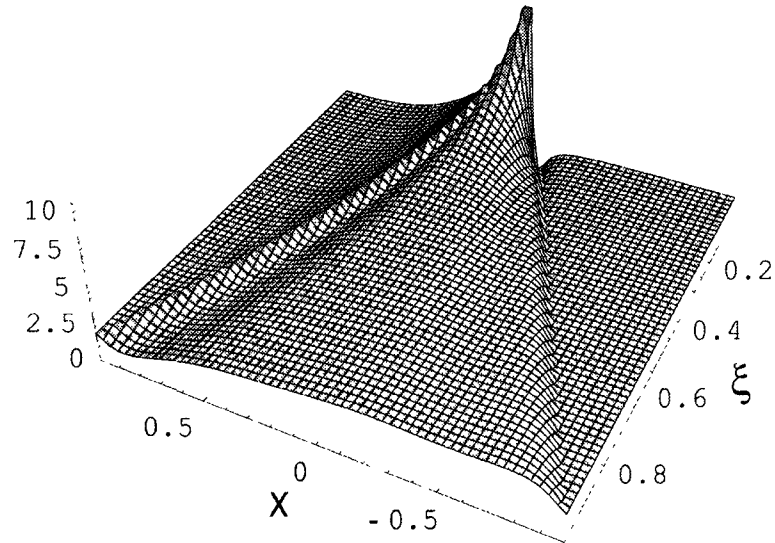


FIG. 9: Illustration of one particular GPD model [32, 33] for the GPD  $H$  as a function of  $x$  and  $\xi$  for  $t = 0$ . One identifies at  $\xi = 0$  a standard quark density distribution, with the rise around  $x = 0$  corresponding to the diverging sea quark contribution and the negative  $x$  part is related to anti-quarks. It is seen that the evolution with  $\xi$  is not trivial and that measuring the integral over  $x$  of a GPD, at constant  $\xi$  will not define it uniquely. (Figure is taken from [32])

in the region where the BH dominates the electroproduction cross section, the BH-DVCS interference term can be used through unpolarized beam charge cross section difference

$$\sigma^+ - \sigma^- \propto \Re \mathbb{T}^{DVCS} = P \int \frac{dx}{x - \xi} GPD(x, \xi, t), \quad (52)$$

where  $\sigma^-$  and  $\sigma^+$  are opposite lepton charge conjugation. Or, the cross section differences of opposite beam helicities

$$\sigma^{\rightarrow} - \sigma^{\leftarrow} \propto \Im \mathbb{T}^{DVCS} = -i\pi GPD(\xi, \xi, t). \quad (53)$$

The main difference between Eq. (52) and (53) is that the former measure the integral and needs a deconvolution to access the GPDs, on the other hand the later is the direct measurement of the imaginary part of the GPDs directly, but only along the line  $x = \xi$ .

In the kinematical region where DVCS dominates the electroproduction cross section, one can measure

$$\sigma^{DVCS} \propto \left| \int \frac{dx}{x - \xi + i\epsilon} GPD(x, \xi, t) \right|^2. \quad (54)$$

Here the challenge is similar as to the real part of this integral as mentioned in Eq. (52), a deconvolution (theoretically challenging task [46]) is necessary to access the GPDs directly.

One conventional concept that is widely used in experimental measurements is beam spin asymmetry (BSA), or single spin asymmetry (SSA) which is less complicated than cross section difference experimental but more complicated theoretically.

### Angular Dependence of the Cross Section

The  $ep \rightarrow ep\gamma$  cross section [34] mentioned in Eq. (49), which is formed by the physical observables that provide direct access to GPDs,

$$\frac{d\sigma}{dx_B dy dt d\phi d\varphi} = \frac{\alpha^3 x_B y}{16\pi^2 Q^2 \sqrt{(1 + \epsilon^2)}} \left| \frac{T}{e^3} \right|^2 \quad (55)$$

The cross section depends on (see Fig. 10)

- Bjorken variable  $x_B$ ,
- the squared transverse momentum transfer  $t = \Delta^2 = (p' - p)$ , where ( $p = (M, 0, 0, 0)$  and  $p'$  is the recoiled proton's momentum),



- the lepton energy fraction  $y = \frac{p(k_i - k_f)}{P\epsilon}$ ,
- $\epsilon = 2x_B \frac{M}{Q}$ ,
- $\phi$  is the angle between the leptonic plane and recoiled proton,
- $\varphi$  is defined in the kinematics in which the target nucleon is transversely polarized. In that convention  $\varphi$  is the angle between the polarization vector and the hadronic plane  $p' \otimes q'$  [34],

The amplitude squared is

$$T^2 = |T_{BH}|^2 + |T_{DVCS}|^2 + I \quad (56)$$

where  $I = T_{DVCS}T_{BH}^* + T_{DVCS}^*T_{BH}$ . These azimuthal dependence of each three term read

$$|T_{BH}|^2 = \frac{e^6}{x_B^2 y^2 (1 + \epsilon^2)^2 t P_1(\phi) P_2(\phi)} \{c_0^{BH} + \sum_{n=1}^2 c_n^{BH} \cos(n\phi) + s_1^{BH} \sin(\phi)\}, \quad (57)$$

$$|T_{DVCS}|^2 = \frac{e^6}{y^2 Q^2} \{c_0^{DVCS} + \sum_{n=1}^2 [c_n^{DVCS} \cos(n\phi) + s_n^{DVCS} \sin(n\phi)]\}, \quad (58)$$

$$I = \frac{\pm e^6}{x_B y^3 t P_1(\phi) P_2(\phi)} \{c_0^I + \sum_{n=1}^3 [c_n^I \cos(n\phi) + s_n^I \sin(n\phi)]\}, \quad (59)$$

the  $\pm$  signs in interference term corresponds negatively charged lepton in the case of (+), and positively charged lepton in the case of (-). The  $\phi$  dependence of the cross section originates from the Fourier coefficients in Eq. (57,58, and 59) and BH propagators,

$$Q^2 P_1 \equiv (k - q_\gamma^2) = Q^2 + 2k \cdot \Delta, \quad Q^2 P_2 \equiv (k - \Delta)^2 = -2k \cdot \Delta + \Delta^2, \quad (60)$$

The Fourier coefficients expressed in Eq. (57,58, and 59) are discussed in details in [34]. Here in this thesis, I will discuss only  $s_n^I$  of Eq. 59 being related to the BSA (or SSA).

### II.5.3 Beam Spin Asymmetry (BSA)

The measurement of the cross section in Eq. (58) with its decompositions, allows direct access to physical Compton Form Factors (CFFs) [34] which are linear combination of GPDs. Nevertheless, experimentally it requires to calculate, acceptance,

normalization. On the other hand, in spite of some restrictions, one can also extract the imaginary part of the interference term via  $ep \rightarrow ep\gamma$  reaction with a polarized electron beam by measuring the out-of-plane angular dependence of the produced photon [47]. Later it was introduced in [33, 48] as Single Spin Asymmetry or BSA. The BSA can be studied with the facilities having one type of lepton beam, such CEBAF at Jlab. Having the polarized electron beam at CEBAF allows us to extract BSA as helicity difference which removes the background BH cross section. This helicity difference is directly proportional imaginary part of the DVCS amplitude. The BSA for a longitudinal polarized beam and unpolarized proton target is defined as

$$BSA(\phi) = \frac{d\sigma^{\rightarrow} - d\sigma^{\leftarrow}}{d\sigma^{\rightarrow} + d\sigma^{\leftarrow}} \quad (61)$$

where  $\rightarrow$  denotes beam spin parallel and  $\leftarrow$  denotes anti-parallel to the beam direction. Following the discussion in [34], beam spin asymmetry becomes,

$$BSA_{\phi} \propto s_{1,unp}^I \sin \phi, \quad (62)$$

where

$$s_{1,unp}^I \sin \phi = 8K\lambda y(2-y)\Im m \mathcal{C}_{unp}^I(\mathcal{F}). \quad (63)$$

Here in Eq. (63)  $\lambda$  is the helicity of the electron beam,  $y$  is the lepton energy fraction  $K$  is the  $1/Q$  power suppressed kinematical factor,

$$K^2 = \frac{-t}{Q^2}(1-x_B)(1-y-\frac{y^2\epsilon^2}{4})(1-\frac{t_{min}}{t})\{\sqrt{1+\epsilon} + \frac{4x_B(1-x_B) + \epsilon^2 t - t_{min}}{4(1-x_B)}\frac{t-t_{min}}{Q^2}\}. \quad (64)$$

$K^2$  vanishes at the kinematical boundary of  $t = t_{min}$ ,

$$-t_{min} = Q^2 \frac{2(1-x_B)(1-\sqrt{1+\epsilon^2}) + \epsilon^2}{4x_B(1-x_B) + \epsilon^2} \approx \frac{x_B^2 M^2}{1-x_B}. \quad (65)$$

The Compton Form factor, a twist-2 term, in Eq. (63) is linear combination of GPDs

$$\mathcal{C}_{unp}^I(\mathcal{F}) = F_1 \mathcal{H} + \xi(F_1 + F_2)\tilde{\mathcal{H}} - \frac{t}{4M^2}F_2 \mathcal{E}. \quad (66)$$

As mentioned in the relation 53, along the line  $x = \pm\xi$  one has,

$$\Im m \mathcal{H} = \pi \sum_q e_q^2 (H^q(\xi, \xi, t) - H^q(-\xi, \xi, t)), \quad (67)$$

$$\Im m \tilde{\mathcal{H}} = \pi \sum_q e_q^2 (\tilde{H}^q(\xi, \xi, t) + \tilde{H}^q(-\xi, \xi, t)), \quad (68)$$

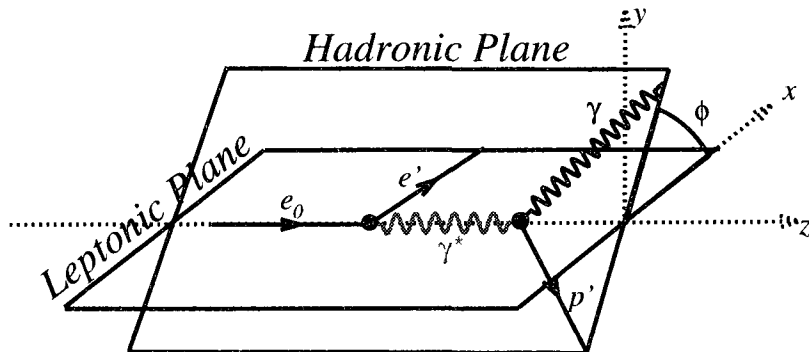


FIG. 10: Kinematics of Electroproduction of Real Photon in the target rest frame. The three momentum of the virtual photon ( $\gamma^*$ ) is along the z-direction. The lepton three momenta form the leptonic scattering plane, while the recoiled proton and outgoing real photon define the hadronic scattering plane. In this reference system the azimuthal angle between the leptonic plane and the recoiled proton is  $\phi$ .

$$\Im m\mathcal{E} = \pi \sum_q e_q^2 (E^q(\xi, \xi, t) - E^q(-\xi, \xi, t)). \quad (69)$$

The studies in GPDs are model dependent, however, regardless of the model one uses, the  $H^q$  type GPDs dominate the  $BSA_{LU}$  in consequence of

- the second term in Eq. (66) is suppressed by  $\xi$  because of the fact that even in the fixed target kinematics  $\xi$  is not usually larger than 0.2
- the third term in Eq. (66) is  $t$  suppressed by about a factor of 25 on the proton for  $t$  values around  $0.15 \text{ GeV}^2$

Among the all  $H^q$  GPDs, for a proton target, the GPD  $H^u$  will provide the major contribution to  $\mathcal{C}_{unp}^I(\mathcal{F})$  because of the u quark dominance in proton.

## CHAPTER III

### EXPERIMENTAL STUDIES ON DVCS

The difficulty in the experimental studies of GPDs is the measurement of exclusive process, or rather low cross section, at the highest possible momentum transfer  $Q^2$ . In order to acquire this, high beam energy and luminosity, as well as large acceptance and high resolution detectors are required. Therefore, in order to avoid theoretical complication along with the challenges mentioned, the DVCS, simplest process to access the GPDs, has become more appealing for experimental studies.

#### III.1 COLLIDER EXPERIMENTS

The  $p(e, e'\gamma)X$  cross section (integrated over  $\phi_{\gamma\gamma}$ ) has been measured in hard exclusive photon electroproduction at HERA collider by the experiments H1 [51, 52, 53] and ZEUS [54, 55]. The HERA data cover a wide kinematics range at low  $x_B$ , with central values of  $Q^2$  and  $W$  from 8 to 85  $GeV^2$  and 45 to 130  $GeV$ , respectively. The published results of these two experiments shown in Fig.(11). The model calculations are dominated by the gluon GPD contribution.

#### III.2 FIXED-TARGET EXPERIMENTS

It was shown in section II.5.2 that in the hard exclusive real-photon leptonproduction the interference term (Eq. (59)) of the BH and DVCS processes is a rich source for extracting wealth information on GPDs. In this regard, the first published GPD-related experimental results were BSA measured in fixed-target experiment at HERMES at HERA [56] with a positron beam and by CLAS at Jefferson Laboratory [57] with an electron beam (Comparison of the results can be seen in Fig. 12).

#### HERMES

The HERMES collaboration performed their first BSA measurements at average kinematics of  $\langle Q^2, x_B, t \rangle = (2.6 \text{ GeV}^2, 0.11, -0.27 \text{ GeV}^2)$  [56]. The average beam polarization at HERMES was 55% and to compensate not detecting the recoil proton the  $M_X^2$  technique (resolution of 2  $GeV^2$ ) is used. Following the first experiment, the HERMES collaboration has measured

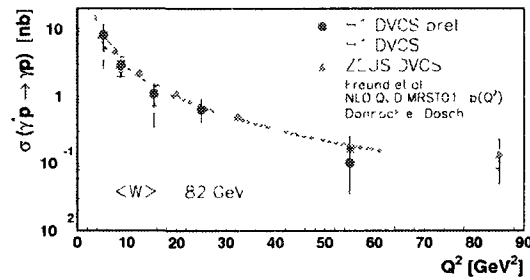


FIG. 11:  $Q^2$ -dependence of the differential  $\gamma^*p \rightarrow \gamma p$  cross section measured by H1 and ZEUS. In addition to the H1 and ZEUS data, the solid curve shows NLO  $pQCD$  calculation using a GPD parametrization based on MRST2001 PDFs and a  $Q^2$  dependent  $t$ -slope  $b(Q^2)$  describing the factorized  $t$ -dependence [58].

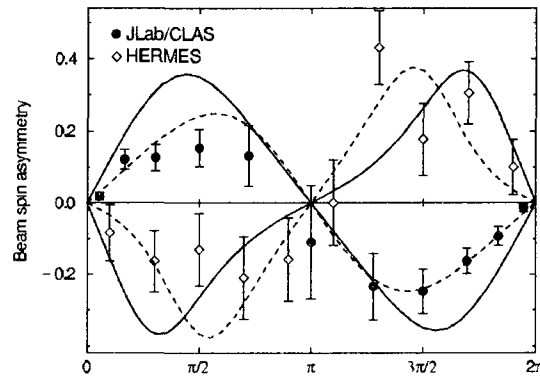


FIG. 12: The  $\phi_{\gamma\gamma}$  dependent BSA measurements performed at HERMES [56] and CLAS [57]. Since the charge of the lepton beams used in these two facilities were opposite, the opposite sign in BSA is observed. GPD models [59, 60] have been overlaid (solid lines) and show that theory and data are in good agreement. Dashed lines show a phenomenological fit to the data [61].

- the beam charge asymmetry [62],
- transversely polarized target asymmetries [63],
- longitudinally polarized target asymmetries [64],
- an extensive set of BSA [65],
- an experiment with a recoiled detector [66] and achieved exclusivity through  $H(e, e'\gamma p)$  triple coincidence detection [67].

## CLAS

The first CLAS BSA measurements on proton target performed at average kinematics of  $\langle Q^2, x_B, t \rangle = (1, 25 \text{ GeV}^2, 0.19, -0.19 \text{ GeV}^2)$  [57]. The average beam polarization at CLAS was 70%.  $H(e, e'p)\gamma$  and  $H(e, e'p)\pi_0$  events were separated by a line shape analysis on the missing mass of the  $H(e, e'p)X$  process.

The continuation of the CLAS DVCS program with standard CLAS configuration [68] measured the longitudinal target spin asymmetry in the  $\vec{p}(e, e'p\gamma)$  on a polarized  $NH_3$  target [69].

## III.3 DVCS AT JLAB

### III.3.1 Hall A DVCS Program

The initial experiments in Hall A DVCS program were E00-110 [70] and E00-106 [71]. These experiments measured the cross sections of the  $H(e, e'\gamma)p$  and  $D(e, e'\gamma)pn$  reactions at  $x_B = 0.36$  with an incident electron beam of  $5.75 \text{ GeV}$ . The published results of these experiments are [72, 73, 74]. The helicity dependent cross section as a function of  $\phi_{\gamma\gamma}$  in four bins of  $t$  are displayed in Fig. (14). The dominance of the effective twist-2 term  $s_1^f$  (Eq. 59) can be seen in the helicity dependent cross sections in Fig. (14). The results displayed in Fig.(15) demonstrates a  $Q^2$  independent behavior within the statistics in each  $t$  bin. Thus, from the experimental point of view, the DVCS factorization results in leading twist dominance at the same scale of  $Q^2 \geq 2\text{GeV}^2$  as in DIS.

The Neutron DVCS experiment in Hall A measured helicity dependent DVCS cross section on Deuterium target. The analysis method in [73] introduces constraints on the Neutron and Deuteron DVCS.BH interference terms  $\Im m C_{imp}^I$ . The Neutron

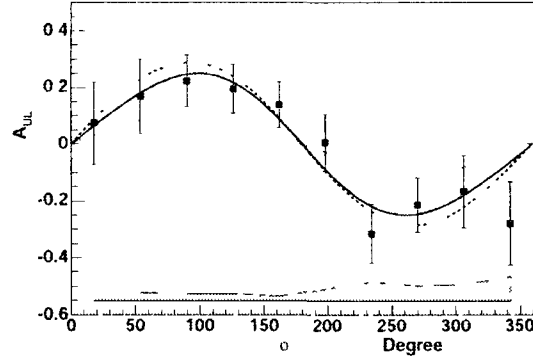


FIG. 13: CLAS longitudinal target spin asymmetry [69]. The experiment performed for average kinematics of  $\langle Q^2, x_B, t \rangle = (1.82 \text{ GeV}^2, 0.16, -0.31 \text{ GeV}^2)$ . The solid curve is a fit to the data. The dashed and dotted curves are from  $\xi$ -dependent VGG model with  $\tilde{E} = 0$  and  $\tilde{E} = 0$ . The dotted curve includes only H. The dashed curve includes both H and  $\tilde{H}$ .

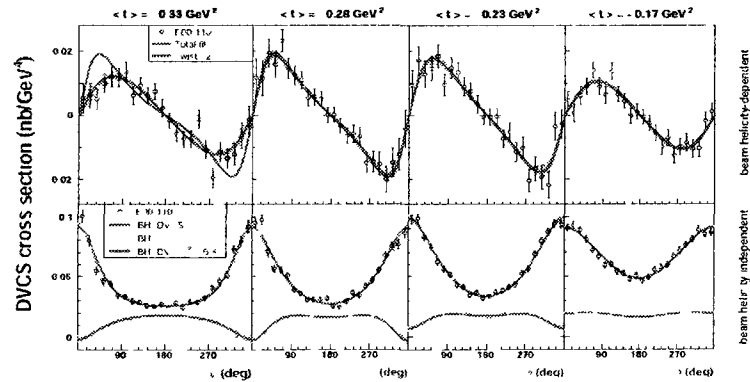


FIG. 14: Helicity dependent (top) and independent (bottom) cross section at  $Q^2 = 2.3 \text{ GeV}^2$  for the Hall A DVCS. The values of  $-t$  from right to left 0.17, 0.23, 0.28, and  $0.33 \text{ GeV}^2$ . Each distribution is fitted with the form of Eq.(59).[70]

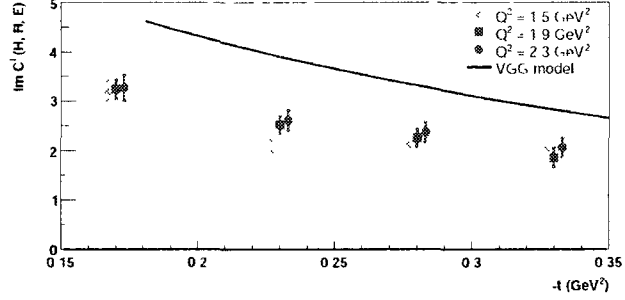


FIG. 15: Imaginary part of the effective interference term  $\mathcal{C}_{unp}^I$  extracted from the helicity dependent data of Fig.(14).

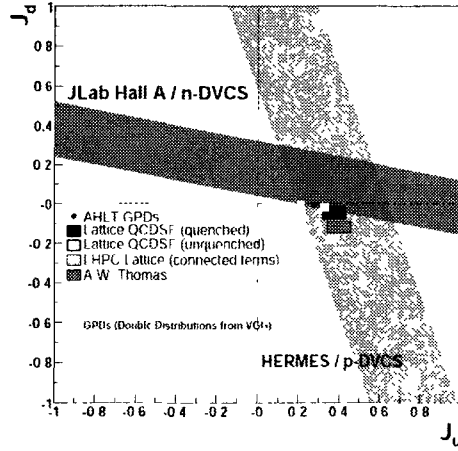


FIG. 16: Experimental constraints on the total up and down quark contributions to the proton spin. JLab Hall A Neutron experiment [73] and HERMES transversely polarized proton [63]. The theory/model values displayed [75, 76, 77, 78, 79] respectively as listed in the figure.



Kin.	$s$ ( $GeV^2$ )	$Q^2$ ( $GeV^2$ )	$x_B$	$\theta_e$	$\theta_{\gamma^*}$	$P_e$ ( $GeV^2$ )
1	3.5	1.5	0.36	15.6	22.3	3.6
2	4.2	1.9	0.36	19.3	18.3	2.9
3	4.9	2.3	0.36	23.9	14.8	2.3

TABLE 1: Three kinematical settings of the E00-110 experiment. Three different  $Q^2$  settings were chosen aiming to maximize the highest  $Q^2$  value and  $Q^2$  range which keeps above the main resonance.

interference signal fitted by varying the parameters of the E GPD with the VGG model [32] (see also chapter IX). Therefore, a model dependent constraint is entailed on the Ji sum rule values of  $(J_u, J_d)$  illustrated in Fig. (16). The HERMES DVCS collaboration obtained a similar constraint in [63]. The common features in these two experiments are having constraints on the model at one value of  $x_B$ , and the model is integrated over  $x$  at fixed  $\xi$  value to be able to extract the sum rule estimate. The HERMES results, lattice QCD calculations other phenomenological estimates are displayed along with the [73]'s  $J_u$  and  $J_d$  values in Fig. 16.

### Recent 6 GeV Experiments

After these promising results two new experiments E07-007 [82] and E08-025 [83] approved to run in Hall A and both experiments completed in Fall 2010. The former measured the DVCS helicity independent cross section in three kinematics Table -1 at two separate beam energies in each kinematics. The later measure the DVCS cross section on the Deuteron at the same values at E03-106 at two separate beam energies. One other important difference with these two recent experiments than the old experiments is that proton array was not used and extended electromagnetic calorimeter is used.

### III.3.2 CLAS DVCS Program

An extensive DVCS program started with the experiment [57] in which real photon was not detected. Later, a calorimeter was constructed to provide complete  $2\pi$  photon coverage in the forward direction. All final particles of the  $ep \rightarrow ep\gamma$  are detected in CLAS. The published results of the CLAS DVCS experiments can be

found in [80, 81] (17). A longer experiment ran in 2009 at CLAS [84] which will significantly improve the statistical precision of the CLAS DVCS data.

A recent DVCS experiment completed data taking with the longitudinally polarized  $NH_3$  target [85]. The new experiment, in comparison to [69] ran with the new electromagnetic calorimeter. This experiment results will shed lights on the importance of target spin asymmetry which is mostly sensitive to  $\widetilde{\mathcal{H}}(\xi, t)$  and will be discussed in this thesis in chapter IX.

One significant development is the HD-ice target, which had been used at the BNL-LEGS facility, now has been transferred to JLab. An electron beam test is projected for the end of the 2011 photo-production run. If it will be successful, a new intense study of transverse polarization observables for the DVCS will be feasible [87].

CLAS had an pioneering [88] DVCS experiment in 2010 on a  $^4He$  target. It is expected that with this experiment the  $\phi$ -distribution of the coherent DVCS BSA can yield the real and imaginary parts of the CFF of the coherent GPD.

### III.4 FUTURE OF DVCS MEASUREMENTS

The kinematical coverage of the existing facilities along with the future coverages are displayed in Fig.(18). The complementary facilities will continue to study GPDs through exclusive reactions.

#### III.4.1 Jefferson Lab 12 GeV

Jefferson Lab will be the first facility in the world capable of study the exclusive processes in a comprehensive way via providing high luminosity and large acceptance. What 12 GeV upgrade will provide is the simultaneous accesses to small  $t$ , large  $x$ -range along with high  $Q^2$ . For example, the design luminosity with the upgraded CLAS detectors is  $10^{35}/(s\text{ cm}^2)$ , with a large phase space acceptance. At this luminosity, the Hall B dynamic nuclear polarization for  $NH_3$  target will achieve a longitudinal polarization of 80% . The Hall A and Hall C spectrometers will allow to perform experiments at luminosities  $\geq 10^{37}/s\text{ cm}^2$  for neutral channels  $\gamma, \pi^0$  at low  $t$  and up to  $4 \times 10^{38}/s\text{ cm}^2$  for charged channels  $\pi^\pm, K^\pm$ . Among the approved experiments for 12 GeV program there exist Hall A DVCS experiment Hall A DVCS (E12-06-114), Hall B DVCS (E12-06-119). Some of the possible measurement with

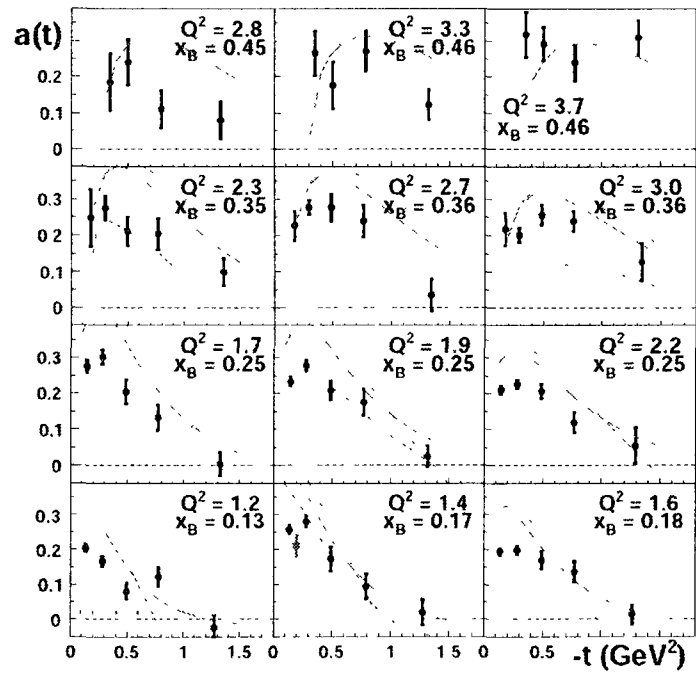


FIG. 17: Beam spin asymmetry  $\sin(\phi_{\gamma\gamma})$  moment from the CLAS DVCS experiment [80]

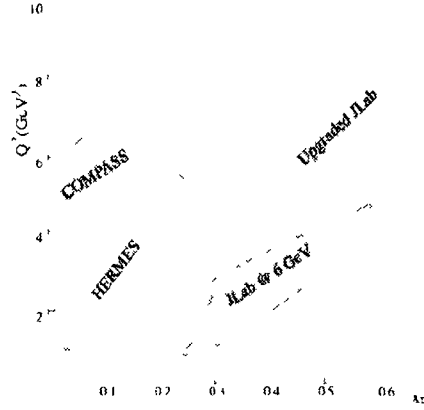


FIG. 18: Kinematics coverage for fixed target experiments. COMPASS at 190 GeV, HERMES 27.6 GeV, JLab 6 GeV (now), with upgrade 11 GeV.

upgraded JLab:

- BSA, longitudinal and transverse target-spin asymmetries for DVCS and meson production,
- separation of different GPDs,
- absolute cross section measurements,
- exploration of double DVCS process to map  $x$  and  $\xi$  independently

### III.4.2 DVCS Measurements with Higher Beam Energies

CERN COMPASS collaboration proposes to measure DVCS in high energy muon scattering at low  $X_B$  through triple coincidence  $H(\mu^\pm, \mu^\pm, \gamma p)$  detection [89].

A future electron ion collider, with luminosity several order of magnitude higher than any other existing facilities would open a new era in GPD studies. The essential feature for the new facilities is to maximize the luminosity to measure the differential cross sections in all kinematic variables. Moreover, a collider can deliver

both longitudinally and transversely polarized beams without the unpolarized target background.

## CHAPTER IV

### EXPERIMENTAL SETUP

The DVCS experiments, DVCS on proton E00-110 and DVCS on neutron E03-106 ran between the dates September 21<sup>st</sup> and December 9<sup>th</sup> 2004. Both experiments completed in Hall A of Thomas Jefferson National Accelerator Facility in Newport News, Virginia. In this chapter I describe Continuous Electron Beam Facility (CEBAF) at Thomas Jefferson National Accelerator Facility (Jefferson Lab), standard Hall A instrumentation, and dedicated detectors used for DVCS experiments.

#### IV.1 CEBAF AT JEFFERSON LAB

The CEBAF (Fig. 19) at Jefferson Lab (JLab) studies the structure of nuclei and hadrons and the fundamental interactions in the region below the high-energy *asymptotically free* regime. CEBAF's 6 GeV continuous wave electron beam is, in many respects, an ideal probe for the study of strong QCD region because the electromagnetic interaction is well understood, and the wavelength of the electron at this energy is a few percent of the nucleon's size. The availability of polarized electron beams extends the capabilities of the facility to include variety of different experiments.

Being the first continuous lepton beam facility using the superconducting cavities, CEBAF at JLab initially designed to accelerate electrons up to 4 GeV by circulating the beam up to five times through two superconducting linacs, each producing an energy gain of 400 MeV per pass. Among the existing injector technologies electrons are being injected into the accelerator by a polarized gun which allows to obtain a longitudinal polarized electron beam. Depending on the photo-cathode used, the polarization can go up to 85%. In the polarized gun a strained GaAs cathode is illuminated by 1497 MHz gain-switched diode laser, operated at 780 nm. A 5 MeV Mott polarimeter is used at the injector to measure the polarization and the polarization vector can be oriented with a Wien filter. In our experiment polarization of the electron beam was around 77%.

The existing three experimental Halls have been operational since 1997 and the current of each Hall can be controlled independently. Each linac contains 20 cryomodules with a design accelerating gradient of 5 MeV/m, with the in situ processing it resulted in an average gradient excess of 7 MeV/m, which has made it possible to

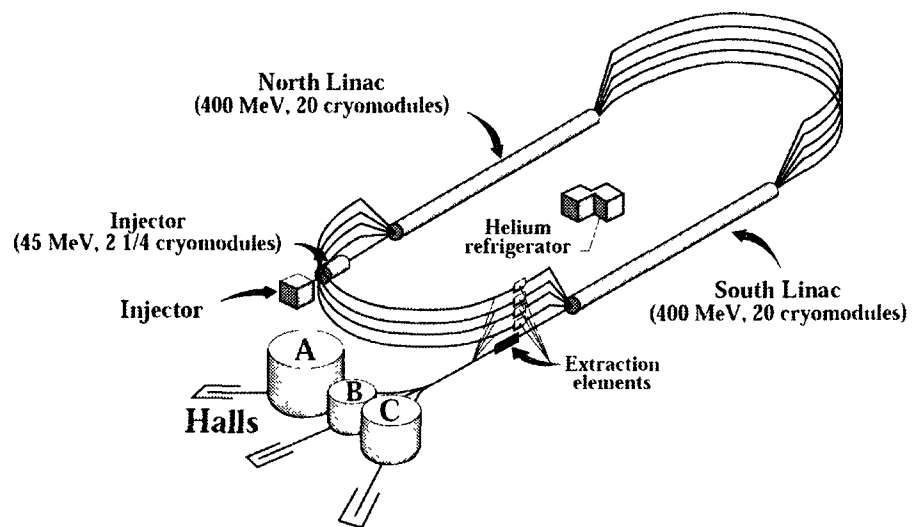


FIG. 19: Continuous Electron Beam Facility at JLab The electron beam is produced at the injector by illuminating a photo-cathode and then accelerated to 60 MeV. The beam is then further accelerated in North and South linacs.

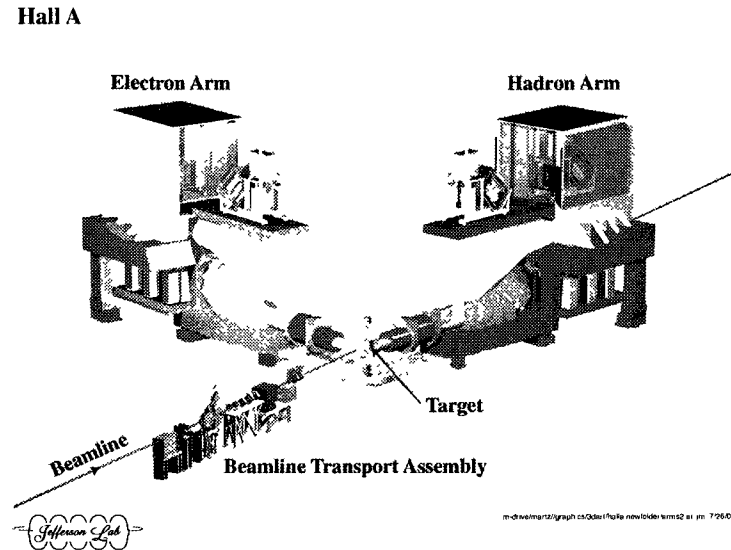


FIG. 20: Experimental Hall A  
General View of the beamline instrumentation, target, L-HRS (Electron Arm),  
R-HRS (Hadron Arm) and detector packages.

accelerate electrons to 5.7 GeV [90]. Technically the maximum achievable current at Jab is  $200 \mu\text{A}$  CW, which can be split arbitrarily between three interleaved 499 MHz electron bunches. One such electron bunch, which is unique in its properties, can be separated from the other two, and can be delivered to any one of the Halls with the maximum beam energy.

## IV.2 EXPERIMENTAL HALL A

The DVCS experiments ran at the experimental Hall A (Figs. 20 and 22) at Jefferson Lab, which allows to make high precision measurements and to run the experiments with high luminosity which has a typical value of  $10^{38} \text{cm}^{-2} \text{s}^{-1}$ . The central elements of the experimental Hall A are; two high resolution spectrometers, beamline instruments, and target system. In the coming sub-section I briefly discuss each element.



### IV.2.1 High Resolution Spectrometers

The central standard elements of experimental Hall A are two High Resolution Spectrometers (HRS)(Fig.20). These two identical spectrometers are:

- The Left HRS (L-HRS) is located on the left hand side of the Hall A, and was initially dedicated to electron momentum measurements.
- The Right HRS (R-HRS) is located on the right hand side of the Hall A, and was initially dedicated to hadron momentum measurements.

Both devices provide a momentum resolution of the order of  $\delta p/p \sim 10^{-4}$  and a horizontal angular resolution around 2 mrad at a design maximum central momentum of 4 GeV/c. The vertically bending design includes a pair of superconducting quadrupoles followed by a 6.6 m long dipole magnet. Following the dipole is a third superconducting quadrupole. The second and third quadrupoles of each spectrometer are identical in design and construction because they have similar field and size requirements[90].

In the DVCS experiments L-HRS used for measurements of the leptonic part of the reaction, and R-HRS used only for monitoring the luminosity during experiment.

### Detector Package

Experimental Hall A spectrometers consists of detector packages designed to perform various function to characterize the charged particles passing through the spectrometer. These detector packages are located in a shield hut of each HRS (see Fig. 20) and their configuration can be changed according to meet the needs of the experiment at Hall A. The data package includes the following elements in most of the configurations (can be seen in Fig. 21):

- Detector Shielding: Consists of the Line-of-Sight Block (LSB) and the Shield Hut (SH). The LSB is a two meter thick concrete block located 2 m from the target on top of Q1 and Q2. It moderates the pion flux produced at the target and thus reduces the muon rates in the detectors. The detector package and all Data- Acquisition (DAQ) electronic are located in SH to protect the detector against radiation from all direction. The radiation level inside the SH is below 1 mrem per hour at a luminosity of  $10^{38} cm^{-2}s^{-1}$ . At that luminosity the rate of a single spectrometer detector can be a few hundred kHz.

- Tracking: A pair of Vertical Drift Chambers (VDCs) provide tracking information in each HRS. VDCs allow a simple analysis algorithm and high efficiency with a small acceptance.
- Triggering: There exist a trigger system in detector package to activate the DAQ electronics. There are two primary trigger scintillator planes, S1 and S2. Each plane is composed of six overlapping paddles made of thin plastic scintillator to minimize hadron absorption.
- Particle Identification: The long path from the target to the HRS focal plane (25 m) allows accurate time-of-flight identification in coincidence experiments. The time-of-flight between the S1 and S2 planes is also used to measure the speed of particles  $\beta$ . A gas Cherenkov detector filled with  $CO_2$  at atmospheric pressure is mounted between the S1 and S2. The detector allows an electron identification with 99% efficiency and has threshold for pions at 4.8 GeV/c. Another important part of the particle identification detectors is two layers shower detectors which are installed in each HRS. These layers are perpendicular to the particle track. Combination of the gas Cherenkov and shower detectors provides a pion suppression above 2 GeV/c of a factor of  $2 \times 10^5$ .
- The Focal Plane Polarimeter (FPP): The FPP measures the polarization of recoil protons and can be installed in either HRS.

During the DVCS experiments L-HRS provided measurements with a momentum resolution of the order of  $\delta p/p \sim 10^{-4}$  and a horizontal angular resolution around 1 mrad which provided perfect measurement of the leptonic part of the reaction, (e.g.  $x_{bjk}, Q^2$ ). Having a rather small acceptance (about  $60 \cdot 10^{-3} \otimes 120 \cdot 10^{-3} sr$ ), resulted in a small acceptance for the virtual photon direction.

#### IV.2.2 Beamline Instrumentation

The beamline instrumentation (shown in Fig.22) in experimental Hall A consists of two polarimeters, Compton and Møller, beam position monitors (BPM), and beam current monitor (BCM). These necessary instruments provide to measure simultaneously the properties of the beam; to control and maintain accuracy of beam energy, polarization, position, direction, size and stability of the beam at the target location. Here, I will briefly discuss the characteristics of these instrumentation.

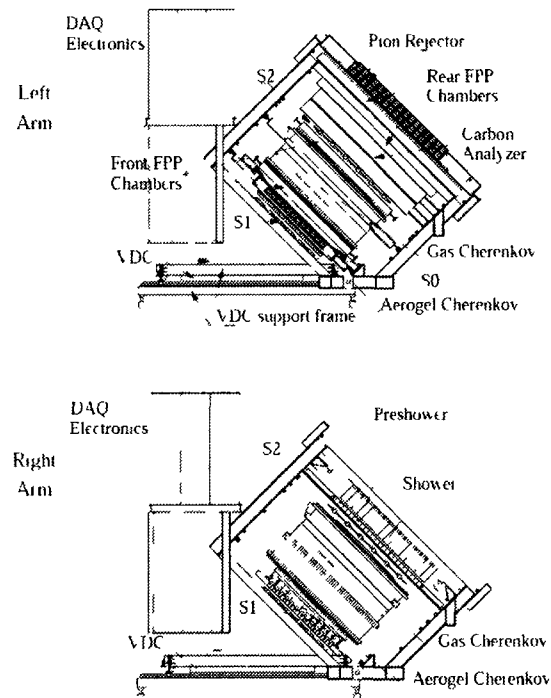


FIG 21 Side-view the most frequently used individual elements of the detector system are indicated in the configuration. The position DAQ of each detector package, VDC support frame, and the S1, Čerenkov, S2 plates relative positions are drawn

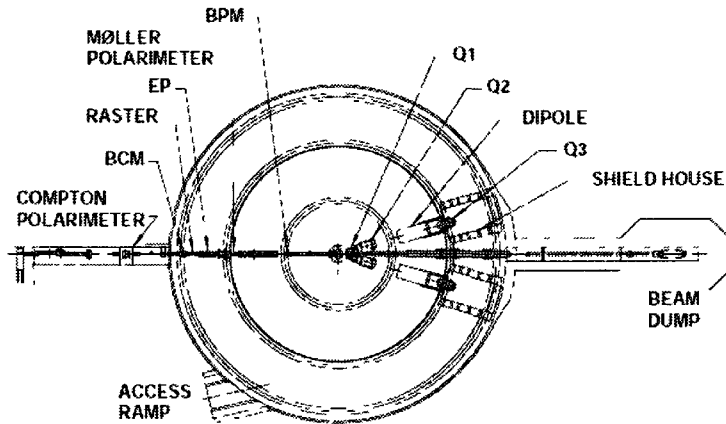


FIG. 22: Schematic top view of experimental Hall A, indicating the location of Compton and Møller polarimeters, the beam current monitors (BCM) and the beam position monitors (BPM) upstream of the target. In addition to beam line components, the locations of the components of one the high-resolution spectrometers (Q1, Q2, dipole, Q3 and the shield house), the beam dump and the truck access ramp are indicated.

The experimental Hall A uses polarized electron beam in an important part of its physics program and the measurement of the polarization delivered beam. In order to do, the beamline is equipped with two polarimeters, Compton Polarimeter and Møller Polarimeter.

### Compton Polarimeter

The Compton polarimeter provides concurrent measurement of the beam polarization as a non-invasive technique. Extracting the polarization of the electron beam by Compton polarimeter is the measurement of the counting rate asymmetry for the

opposite beam helicities in the elastic scattering of electrons off photons. The interaction of the electron beam with the photon target does not change the properties of the beam so that the beam polarization can be measured simultaneously while running the experiment. The Compton polarimeter consists of (shown in Fig.23):

- **Magnetic chicane:** Consists of four dipoles, is used to deflect the electron beam from the regular direction of the beam to the cavity axis.
- **Photon Beam Source:** The photon beam is maintained by a ND:YAG laser beam ( $\lambda = 1064mm$ ) delivering 230 mW of power
- **Optical Cavity:** A resonant Fabry-Pérot cavity is used as a power amplifier for the photon beam to increase the Compton interaction rate. Fabry-Pérot cavity comprising two identical high-reflectivity mirrors, amplifies the photon density at the Compton interaction point with gain around 7000 [91].
- **Electron Detector:** Located few mm above the primary beam in front of the fourth dipole, is composed of four silicon micro-strip detectors. Electron detector allows us to calculate the momentum of the electrons by re-constructing the electron trajectories.
- **Electromagnetic Calorimeter:** A Lead Tungstate ( $PbO_4$ ) calorimeter

The vertically deflected electron beam crosses the photon beam at the center of Fabry-Pérot cavity. Subsequently, the backscattered photons are detected at the electromagnetic calorimeter and the electrons are detected by electron detector. Finally, non-interacted electrons reach the target.

The accuracy of a Compton measurement is directly proportional to the square root of the number of events and to the analyzing power of the polarimeter which in fact, is proportional to the electron beam energy. In our experiment a 1% statistical error could be achieved in 2.5 hours of data taking. Compton data was taken with the normal DVCS data taking in progress, we can average over time periods to be able to neglect the statistical error.

### **Møller Polarimeter**

The polarization measurements with the Møller polarimeters are invasive due to solid target, nevertheless they are widely used for electron beam polarization measurements in the GeV energy range. A Møller polarimeter exploits the Møller scattering

of polarized electrons off polarized atomic electrons in a magnetic foil. Schematic layout of the experimental Hall A Møller polarimeter is shown in Fig.24. The Hall A Møller polarimeter consists of:

- **Polarized Electron Target:** Consists of a ferromagnetic foil as a target of polarized electrons. The polarimeter target system provides a target polarization that has both longitudinal and transverse polarization by tilting the target foil at various angles to the beam in the horizontal plane.
- **Three Quadrupole Magnets:** These quadrupole magnets make it possible to keep the position of all polarimeter elements unchanged within the energy range of the electron beam.
- **A Dipole Magnet:** The dipole is the main element of the polarimeter magnetic system by providing the energy analysis, thus separating the Møller scattered electrons from other type scattered electrons to surpass the background. In addition to this, by bending the Møller electrons, it allows detection away from the electron beam.
- **Detector:** The detector is located in the shielding box downstream of the dipole and it consists of lead glass calorimeter modules which has two arms to be able to detect two scattered electron in coincidence [92].

The helicity driven asymmetry of the coincidence counting rate is used to complete the beam polarization measurement. The Hall A Møller polarimeter provides accurate measurement in the energy range 0.8 to 5.0 GeV and can be used for measurements with beam currents between 0.5-5.0  $\mu A$ . A typical Møller measurement takes an hour and providing a statistical accuracy of about 0.2%.

### **Statistical Uncertainties of the Polarimeters**

Polarization measurements often account for the main systematic uncertainty for polarized electron beam experiments. Having used two different polarimeters, introduces two different sources for systematic uncertainty for DVCS experiment. The dominant uncertainty of the Møller polarimeter comes from the uncertainty in the target polarization, while that of Compton polarimeter originates from its low analyzing power. The Møller polarimeter is used at low beam current, and the current regime delivered at JLab is higher than the operational limits. Therefore the current

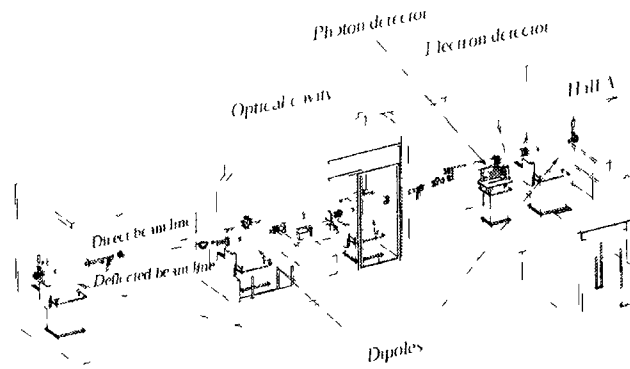


FIG. 23: Schematic layout of the Compton polarimeter at Hall, A showing the four dipoles of the chicane, the optical cavity, and the photon and the electron detectors.  
Layout of the Compton polarimeter,

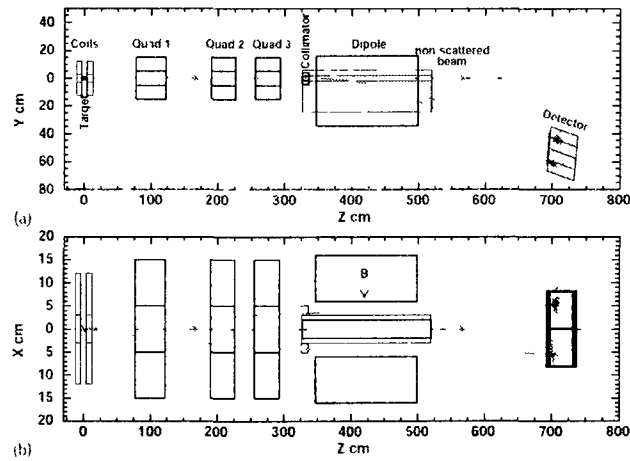


FIG. 24: Top and side view of the Møller polarimeter at Hall A. The trajectories displayed belong to a simulated event of Møller scattering at  $\theta_{CM}=80^\circ$  and  $\phi_{CM} = 0^\circ$  at a beam energy of 4 GeV.

is reduced at the injector, either by attenuating the laser light or with a slit at the copper. Either way, the polarization of the beam might change which introduces another uncertainty for Møller polarimeter. On other hand, this is not a limiting factor for the Compton polarimeter because it is capable of running at the same current as the electron beam. At energies that CEBAF provides, the main uncertainties originate from the knowledge of the detectors' calibration and resolution in the determination of the mean analyzing power. One other important source of uncertainty is related to the asymmetry measurements of the Compton. In that regard, minimizing the sensitivity in beam position has to be taken care of carefully because of the fact that position of the beam is among the helicity-correlated beam parameters. The background depends on critically on the beam tune. The Møller polarimeter is insensitive to these kind of uncertainties. At the energy of DVCS experiments the total systematic error of the Compton measurement was 2%, and it was 3% for the Møller polarimeter[93].

### **Beam Position Monitors**

In the experimental Hall A, there are two Beam Position Monitors (BPMs) located 7.524m and 1.286m upstream of the target (Fig.22). The technique that is used to determine the relative position of the beam is to calculate the ratio of the difference to sum voltages of diametrically opposed wire pairs. By this technique the relative position can be determined within 100  $\mu m$  for currents above 1  $\mu A$ . In order to measure the absolute position of the beam, the BPMs needs to be calibrated. This process is done by wire scanners called harp which consists of thin wires that can be moved into the beam. Then, the absolute position is determined relative to the geometrical survey of the harp.

### **Beam Current Monitor**

Beam current is among the parameters which are necessarily to be monitored and/or measured during an experiment. To be able to maintain a stable, low-noise, non-invasive beam current monitoring and/or measurement the Beam Current Monitor (BCM) installed in to the experimental Hall A (Fig.22). The Hall A BCM components are, an Unser monitors, two RF cavities, associated electronics and a data-acquisition system. The Unser monitor is a Parametric Current Transformer which provides an absolute reference. The monitor is calibrated by passing a known current



through a wire inside the beam pipe. As the Unser monitor's output signal drifted significantly on a time scale of several minutes, it cannot be used to continuously monitor the beam current. The two RF cavity monitors are stainless steel cylindrical waveguides which are tuned to the frequency of the beam down-shifting and rectifying the output signal produced voltage levels are proportional to the beam current. The BCM monitors in Hall A are enclosed in a temperature-stabilized box to stabilize the gain and provides an absolute measurement of the beam current with accuracy of 0.5% [93].

### Absolute Energy Measurement

Beam energy at JLab can be measured with two independent methods, the ARC method and the eP method. The eP method utilizes a stand-alone device along the beamline located 17 m upstream of the target. In this method, the beam energy is determined by measuring the scattered electron angle  $\theta_e$  and the recoil proton angle  $\theta_p$  in the  $H(e, e'p)$  elastic reaction. This was not used during the DVCS experiments because of the fact that instrumentation was not operational at that time.

The ARC method measures the deflection of the beam in the arc section of the beamline. The measurement is made when the beam is tuned in dispersive mode in the arc section. In this method, the aim is to have dispersive arc so it that can function like a spectrometer and this can be achieved by turning off the correction quadra-poles. The correction dipoles along with the eight deviation dipoles, quadrupoles and sextupoles are located at the entrance of Hall A. Specific instrumentation for the ARC method includes a set of wires scanners, and an absolute angle measurement device, and an absolute field integral measurement device for the reference magnet.

The method consists of two simultaneous measurements, one for the magnetic field integral of the bending elements (the eight dipoles), based on a reference magnet (the ninth dipole) measurement, and the actual bend angle of the arc, based on the wire scanners.

A measurement of the beam energy performed during the DVCS experiment based on ARC method resulted in a beam energy of  $5757.1 \pm 0.1 \text{ MeV}$  [61].

### IV.2.3 The Target System

The experimental Hall A target system cooled down on September 29 1997 with a world record on beam power over 700 Watts and luminosity of  $5 \times 10^{38} \text{cm}^{-2} \cdot \text{scc}^{-1}$ . The target system in Hall A provides three different standard targets; the Waterfall target, the Cryogenic target and polarized  $He^3$  target. In 2004 DVCS experiments Cryogenic target system was used with a custom made scattering chamber.

#### The Target Scattering Chamber

The standard scattering chamber 2 inch thick aluminum walls and no windows for the recoil protons of DVCS. The minimum detected recoil proton momentum was about 305 MeV/c which corresponds to a range of 2.49 cm in aluminum. Therefore, a custom made scattering chamber was built for the DVCS experiments. The DVCS scattering chamber is made of a 1 cm spherical shell of aluminum, allowing for low energy protons to go through it. In addition to thickness, a larger exit beam pipe was constructed which reduces the background.

One other important contribution of the DVCS scattering chamber is that it accommodates the spherical symmetry of the reaction, making energy losses independent of the scattering angle [61].

#### Cryogenic Targets

The cryogenic target [90] system mounted inside the scattering chamber, operates with the following sub-systems:

- Cooling
- Gas handling
- Temperature and pressure monitoring
- Target control and motion
- Calibration
- Solid target ladder

The standard cryogenic target in Hall A has three independent target loops:

- Liquid Hydrogen ( $LH_2$ ) loop
- Liquid Deuterium ( $LD_2$ ) loop
- Gaseous Helium loop

Among these three loops, the two liquid loops were used in DVCS experiments. Each of the liquid loops has two aluminum cylindrical target cells mounted on the target ladder and the cells can be either 4 cm or 15 cm. The 15 cm long target cell was used in our experiment. These standard cells have the sidewalls of a thickness of 178  $\mu m$ , with the entrance and exit windows approximately 71 and 102  $\mu m$  thick respectively. The operating temperature and pressure of the

- $LH_2$  target are 19 K and 0.17 MPa, with a nominal density of 0.0723  $g/cm^3$ .
- $LD_2$  target are 22 K and 0.15 MPa, with a density of 0.167  $g/cm^3$ .

The targets are installed on to a vertical ladder which can move from one position to another by a remote control system. In addition to the loops, the target ladder contains the following target positions:

- Optics: Consists of seven layers of 1 mm carbon foils with purpose of optics calibration of HRS
- Dummy 15cm:  $\pm 7.5$  cm Aluminum foils to study the target wall effects.
- BeO: used in visualizing the beam spot at the target through a camera installed in scattering chamber.
- Carbon Hole : 1 mm thick Carbon, with a hole the diameter of the target cell.
- Cross Hair: Aluminum target used to measure the beam position with respect to target.
- Empty: It is empty in the sense that beam hits nothing on its path through the target ladder. The purpose of having an empty position is to be able to reduce the radiation while beam is used for other measurements such as Møller runs, beam size measurements using wire scanner

Although the Hall A target can take current up to 120-130  $\mu A$ , the DVCS experiment ran at a maximum current of 3  $\mu A$  with the instantaneous luminosity of

$$L = \frac{I}{e} L_{target} \cdot N \cdot \frac{\rho}{M_p} = \frac{2.5 \cdot 10^{-6}}{1.6 \cdot 10^{-19}} \cdot 6.02 \cdot 10^{23} \cdot 0.07229 \cdot 15 = 10^{37} cm^2 \cdot s^{-1}.$$

#### IV.2.4 Dedicated DVCS Detectors

The design of E00-110 experiment differs from the previous DVCS experiment in terms of the detector design. All previous experiments used large acceptance detectors which are limited in luminosity. In order to optimize the luminosity and acceptance, in this experiment a reasonable compromise achieved for the emitted photons' and recoil protons' acceptances. Based on the optimizations done by simulations, the design of the dedicated detectors completed.

Among the standard detectors in experimental Hall A, L-HRS was used for scattered electron momentum measurements. The hadron spectrometer (R-HRS) can not be used because of the fact that the recoil protons are highly out-of-plane. For the detection of emitted photon and the recoil proton in DVCS reaction two dedicated detectors were built. Here I describe the Electromagnetic Calorimeter and Proton Array.

##### Electromagnetic Calorimeter

The central part of the DVCS is the electromagnetic calorimeter, therefore its major limiting factor, resolution, becomes the main issue of the DVCS. In addition to resolution some other requirements needed to met for the experiment:

- Compactness: To be able to achieve the maximum acceptance with in the kinematical constraint that the photons must be detected at angles as small as  $10^\circ$  up to  $14.8^\circ$ , with luminosity of at least  $10^{37}$ , the calorimeter has to be located as close as possible to target. Moreover, presence of the proton array requires a compact calorimeter as well.
- Radiation hardness: Being close to the target, means also being close to beamline which caused the exposure of a high flux of Møller electrons. Radiation resistant is a must for the calorimeter in DVCS experiment.
- Sensitivity to background: At that distance from target and beamline, one other important issue is electromagnetic and hadronic low energy background.
- Mechanical simplicity: The geometry and location of the dedicated detectors requires to have simple and easy mechanical motion. In order to achieve

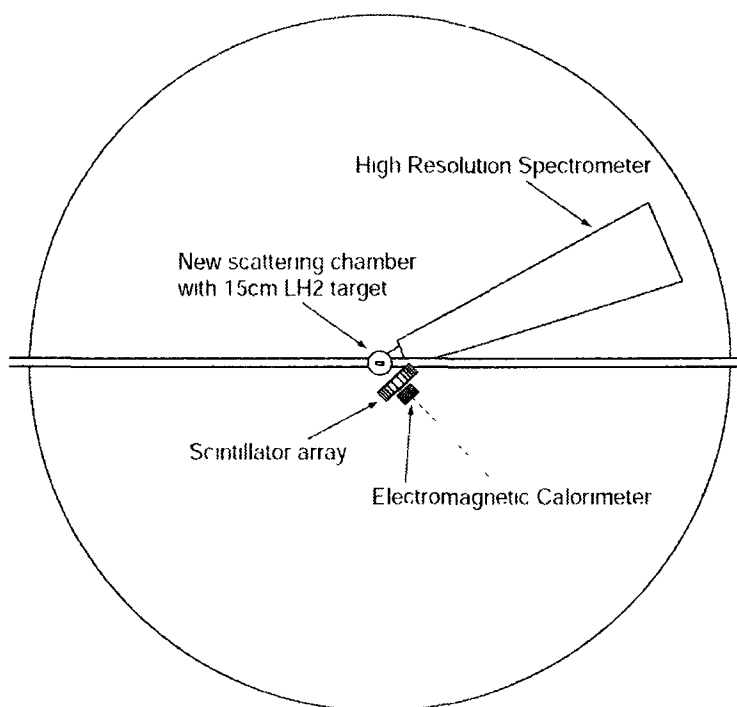


FIG. 25: Top view of Experimental Hall A, showing the location of the scintillator array (proton array), the electromagnetic calorimeter, L-HRS, and scattering chamber. The R-HRS is not shown, and it is parked at a large angle. The support frame for both detectors is not shown.

In order to meet the first three requirements,  $PbF_2$  blocks were used in the electromagnetic calorimeter [94].  $PbF_2$  is an attractive Čerenkov medium for electromagnetic calorimetry. The primary characteristic of  $PbF_2$  is its very high density ( $7.77 \text{ g/cm}^3$ ) which allows a very compact calorimeter. As a pure Čerenkov radiator, in  $PbF_2$  instant Čerenkov radiation is observed and the immediate consequences of this are:

- Good energy resolution
- Easier pulse separation in case of pile-up (shown in Fig. 33).
- Good compatibility with dedicated DVCS electronics.

The calorimeter was built as an array of  $11 \times 12$  and each  $PbF_2$  block has a transverse dimension of  $3 \text{ cm} \times 3 \text{ cm}$  and a longitudinal dimension of  $18.6 \text{ cm}$ . The 132 calorimeter blocks covers an overall transverse area of  $33 \text{ cm} \times 36$  provides an acceptance of  $t_{min} - t < 0.3 \text{ GeV}^2$ .

Each calorimeter block covered by Tyvek and Tedlar, inner and outer covers respectively. The Čerenkov photons (estimated by Monte Carlo simulation) emitted in each block by charged particles of the electromagnetic shower are collected by Hamamatsu R7700 PMTs. The PMTs and the blocks are held together with a system composed of cubic carved copper piece which receives the PMT and a front hole plate linked together with two brass foils. The Čerenkov yield was 1000 photoelectrons/GeV.

DVCS calorimeter is also equipped with a gain monitoring system which functions based on Light Emitting Diodes (LEDs). The LED monitoring was done on a daily basis during the experiment in order monitor the radiation damage that can be caused by the background of low energy radiation. This monitoring system system needs to be placed in front of the calorimeter crystal which arose as an issue in the mechanical support design because of the fact that the detectors are located as close as possible to the target. In order to move the LEDs in front of the calorimeter a XY-table was used. The calorimeter moved back for about  $45 \text{ cm}$  so that LEDs carrying XY-table can be placed in required position. The XY-table and sliding system along the with layout of the calorimeter can be seen in Fig.26.

The LED system was used to simulate the low energy background noise in the PMTs and check the gain variation of them as function of their anode current.

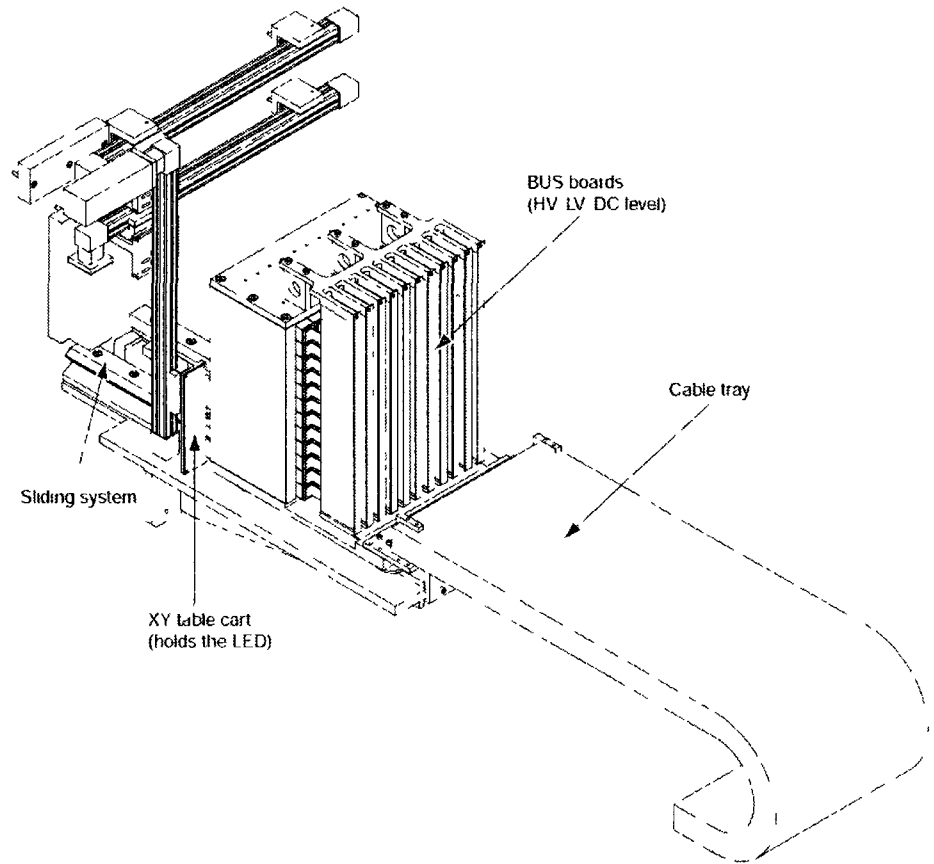


FIG. 26: Backside view of Calorimeter layout, showing the XY table, which functions as LED carrier, the mechanical system to control the motion of LED system and the cable tray

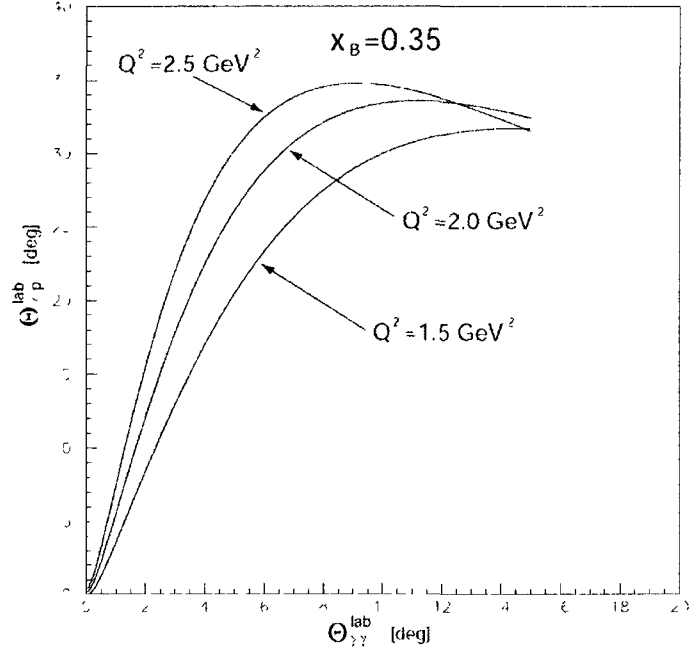


FIG. 27: Correlation between  $\theta_{\gamma\gamma^*}$  and  $\theta_{\gamma^*p}$  is shown for the  $Q^2$  values of  $2.5 \text{ GeV}^2$ ,  $2.0 \text{ GeV}^2$ ,  $1.5 \text{ GeV}^2$  for  $x_B = 0.35$ .  $\theta_{\gamma\gamma^*}$  is the angle between emitted photon and the virtual photon  $\theta_{\gamma^*p}$  is the angle between the virtual photon and the recoil proton. The experimental acceptance for  $\theta_{\gamma^*p}$  the can be seen in Fig. 28

### Proton Array

In order to detect the recoil protons in deeply virtual kinematics of E00-110 experiment, a 100 element plastic scintillator array (proton array) was constructed. As mentioned at the beginning of this chapter, hadron spectrometer can not be used because of the highly out-of-plane recoil protons. Because of the same reason the design of the proton array is matched to the out-of-plane acceptance which is also required to measure beam helicity asymmetry in DVCS kinematics.

The proton array covers a polar angle range of  $18^\circ < \theta_{\gamma^*p} < 38^\circ$  (corresponds  $1^\circ < \theta_{\gamma\gamma^*} < 10^\circ$ ) in five rings around the central  $\vec{q}$  direction. The minimum polar angle must be  $18^\circ$  because of the fact that, for smaller angles than 18 degrees, proton array can interfere with calorimeter. On the other hand, the maximum limit choice of  $38^\circ$  originates from the fact that larger  $-t$  values the proton actually moves to smaller angles Fig. (28). Each ring is divided into 20 elements that together subtend



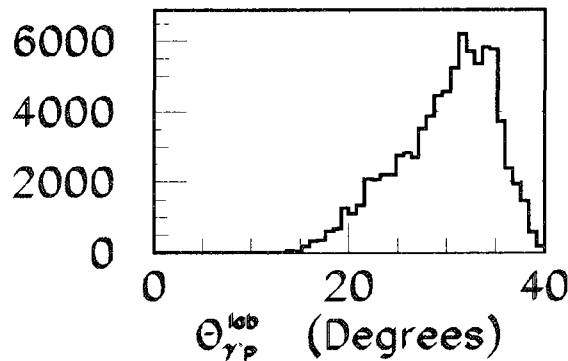


FIG. 28: The Experimental Acceptance for Proton Array and  $\theta_{\gamma^*p}^{lab}$  is the angle between virtual photon and recoil proton in lab frame

the azimuthal angles from 45 to 315 degrees. The azimuthal segmentation of the proton array allows one to correlated the proton array element with the prediction direction of the recoil proton (prediction based on the electron and emitted photon measurements). The azimuthal cut-off on the beam side between azimuthal angles -45 to 45 degrees is required to make fit the beam exit pipe in the compact design of custom scattering chamber, calorimeter and proton array [95].

The proton array is located around the direction of the virtual photon and as close as to target to minimize the consequences of multi-scattering on the target chamber. Nevertheless, this compact structure brings low energy backgrounds which originates from Møller electrons and low energy photons. This backgrounds can cause serious damages to the detectors, thus plastic scintillators shielded with 2 cm Aluminum and the PMTs' gain monitored continuously by DC current monitors .

Because of the scintillators, the proton array is very sensitive to above mentioned low energy background which can cause damages to PMTs. The electronic equipments in detector are not sensitive to DC current which could cause the damage. Therefore, the proton array includes a DC current monitoring system which consists of a simple circuit with 10  $K\Omega$  resistor that current from the anode pass through it so that the read-out voltage can be recorded. All the read-outs sent into the scanning ADCs

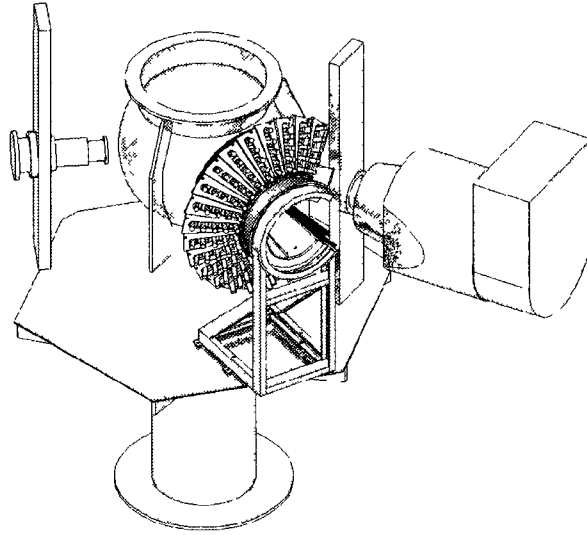


FIG. 29: Proton Array with Scattering Chamber. Relative position of the proton array to the scattering chamber and the L-HRS. The exit beam pipe, not shown here, is in between PA and L-HRS.

and provided a real-time read-out by Experimental Physics and Industrial Control System (EPICS). Through, this system the detector were checked at least once a shift to ensure PMTs were working properly.

### DVCS Mechanical Support

Calorimeter and proton array were mounted to each other by an Aluminum plate centering the calorimeter in the center of proton array, in other words the direction of the virtual photon is toward to the center of calorimeter. Reasonable compactness achieved by the design of the detectors, however, we aim to cover the maximum solid angle by the calorimeter and to make this coverage achievable, the calorimeter had to be as close as possible to the scattering chamber. This arose the issue of not having enough place for the LEDs monitoring system which is a monitoring system. Moreover, in order to perform the calibration of the calorimeter by using elastics events, calorimeter needs to move back to 5.5 m. Therefore, to be able to move the calorimeter as it is necessary, the detectors placed on to the stand designed for Big Bite standard spectrometer of Hall A (shown Fig. 32). This stands allows not only

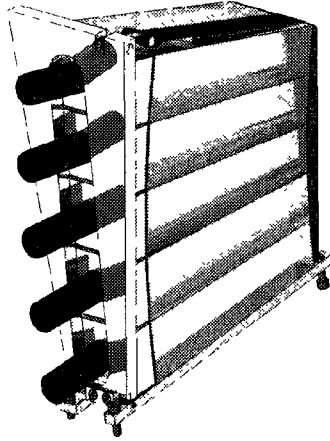


FIG. 30: Proton array consists of 20 towers and each towers is combination of 5 scintillator blocks and PMTs at the end. Here single PA tower is shown. Each tower covers  $13.5^\circ$  in azimuthal angle ( $\phi$ ) and each scintillator block covers  $4^\circ$  in polar angle ( $\theta$ ).

back and forth motion but also allows the circular motion of the DVCS detectors which provide accurate positioning based on the required kinematics.

#### IV.2.5 Data Acquisition

DVCS experiments in Hall A, requires to have dedicated data acquisition system in addition to the dedicated detectors. DVCS experiments' specific requirements such as  $e\gamma$  coincidence trigger, read-out, background and counting rates can not be met by solely using the standard Hall A data acquisition system. Here I will describe the standard Hall A DAQ, DVCS DAQ and associated electronics, and the modifications done in standard Hall A DAQ.

#### Standard Data Acquisition System in Experimental Hall A

At Jefferson Laboratory, DAQ group designed and maintains CEBAF On-line Data Acquisition (CODA) software in order to provide data acquisition for three existing experimental Halls. CODA supports main commercially available hardware elements,

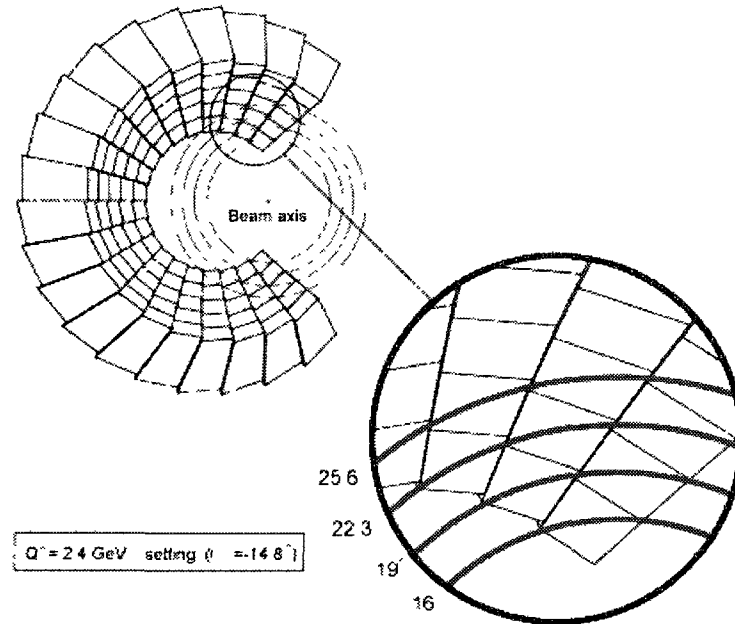


FIG. 31: The compact design that can be seen in Fig. 29 ensues the condition of being in direct view of target, and being exposed to the radiation effect from the beamline. As it can be seen here, radiation effects can highly be observed in first 3 or 4 towers from each end of the PA. Although the radiation doesn't effect the all 5 blocks, it is major issue for the closest towers. One immediate consequences of beam pipe radiation in this triple coincidence analysis is that we removed the two towers in both ends of the PA (will be explained in the coming chapters). In this analysis, a new calibration of the calorimeter performed and it is shown that the beam pipe radiation effects are not negligible for the calorimeter blocks closer to the beam pipe.

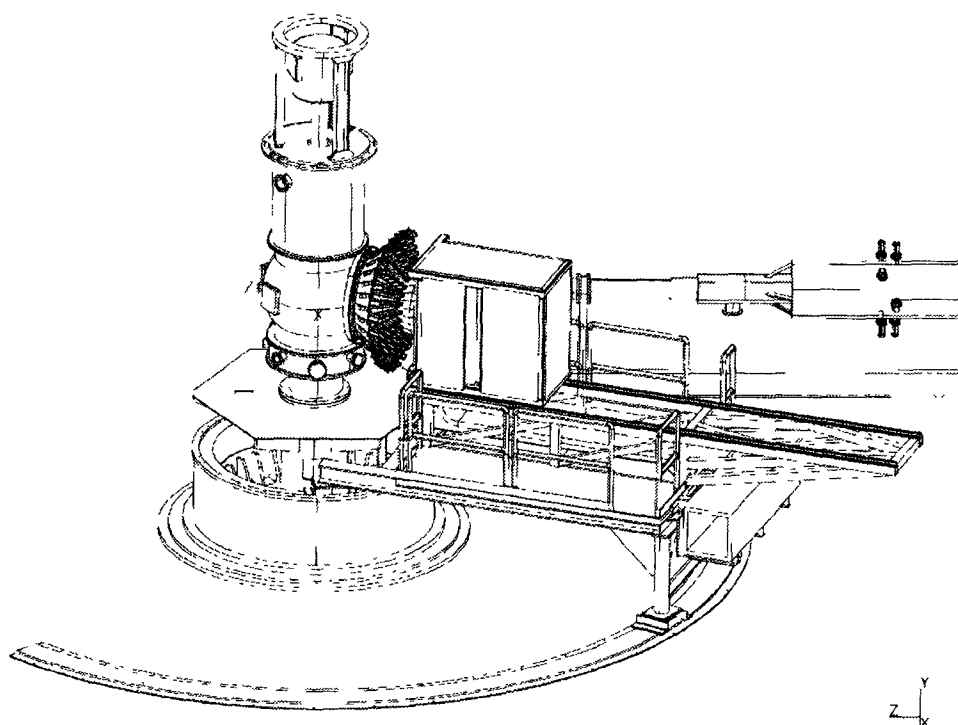


FIG. 32: The Schematic view of the scattering chamber, proton array, calorimeter, Big Bite stand along with beam line. The Big Bite stand which was used for as DVCS stand allowed the circular motion of the DVCS detectors with precise adjustment of the desired kinematical angles.

electronics including front-end Fastbus, VME digitization devices, the Struck Fastbus Interface, single-board VME computers, 100 BaseT Ethernet networks, Unix or Linux work stations, and a mass storage tape silo for long-term data storage. The commercial software elements are the VxWorks operating system which runs on the VME computers, and either SunOS Linux on the work stations. Custom hardware elements made at JLab include the trigger supervisor which synchronizes the read-out of the front-end crates and handles the dead-time. The most important custom software components of CODA are the read-out controller (ROC) which runs on the front-end crates, the event builder (EB) and event recorder (ER) which run on a Unix or Linux workstation, the event transfer (ET) system which allows distributed access to the data on-line or insertion of the data from user processes, and finally Run-Control process, which users can select different experimental configurations [96, 97], and control the data acquisition.

### DVCS DAQ

The DVCS experimental set up had very compact design as it can be seen in Fig. 29 and 32. Moreover, the large acceptance DVCS detectors are in close vicinity to the target (e.g. for one of the kinematics, some calorimeter blocks positioned at  $6^\circ$  and 110 cm from the scattering chamber) and at small angles from the beamline. The distance between the beamline and detectors can be seen in Fig. 31 and beamline effects to the proton array can be seen. In addition to these, DVCS experiment ran at very high luminosity ( $10^{37} \text{ s}^{-1} \text{ cm}^{-2}$ ) so it was expected to observe high single rates, up to 10 MHz [61] and high background which is not an issue for standard Hall A detector electronics because usually in Hall A, small acceptance detectors are used. Including the pile-up events (as in Fig. 33), standard ADCs could not provide accurate data acquisition. Therefore, dedicated Analog Ring Sample (ARS) [94] designed to be able to acquire accurate data acquisition (e.g. energy and position resolutions)

**The ARS** is the custom electronics used in DVCS experiments instead of the standard ADCs. ARS is a sampling system consists of an array of 128 capacitor cells. ARS allows sampling at 1 GHz rate up to 128 ns which allows to record the signal coming from each PMT for every event and to function like a digital oscilloscope and to perform off-line waveform analysis for the pile-up events (typical

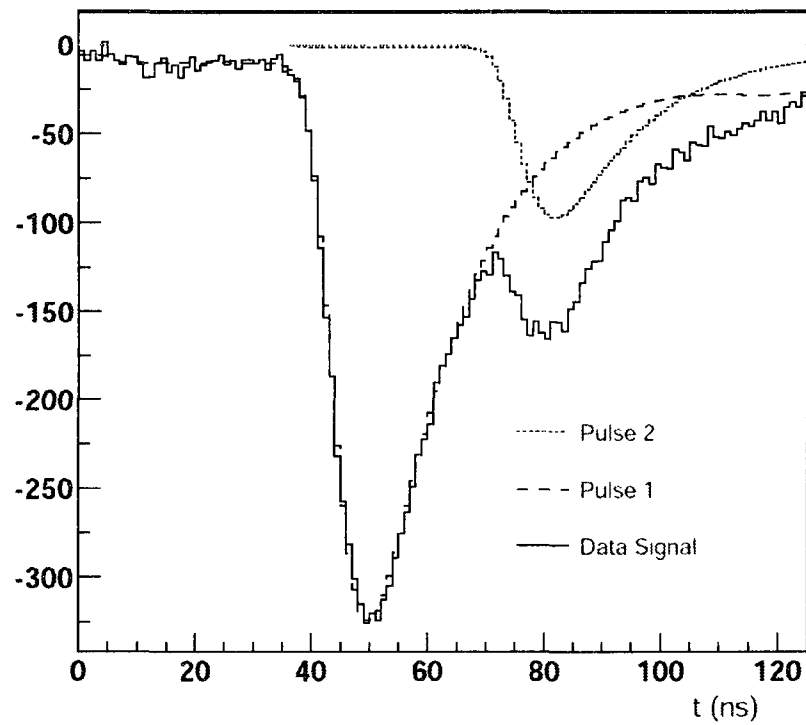


FIG. 33: Typical waveform recorded by an ARS channel, yielding two pulses. A waveform analysis is performed to get the information about the two separate pulses.

pile-up event shown in Fig.33). The fixed sampling frequency of 1 GHz is defined by the delay between two consecutive good signals, however, the front-end electronics has a band-width of  $\sim 300$  MHz.

The ARS system allows to have data transfer rate of 2 MBytes/sec which generates huge amount of data. Initially it may seem to good to have that amount of data, nevertheless, it entails an impact on the data acquisition dead-time. In order to reduce the amount of recorded data and to accommodate the intriguing channels of the calorimeter a dedicated DVCS trigger module was designed.

**DVCS trigger** is the custom trigger used in DVCS experiment. The existing L-HRS single trigger forms the bases of this trigger with addition of calorimeter coincidence custom feature. In addition to the background, another major issue for DVCS calorimeter is the electromagnetic shower in the detector. Typically, 9 blocks are being hit, and more than 90 % of the energy is deposited in the central block. As a solution, a high threshold can be set, however, as can be seen Fig. 34 the level of issue varies according to location of the block. Moreover, and individual block threshold can not be exact remedy based on the requirements of the experiment.

The most maintainable remedy developed through the custom trigger module which scheme briefly can be seen in Fig. 35.

- The initial step is the signal generated by standard L-HRS trigger module by the detection of a good electron. This signal is a coincidence between S1 and S2m. This is called T3 trigger.
- Second step is the coincidence between the Čerenkov detector and S2m. This signal triggers the system to integrate the signal of each calorimeter PMT in a time window around 60 ns. 7-bit flash-ADCs are used to integrate each individual channel. Using the Čerenkov detector allows to filter pion events by a prescale on this trigger. If the pion events were needed, prescale factor changed accordingly.
- Then sum of these integrated ADC values are computed for every set of  $2 \times 2$ . 4 adjacent blocks, which is called calorimeter tower.. (shown in Fig. 36). The sum of these 4 adjacent are computed over 8-bit. Among these towers, only the ones higher than the set threshold are recorded.



- The recorded values for a random good event can be seen in Fig. 37. The numbers shown in each calorimeter block, correspond to integration over 7-bit of the individual channels. As it can be seen in Fig. 37 most of the blocks have ADC values of 8 or 9 which correspond pedestal. All over the calorimeter there can be seen ADCs channels between 10 - 13, because of the low energy noise. In this particular event, there exist only 4 overlapping towers are higher than the threshold number of ADC channels. In addition the ARS corresponding to the highest energy block and the 8 adjacent blocks' signal are recorded even though the low energy signals are not recorded.

This procedure takes about 340 ns, after this, there are two possible outcomes as can be seen in Fig. 35:

- No coincidence case, there exist no tower with higher energy than threshold, therefore the fast clear of all ARS is processed with a total dead time of 500 ns.
- Coincidence case, is the case where there exist at least one tower over threshold and the photon trigger receives the coincidence signal from the calorimeter trigger. Then, the photon trigger sends  $e\gamma$  coincidence signal (T5) which is the validation signal for trigger supervisor.
- The final step is to record the ARS, and this process is operated by trigger supervisor. Simply, if T5 delivers the validation signal, then ARS is recorded for the  $e\gamma$  coincidence. Following the recording, the ARS fast clear starts in order to have the DAQ ready for the next event. For the coincidence case, the processing and transferring the data imply a dead time about 128  $\mu s$ .

The challenging detector, proton array, is not in trigger module, however, the read out of the proton array performed for every single  $e\gamma$  coincidence. Therefore, the challenge for DAQ is how to perform proton array data acquisition, the triple coincidence ( $e\gamma p$ ) case, without increasing the dead time and of course the amount of the recorded data. As a matter of fact, the remedy is the answer to the question of: "is it necessary to read out all the blocks of the PA for  $e\gamma$  coincidence ? "

Because of the DVCS kinematics (Fig. 10) and the small acceptance of L-HRS the re-coil proton and the photon are in always in the opposite sides of the virtual photon and its the direction is always in a very small angular and it is constrained

to the four central blocks. Since the direction of the virtual photon constrained with the HRS acceptance in a fix direction, the only way to deduce where the proton would in the proton array, for a  $e\gamma$  coincidence, is to predict possible region in the proton array by using the position of photon in the calorimeter. The accuracy of this prediction is convoluted by HRS acceptance and the calorimeter energy resolution, in other words, what ever effects these two parameters, it effects the accuracy of the prediction. The prediction is computed by by a Monte-Carlo simulation which introduces the real physical effects of the experimental setup [95] (e.g. the resolution effects of the detectors). The Fig. 38 presents the proton array correspondence for calorimeter towers ( $2\times 2$ ).

Based on the projected predictions in Fig. 38 it is not necessary to read all the proton array blocks for each single  $e\gamma$  coincidence and immediate consequences:

- This eliminates the possible increase in the acquisition dead time and the amount of data.
- There is *no* need to set threshold for any proton array block so that even very low energy protons can be detected.

A multiplexer module is used to establish the communication between the calorimeter trigger module and proton array crate.

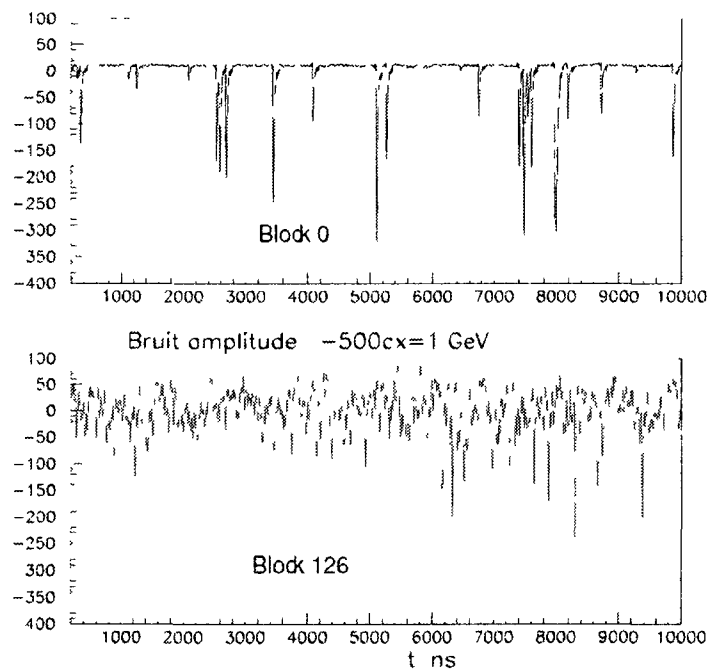


FIG. 34: AC coupled signal in different blocks. Depending on the position of the block, the behavior of signal varies as can be seen in this example. The block zero is in the far edge of the calorimeter from the beamline. On the other hand the block 126 is in the closest column to the beamline.

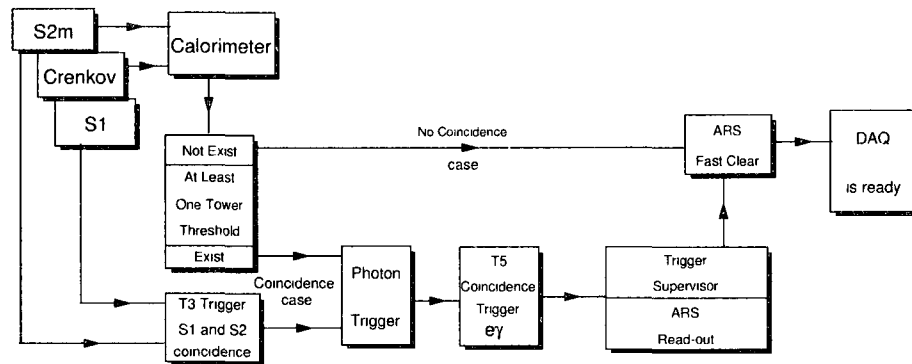


FIG. 35: Basic schema of the DVCS trigger module [98]. The HRS trigger is generated by the coincidence between S1 and S2m and the signal to trigger the calorimeter ADC integration is generated based on the coincidence between Čerenkov and S2m. Since both coincidences include the s2m, both cases have the same time reference. Here is the S2m is an upgraded version of the standard S2. S2m provides improved timing resolution. The significant feature of this custom trigger module is the coincidence trigger between the HRS trigger and the Calorimeter Trigger. In the case of no coincidence, none of the ARS channel needs to be read, it takes about 500 ns to get the DAQ ready for the new event. When the ARS is read out, DAQ will be busy for about 128  $\mu$ s.

11	23	35	47	59	71	83	95	107	119	131
10	22	34	46	58	70	82	94	106	118	130
9	21	33	45	57	69	81	93	105	117	129
8	20	32	44	56	68	80	92	104	116	128
7	19	31	43	55	67	79	91	103	115	127
6	18	30	42	54	66	78	90	102	114	126
5	17	29	41	53	65	77	89	101	113	125
4	16	28	40	52	64	76	88	100	112	124
3	15	27	39	51	63	75	87	99	111	123
2	14	26	38	50	62	74	86	98	110	122
1	13	25	37	49	61	73	85	97	109	121
0	12	24	36	48	60	72	84	96	108	120

FIG. 36: Calorimeter block numbers and an example of two overlapping 4 blocks clusters. After the digitization of each individual calorimeter block by using a 7 bit Fast ADC, the pedestals are subtracted. Then, all the sums of the 4 adjacent blocks are computed.

9	9	8	10	9	10	8	9	9	8	10
11	10	11	11	9	12	11	9	9	8	9
9	9	9	9	9	8	8	8	9	6	9
9	9	10	9	8	9	7	8	9	10	9
9	9	9	10	9	10	8	8	9	17	8
9	9	9	9	9	9	8	9	9	4	12
9	9	9	9	9	10	11	8	8	7	10
9	10	9	15	9	9	12	9	41	15	5
9	9	9	9	10	9	9	7	14	12	10
9	9	9	8	9	10	8	10	10	8	12
9	10	10	9	9	9	9	8	7	9	9
9	9	9	9	9	9	10	7	9	8	8

FIG. 37: The digitized ADC values in each 4 adjacent block set are computed and to a threshold. During the experiment, substantial amount of data were taken with a threshold of 57 ADC channels which corresponds to an energy value of 1 GeV ARSs with energy higher than threshold area recorded. A typical result of computed ADC channels is shown here in the solid line box where each 9 blocks in the box shows the result of ADC integration. Here in this event 4 overlapping 4 adjacent blocks formed a calorimeter tower, having the block in the center with an ADC value of 41. As it can be seen in this event, no individual block has a higher ADC value than threshold, and this is typical example of showering. In this case of having individual threshold for each block, the accurate information for deposited energy, for instance, from the photon of this particular  $e\gamma$  might be garbage.

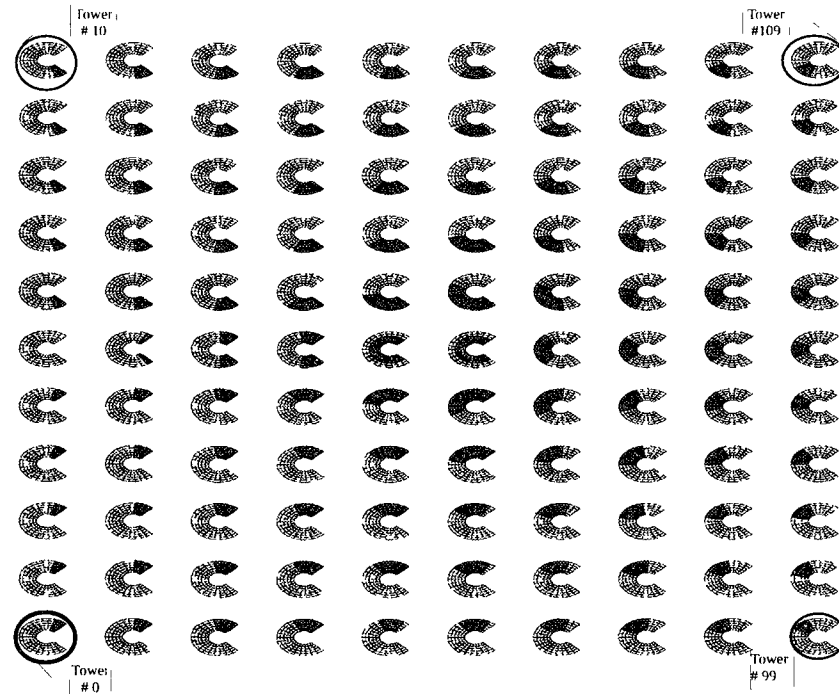


FIG. 38: Proton Array Blocks Projected to Calorimeter Towers The back view of the calorimeter towers and the proton array, the beam is on the right hand side. There are 132 blocks in the calorimeter, however, the number of towers is 110. Left edge bottom corner tower is tower number 0, and the right edge upper corner tower is tower number 109. The symmetric direction of the emitted photon and the recoil proton with respect to the virtual photon can be seen here. For example, while the tower is the left bottom corner, the predicted position where proton would hit is right upper corner of the proton array. Because of the geometry of proton array the projected proton array events in the blocks located on the left hand side are very few.

## CHAPTER V

### DVCS MONTE CARLO SIMULATION

The DVCS Monte Carlo Simulation is used for experimental acceptance calculation except the proton array's geometrical acceptance. We do not have a determination of proton array efficiency which prevents cross section extraction from proton array ,triple coincidence ( $H(e, e'\gamma p)$ ), data. However, any analysis with triple coincidence data requires the simulation of the experiment because of the fact that the proton prediction which is based on the DVCS Monte Carlo, is the core of the triple coincidence data analysis. Having said that, this chapter includes an overview of the DVCS simulation, and brief discussion about event generation. (Details can be found in [61].)

#### V.1 OVERVIEW OF THE DVCS SIMULATION

As discussed in chapter VII.2.3, there are three detectors in E00-110 experiment among which include the standard HRS of Hall A which is not fully simulated in this Monte Carlo Simulation. The HRS is well characterized and has been used in many experiment including the VCS experiment [103]. As a result of this, the acceptance, the angular resolution, and the momentum resolution of HRS have been measured accurately. Moreover, the parametrization and the acceptance function of HRS can be found along with other details about HRS in [104].

The implementation of the simulation can be summarized as;

- DVCS events are generated by sampling  $Q^2$ ,  $x_B$ ,  $t$ ,  $\phi$ , and  $\varphi$  (= scattered electron azimuthal angle).
- The initial step is to generate the events at the vertex in according to DVCS reaction kinematics.
- The scattered electron is simulated up to the front face of the HRS so that external radiative corrections can be implemented to the generated vertex events along with a multiple scattering;
- Emitted DVCS photon and the recoil proton are fully simulated along with multiple scattering in the air between the scattering chamber and the detectors;



- All main electromagnetic and hadronic process are simulated according to GEANT [105];
- Well defined QED radiative corrections [107, 108, 109, 110] are implemented:
  - In the processes where BH term is not negligible, radiative corrections have significant importance in extracting nucleon structure from  $ep \rightarrow ep\gamma$  reaction;
  - Radiative corrections can contribute to cross section in the order of 20% [74, 106];
  - Radiative corrections to the leptonic side (BH) are dominant ones. Due to larger mass of proton, radiative corrections from proton side are suppressed.
  - Radiation of an additional photon cause a radiative tail in missing mass which is included in the simulation as well.
- An electron passing through a slice of material loses energy via ionization of the medium. This is known as straggling and along with the radiative energy loss (bremsstrahlung) it is used to generate initial electron energy at the reaction vertex.

## V.2 GENERATION OF SCATTERED ELECTRON EVENTS

The full space event generation is redundant for HRS because of the fact that a very limited number of these events would be detected due to the small acceptance for electrons in this experimental setup. The initial event is generated within the horizontal plane with angular limits slightly larger than the real HRS limits in order to be able to use precise acceptance function. For a given value of the initial electron energy, the electron kinematics of the event is defined by choosing  $Q^2$  and  $x_B$  randomly and uniformly within the required ranges [61].

## V.3 GENERATION OF HADRONIC REACTION EVENTS

The hadronic part of the electroproduction of photons,  $\gamma^*p \rightarrow \gamma p'$  is first computed in center of mass frame and the generated particles are boosted to the laboratory

frame. The variables  $t$  and  $\varphi = [0, 2\pi]$  are generated randomly. As a result of the kinematical limit defined by Eq. (65),  $t < 0$  is in the interval of

$$t \in [t_{min}, t_{max}(x_B, Q^2)]. \quad (70)$$

where

$$t_{min} \approx \frac{-M^2 x_B^2}{1 - x_B}$$

and  $t_{max}$  is chosen small enough (typically  $-1.0 \text{ GeV}^2$ ) so that it does not affect the acceptance. Each hadronic reaction event is weighted with a phase space weight factor of  $(t_{max} - t_{min}) \cdot 2\pi$ .

As a final step in simulation, the scattered electron, real photon and recoil proton are rotated around the beam axis, to simulate the vertical acceptance of HRS. This rotation is larger than the actual vertical acceptance of HRS so that a final phase space factor  $\Delta\varphi$  is applied. The global phase space weight associated by this event is

$$\Delta\Gamma = \Delta x_B \Delta Q^2 \Delta\varphi \Delta\phi \Delta t(x_B, Q^2), \quad (71)$$

which is constant for each event, except for the value of  $\Delta t = t_{min} - t_{max}$ .

The electromagnetic shower in the calorimeter is fully simulated (GEANT simulation), following each particle down to an energy threshold of 100 keV. In the triple coincidence data analysis, additional block by block smearing is applied to calorimeter events which will be discussed in chapter VII.

## CHAPTER VI

### HRS AND CALORIMETER WAVEFORM ANALYSIS

The triple coincidence analysis is based on the proton array data. However, the analysis method is convoluted with the other two detectors, L-HRS and electromagnetic calorimeter, information as well. This requires the development of a comprehensive approach to the analysis method of the DVCS experiment. Here in this chapter, I will discuss the analysis method for; the standard Hall A L-HRS, electromagnetic calorimeter and the proton array.

#### VI.1 HALL A HRS DATA ANALYSIS

The Hall A physics data analysis model is straightforward and can be classified in to two parts;

- VDC analysis: tracking and reconstruction,
- optics reconstruction of the interaction vertex from the coordinates of the detected particles at the focal plane.

The details of the HRS and detector packages are discussed in IV.2.1. Here in this section I will discuss the HRS's analysis model which is in fact a crucial part of the inclusive experiments for the particle identification. On the other hand, in an exclusive experiment, like DVCS, the detection of the recoil particle, e.g. proton, verifies the DVCS event in HRS.

##### VI.1.1 VDC analysis: Tracking and Reconstruction

The tracking information is obtained from the two Vertical Drift Chambers (VDCs) in each spectrometer. A charged particle along its way, ionizes the gas in the chamber. As a result, ions and electrons are generated in this process. As the electrons drift toward the anode wires, the field intensifies the drifting. As consequence, electrons accelerate and cause further ionizations resulting in an avalanche which induces an electrical signal on the wire. The induced signals are pre-amplified and sent to Time to Digital Converters (TDCs).

The TDCs are capable of recording recording multiple hits (electrical signals) per event. In the case having multiple hits, the first hit corresponds to the largest TDC

value. Only the first hits are used in the analysis and the all subsequent hits are ignored because of the fact that multiple hits are often associated with electronic ringing or track-induced noise. After selecting the hits, clusters are identified. Clusters consist of hits with consecutive wire numbers. Moreover, to allow inefficiencies, clusters are allowed to have gaps of one wire with out a hit. Typically, in a cluster there exist four to six hits.

In principle, tracks can be reconstructed using only the cluster center coordinates; however, the spatial resolution per plane does not meet the HRS requirements. On the other hand, better resolution can be obtained by the TDC timing information. The TDCs measures directly the time between ionization and the arrival of the signal at the wire which is called as “drift time”. The extraction of precise drift distances from the measured drift times requires a detailed analysis as a result of the fact that the relationship between drift time and absolute drift distance is non-linear because of the non-uniform electric field within the cells. The dependence of distance on time can be parametrized either analytically based on calculations or empirically based on data [96, 97].

The track through the VDC is reconstructed from the cluster and timing information. Based on the number of clusters different algorithms are implemented. For example, in the case of having on cluster per wire plane, a standard linear fit is performed on each cluster in each wire plane. This linear fit allows an accurate determination of the cross-over point of the track in the wire plane. If multiple clusters occur in any plane an algorithm, to reconstruct the tracks, is implemented which identifies all possible combinations of clusters from four VDC planes, and each combination is considered a possible path of track through chambers. Then, a fit is performed and the path having the smallest  $\chi^2$  corresponds to the best reconstructed track. Nevertheless, the whole multi-track events are discarded in our analysis, and an efficiency correction is applied.

### VI.1.2 Optics Design, Momentum and Vertex reconstruction

In the standard Transport formalism [98] the trajectory of a charged particle through a system of magnetic elements is represented by a vector

$$\vec{x} = \begin{bmatrix} x \\ \theta \\ y \\ \phi \\ l \\ \delta \end{bmatrix} \quad (72)$$

where  $x$  is the displacement of the trajectory relative to the reference trajectory in the bend plane (for HRS the  $x - z$  plane is the vertical plane),  $\theta$  is the tangent of the angle with respect to the reference trajectory,  $y$  and  $\phi$  are equivalent to  $x$  and  $\theta$  in the transverse plane,  $l$  is the path length difference between the trajectory and reference trajectory, and  $\delta = (\Delta p/p)$  is the fractional deviation of the momentum of the trajectory from the central trajectory. The orientation of the Cartesian coordinates are such that  $\hat{z} = \hat{x} \times \hat{y}$ . The location and direction of the trajectories are recorded at each of the critical apertures along the spectrometers. The critical apertures are those that have been identified as defining the acceptance.

For each event, two angular coordinates ( $\theta_{det}$  and  $\phi_{det}$ ) and two spatial coordinates ( $x_{det}$  and  $y_{det}$ ) are measured at the focal plane detectors. The position of the particle and the tangent of the angle made by its trajectory along the dispersive direction are given by  $x_{det}$  and  $\theta_{det}$ , while  $y_{det}$  and  $\phi_{det}$  give the the position and tangent of the angle perpendicular to the dispersive direction. These focal plane variables are corrected for any detector offsets from the ideal central ray of the spectrometer to obtain the focal plane coordinates  $x_{fp}$ ,  $\theta_{fp}$ ,  $y_{fp}$ , and  $\phi_{fp}$  [99]. To first order, the optical transport from the target to the local plane is described by the matrix:

$$\begin{bmatrix} x_{fp} \\ \theta_{fp} \\ y_{fp} \\ \phi_{fp} \\ \delta_{fp} \end{bmatrix} = \begin{bmatrix} -2.48 & 0.00 & 0.00 & 0.00 & 12.4 \\ -0.15 & -0.40 & 0.00 & 0.00 & 2.04 \\ 0.00 & 0.00 & -0.40 & -1.30 & 0.00 \\ 0.00 & 0.00 & 0.54 & -0.78 & 0.00 \\ 0.00 & 0.00 & 0.00 & 0.00 & 1.00 \end{bmatrix} \cdot \begin{bmatrix} x_{tg} \\ \theta_{tg} \\ y_{tg} \\ \phi_{tg} \\ \delta_{tg} \end{bmatrix} \quad (73)$$

Notice that the transverse matrix is neither point to point,  $\langle y_{fp} | \phi_{tg} \rangle = 0$ , nor parallel to point,  $\langle y_{fp} | y_{tg} \rangle = 0$ . This compromise was driven by the need for a simultaneous good resolution in the transverse position,  $y_{tg}$  and angle,  $\phi_{tg}$ .

Since we do not measure  $\delta_{fp}$  a full inversion of (73) requires apriori knowledge of  $x_{tg}$  from the beam position monitor (BPM). In practice, the expansion of the target

coordinates is performed up to fifth order. A set of tensors  $Y_{jkl}$ ,  $T_{jkl}$ ,  $P_{jkl}$  and  $D_{jkl}$  links the focal-plane coordinates to the target coordinates according to

$$y_{tg} = \sum_{j,k,l} Y_{jkl} \theta_{fp}^j y_{fp}^k \phi_{fp}^l, \quad (74)$$

$$\theta_{tg} = \sum_{j,k,l} T_{jkl} \theta_{fp}^j y_{fp}^k \phi_{fp}^l, \quad (75)$$

$$\phi_{tg} = \sum_{j,k,l} P_{jkl} \theta_{fp}^j y_{fp}^k \phi_{fp}^l, \quad (76)$$

$$\delta = \sum_{j,k,l} D_{jkl} \theta_{fp}^j y_{fp}^k \phi_{fp}^l \quad (77)$$

where the tensors  $Y_{jkl}$ ,  $T_{jkl}$ ,  $P_{jkl}$  and  $D_{jkl}$  are polynomials such as

$$Y_{jkl} = \sum_i C_i x_{fp}^i, \quad (78)$$

where subscript  $i$  and superscript  $i$  denotes the elements of the matrix in (73).

### The extended target correction

The HRS angular acceptance is a complex function of momentum and vertex position, within the extended target such as the one used in DVCS. Using extended target prevents simultaneous determination of the particle momentum and the interaction point at the target. Solution of this issue is to assume that HRS is formed by small-acceptance pointing-type spectrometer. It is assumed that the spectrometer reconstruct the position at the target transverse to the bend plane ( $y_{tg}$ ) with relative high precision,  $x_{tg}$  is considered equal to zero. The vertex is defined as the intersection point of the track plane and the beam ray. ( see Fig. 39 for basic variables) The BPM  $x_{tg}$  value is used to correct the momentum of the detected particle and the angle  $\theta_{tg}$  as

$$x_{tg} = \langle x|x \rangle^i x_{fp} + \langle x|\theta \rangle^i \theta_{fp} + \langle x|\delta \rangle^i \delta_{fp}, \quad (79)$$

and

$$\delta_{fp} = \frac{-\langle x|x \rangle^i x_{fp} + \langle x|\theta \rangle^i \theta_{fp}}{\langle x|\delta \rangle^i} + \frac{x_{tg}}{\langle x|\delta \rangle^i}, \quad (80)$$

which includes the correction, the second term, that can be used in writing the

$$\theta_{tg}^{corrected} = \theta_{tg} + x_{tg} \frac{\langle \theta|\delta \rangle^i}{\langle x|\delta \rangle^i}. \quad (81)$$

where the superscript  $i$  denotes the elements of the inverse of the first-order transport matrix (Eq. (73)).

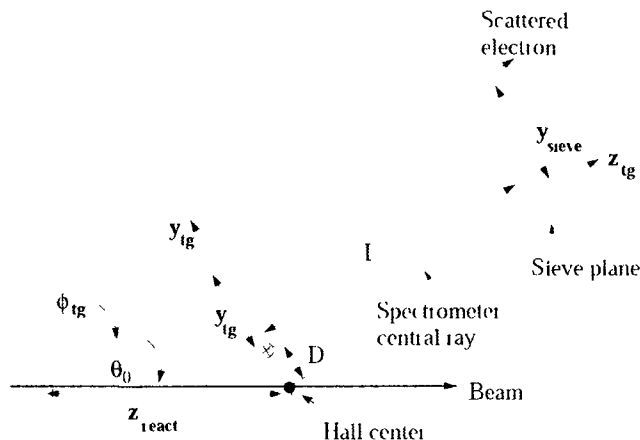


FIG. 39: Target coordinate system,  $L$  is the distance from the Hall center to the HRS sieve plane, while  $D$  is the horizontal displacement of the spectrometer axis from its ideal position. Spectrometer central angle is denoted by  $\Theta_0$ . Note that  $x_{tg}$  is vertically down (in to the page).

## VI.2 WAVEFORM ALGORITHM

The waveforms recorded for electromagnetic calorimeter and proton array signals are analyzed to extract time and amplitude information. the same method was utilized in cooking the raw data for both calorimeter and proton array signals.

### Reference Shape

The assumption that the signal shape is independent of its amplitude is the basis for the algorithm which is implemented for the analysis. Reference shapes for each individual block is basically the average shape of a pulse for each PMT in the calorimeter which extracted from the elastic calibration runs where the probability of pile-up events are rather small.

#### VI.2.1 The Amplitude of the Ideal Case

The ideal case will be the signal without any noise, knowing the only two free parameters, arrival time ( $t = 0$ ) and the pulse's amplitude ( $a$ ) which provides the best

fit to the signal  $\{x_i\}$  is the one which minimizes

$$\chi^2 = \sum_{i=0}^{127} (x_i - ah_i)^2, \quad (82)$$

where  $\{h_i\}$  is the reference shape and so

$$a = \frac{\sum_{i=0}^{127} x_i h_i}{\sum_{i=0}^{127} h_i^2} \quad (83)$$

In the real case, the arrival time is unknown and the fit for the ideal case is implemented for all possible arrival times by shifting the reference shape of a time  $t$ . Finally, for every amplitude identified by this way, one can compute the

$$\chi^2(a, t) = \sum_{i=0}^{127} (x_{i-t} - a(t)h_{i-t})^2 \quad (84)$$

of the fit which is ultimately used in defining the arrival time for the minimum  $\chi^2(t)$ . The Eq. (84) can be generalized and used for multi-pulse cases as

$$\chi^2(a_1, t_1, a_2, t_2) = \sum_{i=0}^{127} (x_i - a_1 h_{i-t_1} - a_2 h_{i-t_2})^2, \quad (85)$$

where  $t_1$  and  $t_2$  are the arrival times (in 1ns increment).

Among the important criteria in implementing the algorithm is to decide when a multi-pulse fit is necessary or whether a one-pulse fit is sufficient. The decision is made according to the value of  $\chi^2$  of the pulse-fit for the best arrival time. Moreover, using the whole 128 ns ARS window is redundant because of the fact that better quality fit is achieved with a time window of 20-30 ns for calorimeter and 50 ns for the proton array.

## VI.2.2 Real Case Implementations

### Baseline Fit

Fitting a constant to a signal is the simplest case where

$$\chi^2 = \sum_{i=i_{min}}^{i_{max}} (x_i - b)^2, \quad (86)$$

which is minimized at

$$b = \frac{1}{(i_{max} - i_{min})} \sum_{i=i_{min}}^{i_{max}} x_i, \quad (87)$$



where  $[i_{max}, i_{min}]$  is the portion of the ARS window for the analysis. Finally, if the

$$\chi_t^2 = \sum_{i=\chi_{min}^2}^{\chi_{max}^2} (x_i - b)^2, \quad (88)$$

is smaller than a  $\chi_0^2$  threshold to be determined, a “baseline” fit will be considered as a good fit.

### VI.2.3 One-Pulse fit

If the  $\chi^2$  from Eq. (88) is greater than  $\chi_0^2$  at least one-pulse must be fit. The amplitudes  $a_1(t_1)$  and the baseline  $b(t_1)$  verifying

$$\begin{pmatrix} \sum_{i=i_{min}}^{i_{max}} x_i h_{i-t_1} \\ \sum_{i=i_{min}}^{i_{max}} x_i \end{pmatrix} = \begin{pmatrix} \sum_{i=i_{min}}^{i_{max}} h_{i-t_1}^2 & \sum_{i=i_{min}}^{i_{max}} h_{i-t_1} \\ \sum_{i=i_{min}}^{i_{max}} h_{i-t_1} & \sum_{i=i_{min}}^{i_{max}} 1 \end{pmatrix} \begin{pmatrix} a_1(t_1) \\ b(t_1) \end{pmatrix} \quad (89)$$

minimize

$$\chi^2(t_1) = \sum_{i=i_{min}}^{i_{max}} (x_i - a_1(t_1)h_{i-t_1} - b(t_1))^2. \quad (90)$$

For every  $t_1$  within the time window of  $t_1^{min} \leq t_1 \leq t_1^{max}$ .

$$\chi_t^2(t_1) = \sum_{i=\chi_{min}}^{\chi_{max}} (x_i - a_1(t_1)h_{i-t_1} - b(t_1))^2 \quad (91)$$

is computed and the minimum value of  $\chi_t^2$  in this time window is compared to a  $\chi_1^2$  threshold to be defined. If it is smaller than  $\chi_1^2$ , a one-pulse fit will be considered as good fit.

### VI.2.4 Multi-Pulse Fit

With a similar approach as for one-pulse fit case, for every possible pair of arrival times  $t_1$  and  $t_2$  the  $\chi_t^2$  can be written as

$$\chi_t^2(t_1, t_2) = \sum_{i=\chi_{min}}^{\chi_{max}} (x_i - a_1(t_1, t_2)h_{i-t_1} - a_2(t_1, t_2)h_{i-t_2} - b(t_1))^2. \quad (92)$$

If the minimum value of  $\chi_t^2$  in the range  $t_1^{min} \leq t_1 \leq t_1^{max}$  and  $t_2^{min} \leq t_2 \leq t_2^{max}$  will be smaller than  $\chi_2^2$ , two pulse fit will be implemented.

The fitting algorithm parameters can be listed as

- Analysis window  $[i_{min}, i_{max}]$ ,

Analysis Window	$[i_{min}, i_{max}]$	[0,80]	Channel dependent
1 <sup>st</sup> -window	$[t_1^{min}, t_1^{max}]$	[-20,25]	Channel dependent
2 <sup>nd</sup> -window	$[t_2^{min}, t_2^{max}]$	[-20,25]	Channel dependent
Minimum Separation	$\Delta\tau$	4 ns	Fixed
0-pulse $\chi^2$ threshold	$\chi_0^2$	42 MeV	Channel dependent
1-pulse $\chi^2$ threshold	$\chi_1^2$	283 MeV	Channel dependent
2-pulse $\chi^2$ threshold	$\chi_2^1$	$\infty$	Fixed

TABLE 2: Calorimeter waveform analysis parameters.  $\chi^2$  of the fit computed in a 40 ns window which is centered around the minimum of the pulse though pulses were searched in a 45 ns time window (See Fig.55)

- first time window  $[t_1^{min}, t_1^{max}]$ ,
- second time window  $[t_2^{min}, t_2^{max}]$ ,

all of which depend on individual ARS channel. For example, cabling issues cause to arrive the signal at a different times in each detector. Besides, the last three of these free parameters change block by block.

In addition to listed parameters,  $\Delta\tau$  (minimum separation of a multi-pulse fit), and previously mentioned thresholds  $\chi_0^2$ ,  $\chi_1^2$ , and  $\chi_2^2$  can be seen in Table-(2).

### VI.3 ELECTROMAGNETIC CALORIMETER

The most important component of the DVCS experiments is the Electromagnetic calorimeter because of the fact that the reaction kinematics depends crucially upon the photon energy and position resolution. Thus, not only the detector capabilities in maintaining the accuracy of the photon energy and resolution, but also the algorithm that is implemented is important.

#### VI.3.1 Vertex Position Reconstruction

The next step is the calculation of the impact position  $x$  which is calculated as the sum of blocks positions  $x_i$  weighted logarithmically by the relative energy loss in each block:

$$x = \frac{\sum_i w_i x_i}{\sum_i w_i} \quad (93)$$

where

$$w_i = \max\left(0, \left[W_0 + \ln\left(\frac{E_i}{E}\right)\right]\right). \quad (94)$$

The photon total energy  $E$  is taken to be the sum over the energy loss  $E_i$  in each of the calorimeter blocks,

$$E = \sum_i E_i \quad E_i = C_i A_i, \quad (95)$$

The parameter  $W_0$  allows a further tuning of the relative weight among blocks. For example, whatever the energy loss, the weighting becomes uniform as  $W_0 \rightarrow \infty$ . Moreover, the value of  $W_0$  fixes the energy loss threshold for blocks to be taken into account in the position determination.

The distance between the calorimeter and the target is 110 cm. However, due to the size of the target cell, 15cm, vertex position in target needs correction. Besides, the electromagnetic shower starts at a certain depth rather than surface of the calorimeter block a comprehensive correction can be expressed

$$x_{corrected} = x \left(1 - \frac{a}{\sqrt{L_{vc}^2 + x^2}}\right) \quad (96)$$

where  $L_{vc}$  is the distance from the vertex to the calorimeter and  $a$  is the distance of the electromagnetic shower centroid to the calorimeter front face.

This correction algorithm was tested with the elastic run data and initially with optimized with the Monte Carlo simulation:

- Monte Carlo Simulation: 3 mm resolution around 3 GeV,
- Elastic Run: 2 mm resolution ( $\sigma$ ) at 110 cm and 4.2 GeV.

Thus it is fair to say that we are able to determine the impact position of the photon at the front face of the calorimeter with a resolution which is times better than the individual block size.

### VI.3.2 Clustering Algorithm

For each event, several particles can hit the calorimeter, and these particles are identical in terms of the characteristics that is manifested in detector and arrive perfectly in time as DVCS photons. In order to separate these particles, spatial clustering is implemented for these kind of event. Moreover, the electromagnetic decay of  $\pi_0$  generates partially overlapping electromagnetic showers as a result of the

decaying mechanism. The minimum angle between generated photons is  $5^\circ$  for a  $\pi^0$  decay which ensues the fact that there are at least two calorimeter blocks between the impact position of these two photons. The goal of the cluster algorithm is to separate blocks belonging to each of the two showers.

The cluster separation is implemented by the algorithm that is based on a cellular automata [102] which is illustrated in Fig. (40). The initial step is the identifying local maxima which are infected by viruses and then the contamination starts. Each neighboring blocks of which is above a common set threshold are contaminated unless they were already contaminated. The value of the maximum is copied into the contaminated block and the next contamination starts until the all neighbor blocks reach the energy threshold.

#### VI.4 PROTON ARRAY

The waveform analysis algorithm of the proton array is same as the calorimeter. As a result of the fact that while the DVCS photons are highly energetic ( $E_{\gamma_{DVCS}} \geq 1.5 \text{ GeV}$ ) and the recoil proton is not, a couple of significant consequences arise:

- event though the algorithms are same, the proton array waveform algorithm parameters are different than calorimeter parameters (Table-3) ,
- one can set a threshold of 1 GeV for photons, which eliminates fair amount of the background, while a threshold of 30 MeVee is set for proton array,
- energy loss by a proton in the detector can go down to zero

In order to set an optimal energy threshold a detailed study of deposited energy in scintillator blocks performed (see section VII.5.2).

In context of this thesis a relative optimization through iterating the calorimeter photon energy to improve the missing mass squared resolution. This will be discussed in section VII.2.3.

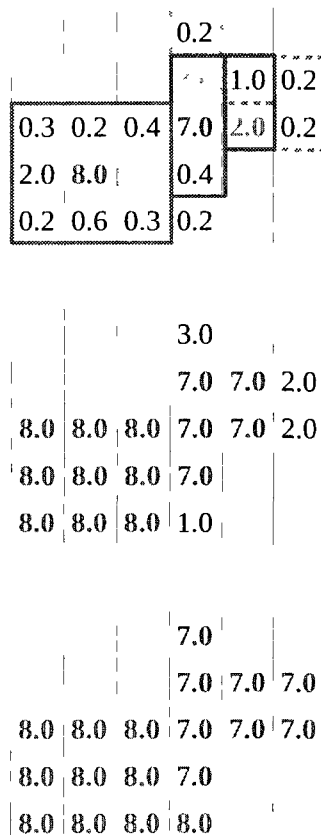


FIG. 40: Illustration of the cellular automata procedure. At every step each cell takes the value of its highest energy neighbor. When a cell gets the value of one of the local maximum first determined, it does not change anymore. At the end the process, all cells with the same value form a cluster.

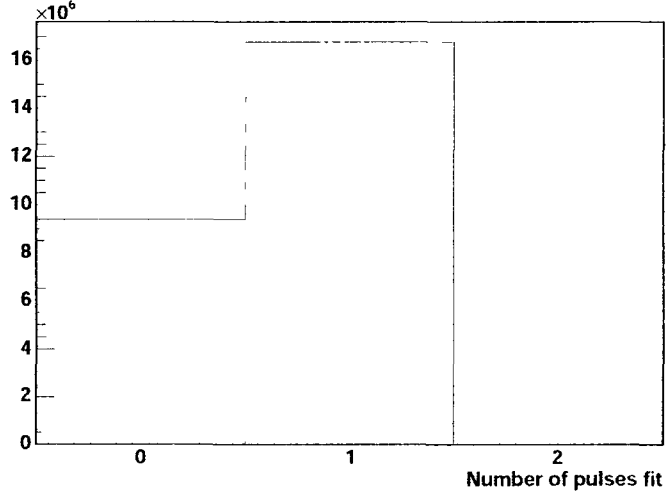


FIG. 41: Calorimeter ARS wave form analysis for kinematics 3. The number of pulses fit presented here as an average over the whole calorimeter. As consequence of higher backgrounds the blocks closer to the beam line have higher number of pulses fit.

Analysis Window	$[i_{min}, i_{max}]$	[45,75]	Channel dependent
1 <sup>st</sup> -window	$[t_1^{min}, t_1^{max}]$	[-20,20]	Channel dependent
2 <sup>nd</sup> -window	$[t_2^{min}, t_2^{max}]$	[-20,20]	Channel dependent
Minimum Separation	$\Delta\tau$	4 ns	Fixed
0-pulse $\chi^2$ threshold	$\chi_0^2$	2.3 MeV	Channel dependent
1-pulse $\chi^2$ threshold	$\chi_1^2$	15.3 MeV	Fixed
2-pulse $\chi^2$ threshold	$\chi_2^1$	$\infty$	Fixed

TABLE 3: Proton Array waveform analysis parameters. Raw ARS data was analyzed with the same algorithm as in the case for calorimeter, however as it can be seen the parameters are different.  $\chi^2$  of the fit computed in a 40 ns window which is centered around the minimum of the pulse and different than the calorimeter case, the pulses were searched in 40 ns time window.

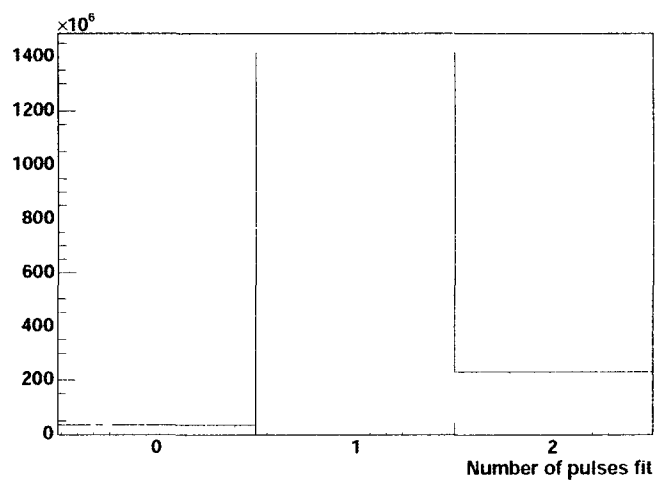


FIG. 42: Proton array ARS wave form analysis for kinematics 3. The number of pulses fit presented here as average over the whole detector. As a consequence of higher backgrounds the blocks closer to the beam line have a higher number of pulses fit.

## CHAPTER VII

### DATA ANALYSIS

This chapter describes the global calibration of detectors and E-00110 triple coincidence data analysis including the detailed event selection along with the missing mass squared study for proton array and calorimeter which entailed a re-calibration of data and additional photon energy smearing to Monte Carlo simulation.

#### VII.1 KINEMATIC SETTINGS

The connection between the theory and the experiment is conditioned by the kinematical settings of the experiment. Thus, three kinematical settings at three different values of  $Q^2$  and fixed  $x_B$  were made in the E00-110 experiment.

All the experimental constraints displayed in Fig. (43). In the experimentally allowed regions three kinematical points at different  $Q^2$  and fixed  $x_B$ . The squared points in the Fig. (43) are the chosen kinematics which are summarized in Tab. (3).

In this triple coincidence analysis kinematics 3 data is used.

#### VII.2 GLOBAL CALIBRATION OF DETECTORS

The HRS, the electromagnetic calorimeter, and the proton array calibrations will be discussed in details in this section.

##### VII.2.1 HRS Calibration

The key concept in HRS calibration is the reconstruction which is implemented by transport matrix of Eq. 73 which requires dedicated runs and long optimization calculations. On the other hand, the transport matrix element of a previous experiment were used along with magnet configurations, therefore, no optics calibration was necessary for the E-00110 DVCS experiment. However, to ensure the quality of the the data, two optimization seemed to be necessary[99].

##### TDC Optimization

Particle tracking is utilized through the VDC planes which combined along with the TDC information and the relation ship between drift time and drift distance. Quite



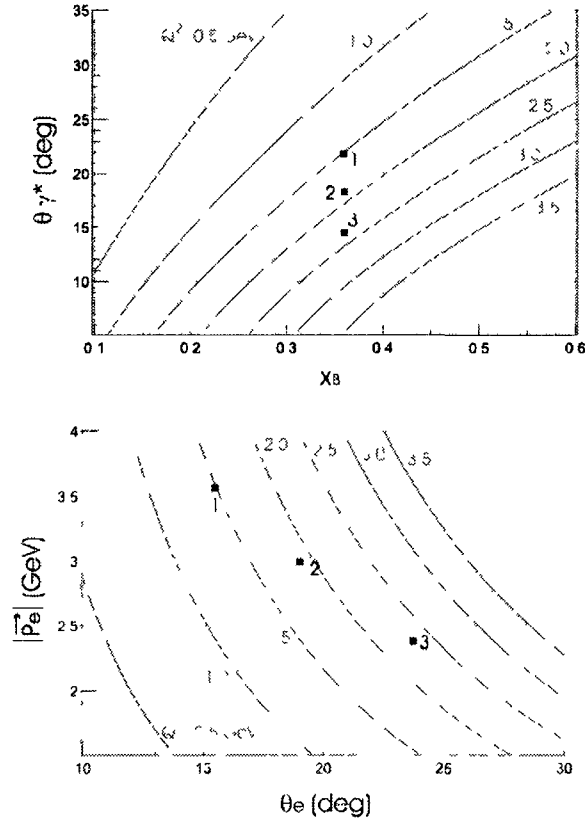


FIG. 43: Top: angle between the virtual photon and the electron beam as a function of  $x_B$ , curves for constant  $Q^2$  and constant  $s$  are plotted. Bottom: scattered electron momentum magnitude as a function of the scattering angle; curves for constant  $Q^2$ , constant  $s$  and constant  $x_B$  are also plotted. Shaded zones in both figures corresponds to experimental constraints. (Figures are taken from [61])

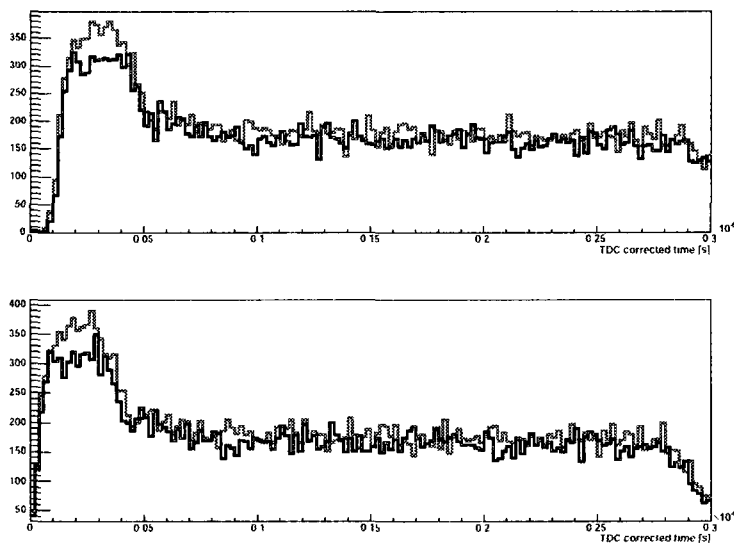


FIG. 44: TDC corrected time for two different bunches of 16 wires of one VDC plane, before (top) and after (bottom) the offsets optimization. The TDC offset observed in the upper plot is corrected after the optimization.(Figure taken from [61])

often the wire cells in this system can presume that zero drift time corresponds to a zero drift distance. In order to make sure this is not the case, TDC offsets for each VDC wire were optimized using a single arm HRS run on LH2 target. The wires in in each VDC plane grouped in bunches of 16 and then these bunches are physically grouped in a same TDC module. Each TDC spectrum was smoothed and derivated and the maximum slope point was adjusted to the same value close to zero.

During the experiment, five weeks later, an equivalent run taken and analyzed with the same procedure as at the beginning. The results were in similar quality and proving the stability of the correction the during the whole experiment.

## VII.2.2 Calorimeter Calibration

Before experiment started initial calibrations performed in order to adjust the gain in each calorimeter channel using mainly cosmic rays and LED monitoring system. In addition to these tests, a calibration performed with elastic scattering at the beginning and the end of the experiment. This section covers briefly these two

process based on [61].

### Cosmic Calibration

Energy deposition of minimum ionizing particles only depends on the length of the material they pass through. In the case of DVCS calorimeter consisting of  $PbF_2$  crystals, the deposited energy is around 35  $MeV$  per block which is sufficient to cross-calibrate all calorimeter channels by adjusting the high voltage of each PMT to get the same energy amplitude for same energy deposition.

The cosmic ray data were analyzed by simply identifying the ARS sample with the largest amplitude within the 128 ns window. Waveform analysis of the cosmic ARS signal was not used because the chances of getting two cosmic per event is almost zero.

Two scintillator paddles were used to trigger the cosmic read-out of the calorimeter having the fact that since the solid angle of the paddles varies for each block, energy distribution varies as well. In order to minimize the negative effects of this variation in the calibration procedure, only the vertical cosmic were taken into account. The result of this calibration can be seen in Fig. 45 in which a cross calibration up to 2.7 % shown. However, the systematics of the cross calibration might be larger than this value. Therefore, a completely different another calibration procedure implemented as well.

### LED Calibration

As a second method for cross calibration LED calibration was implemented because the electromagnetic calorimeter is equipped with a LED monitoring system based on three pulsed and one continuous LEDs. The LED system maintains exactly the same signal since the same LED moves in front of each block. This property provides not only a reliable calibration but also, reliable continuous monitoring during experiment.

Sensitivity of LED measurement relies on the position of LEDs with respect to calorimeter surface. Precise collimation of LED motion plane with respect to calorimeter surface, allows measurement to be less sensitive to the distance in between them. Another important issue is the determination of the block centers, that is the positions where the LED carrier must be stopped to illuminate each block. A thorough scan can be implemented, however it takes several hours therefore only four corner blocks were determined and inferred to the rest of the calorimeter.

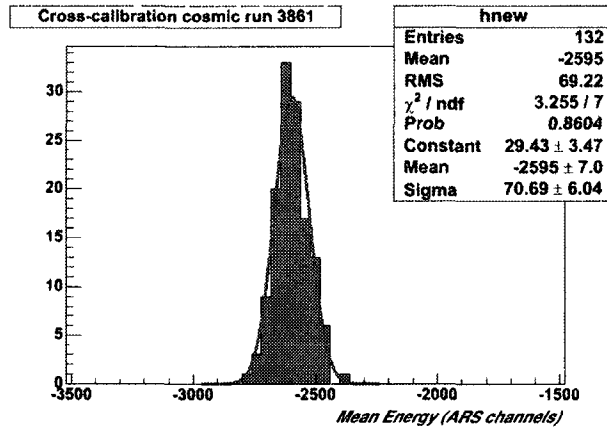


FIG. 45: Cross calibration with cosmic data. The dispersion distribution width is 2.7 % of its mean.

The results of this LED cross calibration can be seen Fig. (46). It shows the signal integral for all channels with the HV obtained by cross-calibrating with cosmics. Results obtained with this independent method of cross calibrating the calorimeter blocks are within 9%.

### Elastic Calibration

The more complete response study of the electromagnetic calorimeter was accomplished by utilizing the elastic scattering ( $ep \rightarrow e'p'$ ). The scattered electron is detected in the calorimeter and recoil proton detected in the HRS.

The calibration implemented with a global fit of all calibration coefficients to best reproduce the data. For an event  $j$ , considering the target proton at rest and neglecting the electron mass, conservation of energy yields the following energy  $E_j$  for the scattered electron:

$$E_j = E_b + m - E_j^p \quad (97)$$

where  $E_b$  is beam energy,  $m$  proton mass, and  $E_j^p$  is the recoil proton energy for that event, measured in the HRS.

If we call  $A_j^i$  the signal amplitude of calorimeter block  $i$  in event  $j$ , and  $C_i$  the

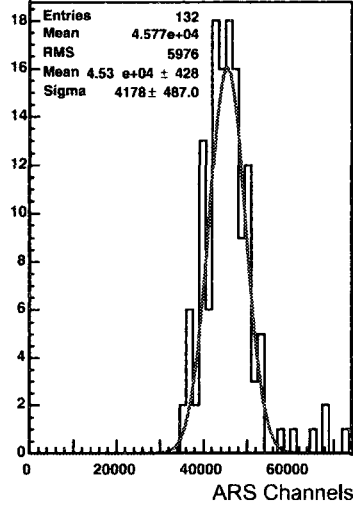


FIG. 46: Calorimeter cross-calibration as measured by LEDs for the HV calculated with cosmic runs.

block calibration coefficient, we can define a  $\chi^2$  as:

$$\chi^2 = \sum_{j=1}^N \left( E_j - \sum_i C_i \cdot A_j^i \right)^2 \quad (98)$$

where  $N$  is the total number of events and the sum over  $i$  runs for all blocks belonging to the reconstructed calorimeter cluster for event  $j$ .

Then the calibration coefficients minimizing the above  $\chi^2$  are:

$$\frac{\partial \chi^2}{\partial C_k} = -2C_k \sum_{j=1}^N \left( E_j - \sum_i C_i \cdot A_j^i \right) A_j^k = 0 \quad (99)$$

which yields

$$\sum_i \left[ \sum_{j=1}^N A_j^k A_j^i \right] C_i = \sum_{j=1}^N E_j A_j^k. \quad (100)$$

Finally, calibration coefficients can be obtained by inverting the  $132 \times 132$  matrix  $M_{ik} = \sum_{j=1}^N A_j^i A_j^k$ .

Because of the small acceptance of HRS, at a distance of 1.1 m from target only a small portion of the calorimeter is hit by the elastic electrons. Therefore, the calorimeter moved to a farther distance of 5.5 m which provides better acceptance[100, 101].

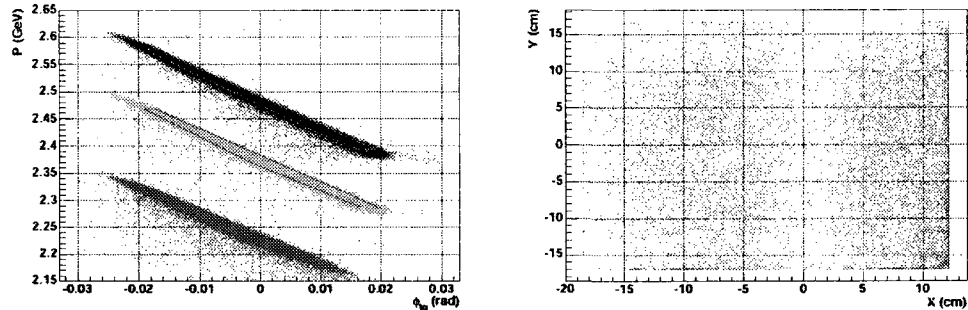


FIG. 47: Left plot is the proton momentum versus the scattering angle for each elastic settings. Cuts applied to select elastic events are shown in red. The corresponding impact point on the calorimeter is shown in the right plot.

A cut on HRS variables was performed to select good elastic events. The reconstructed momentum versus the scattering angle  $\phi_g$  for each elastic setting together with the corresponding impact position on the calorimeter (can be seen in Fig. (47)).

Two elastic calibrations were performed, the first one a few weeks after the experiment started and the second one a few weeks before the experiment completed. In order to maintain a good energy resolution along the experiment, an interpolation of calibration coefficients between these two calibrations was necessary, together with an extrapolation before and after them. The results of these two calibrations demonstrated in Fig.(48) .

### VII.2.3 Proton Array

Similar to the calorimeter calibration procedure, HRS vertical acceptance is the determining factor in the calibration procedure of proton array. As a result of small vertical acceptance, in the case of detecting elastic protons in HRS, one observes no correspondent elastic electron events in the proton array. Therefore, proton detector

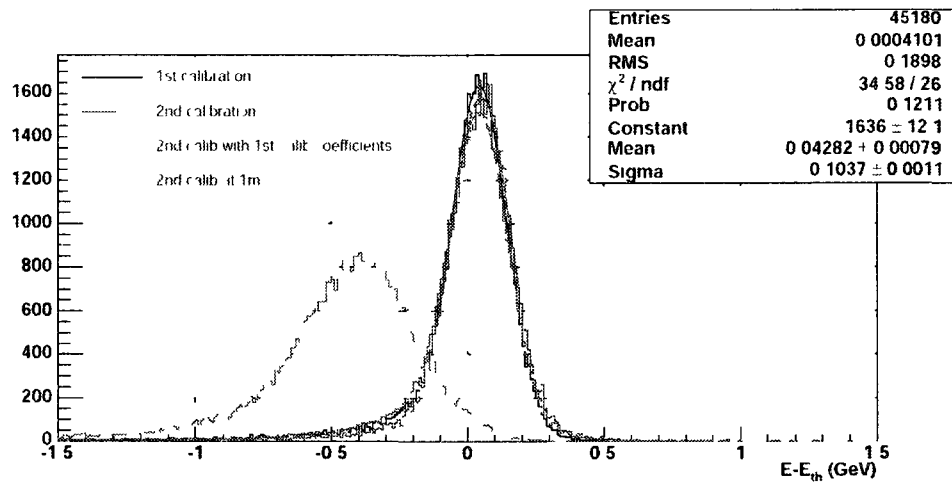


FIG. 48 Energy resolution obtained in both elastic calibration  $2.4\%$ , the average energy of the incident electron is  $4.2 \text{ GeV}$ . The results of the second calibration when first calibration coefficients are used are also plotted to show the necessity of a careful monitoring of the coefficients between these two calibration points.

calibration was performed by a method which based on selection of DVCS events with very tight cuts. Then, a prediction algorithm implemented based on the HRS and calorimeter information (DVCS events) so that the proton array block to be hit by proton can be predicted along with the predicted energy deposition. As discussed in proton array brings challenges, such as DVCS events do not cover the proton array uniformly. For example, in the large  $t$  settings, the outer blocks are hit, on the contrary inner blocks are hit for low  $t$  settings. An example of this variation can be seen in Fig. (49).

Therefore, in order to accomplish enough statistics in each block to calculate its calibration coefficient, the calibration implemented separately for each kinematic setting. Fig. (51 & 52) show some results after calibration performed.

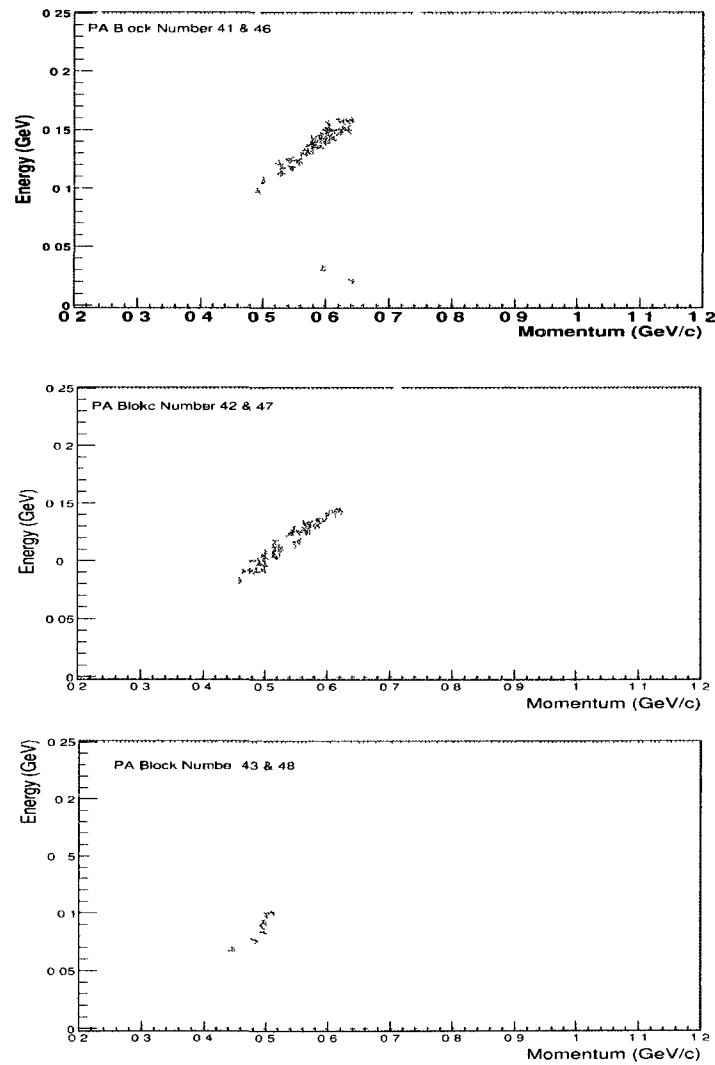


FIG 49 Deposited energy versus momentum distribution generated by using the kinematics 3 of E-00110 experiment. Each plot consists of two proton array blocks: 41 & 46 (outer lane blocks), 42 & 47 (middle lane blocks), and 43 & 48 (inner lane blocks) of the core region of the proton array. (See Fig. 60)



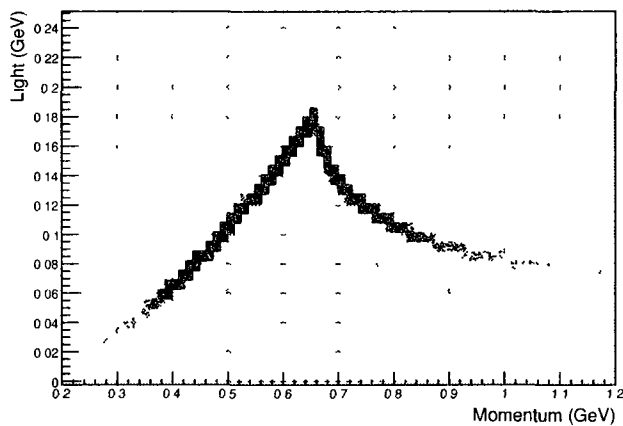


FIG. 50: Simulated light and momentum in Proton Array

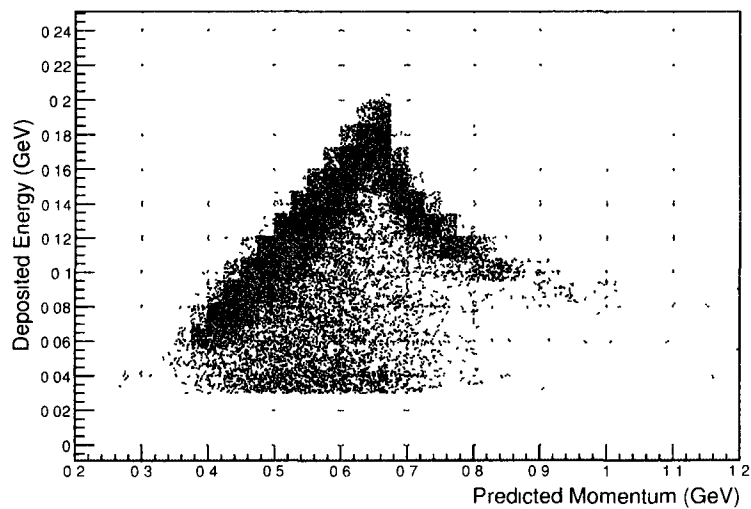


FIG. 51: Measured energy versus predicted proton momentum for all proton array blocks after the calibration performed.

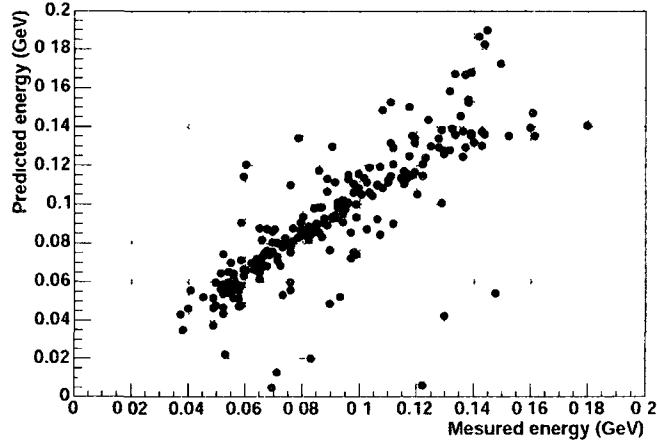


FIG. 52: Measured energy versus predicted energy for proton array block number 53 after the calibration performed.

### VII.3 SELECTION OF ELECTRON EVENTS

#### VII.3.1 Electron Identification

The standard Čerenkov detector package discussed in VII.2.3 was used for particle identification of E00-110 experiment. The two possible signal contamination to the DVCS electron signals 1-photoelectron signal and  $\delta$ -ray. To be able avoid the events associated with 1-photoelectron events, as it can be seen a cut is applied at the value of 150 ADC channels (Fig.53). The  $\delta$ -ray can be produced by scatterings of pion on an atomic electron of the gas, which in turn generates an electron signal. Thus the purity of the electron sample is not 100 % rather a value around 98.8% based on the Čerenkov commissioning.

#### VII.3.2 Electron Events Cuts

##### Acceptance Cut

Trajectories far from the nominal acceptance of the spectrometer are poorly reconstructed. Besides, a cut defining the HRS acceptance must be applied to be

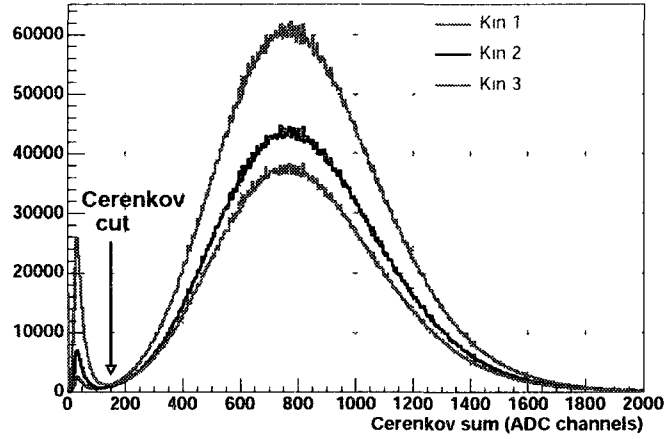


FIG. 53: Distribution of the sum of all Čerenkov mirrors, for each kinematic settings. The first peak in this distribution corresponds to 1-photo-electron signal due to the electronic noise. In order to remove this contamination a Čerenkov cut is applied at Čerenkov sum value of 150 ADC.

able to compute the solid angle of the experiment accurately. The acceptance region depends on 5 variables which are discussed in VI.1.2 as well:  $x_{tg}$ ,  $y_{tg}$ ,  $\theta_{tg}$ ,  $\phi_{tg}$  and  $\delta_{tg}$ . Implementing the cuts to these correlated variables, entails more complications. However, M. Rvachev et al. [104] developed a comprehensive acceptance function, called R-function which allows to implement a four dimensional. R-function implemented to E-00110 data, and details can be found in [61].

### Target Length Cut

The overall location of the target relative to the Hall center is 7.8 mm downstream. In order to preclude the contribution from the target cell wall a cut

$$-6.00\text{cm} < v_z < 7.50\text{cm} \quad (101)$$

where  $v_z$  is the reaction point along the beam, is implemented. The resolution of the vertex is determined from data reconstruction on a multi-foil carbon target (Fig. 54). The luminosity will be calculated from measured electron beam charge with the assumption of 13.5 cm fiducial length for the target.

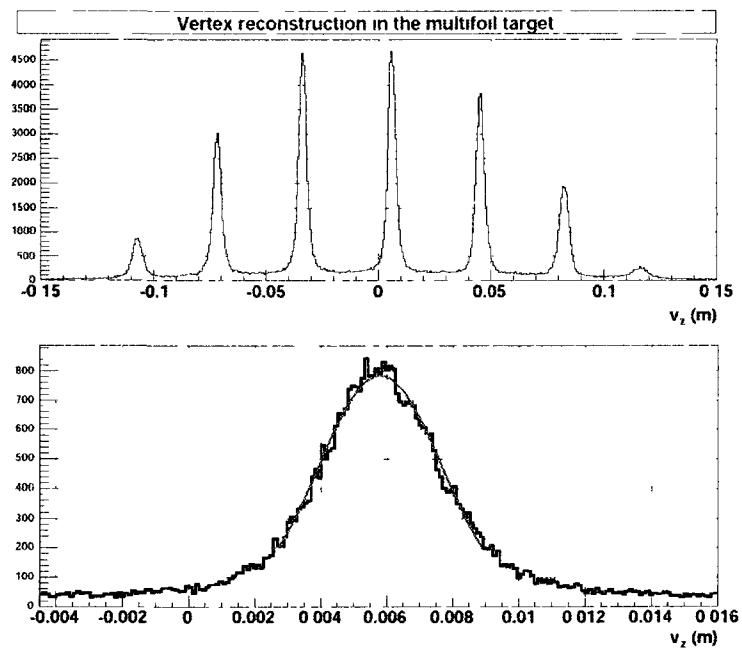


FIG 54: The upper figure illustrates the resolution of the vertex reconstruction on a multi-foil target. The bottom figure illustrates the central foil fit leads to  $\sigma=1.9$  mm. The foil thickness is 1mm and the HRS was at  $37.69^\circ$  during this run. The measured  $\sigma$  at this angle is 1.87 mm that means a  $\sigma$  value of 1.2 mm at  $90^\circ$ . Therefore, the introduced  $\sigma$  value of  $1/\sqrt{12}$  for foil thickness can be ignored.

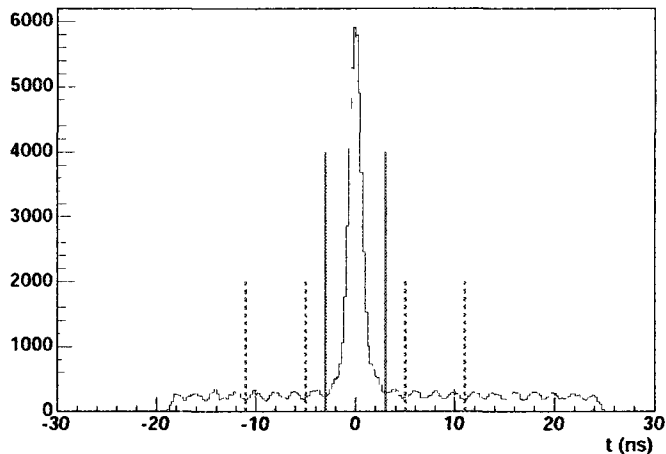


FIG. 55: The 45 ns time window of the waveform analysis for the calorimeter blocks in kinematic 3 with  $E > 300\text{MeV}$ . Here in this plot the coincidence  $[-3,3]$  time window used for clustering is shown by solid lines. The time resolution is 0.6 ns.

## VII.4 SELECTION OF PHOTON EVENTS

Previously discussed waveform analysis is the major selection criteria for photon event selection. For example, only selecting 80 ARS channel out of 128 provides lesser contamination of accidentals to the DVCS events.

### VII.4.1 Clustering Time Window

The preliminary calorimeter event selection discussed in VI.3.2 whereas the cluster algorithm determines the local energy maxima and therefore, with in the the clustering time window ( $[-3,3]$ ns, Fig. (55)) the number of local energy maxima is defined as number of clusters. Fig. (55) shows the calorimeter time spectrum for kinematics 3.

The coincidence time window is set by a time cut of  $[-3,3]$ ns which is more than  $3\sigma$  and the number of events missed by this cut is less than 0.02%. Therefore, this narrow cut can safely be applied. The Fig. (56) shows the number of clusters in time window of  $[-3,3]$ ns for kinematics 3. The key selection based on the number

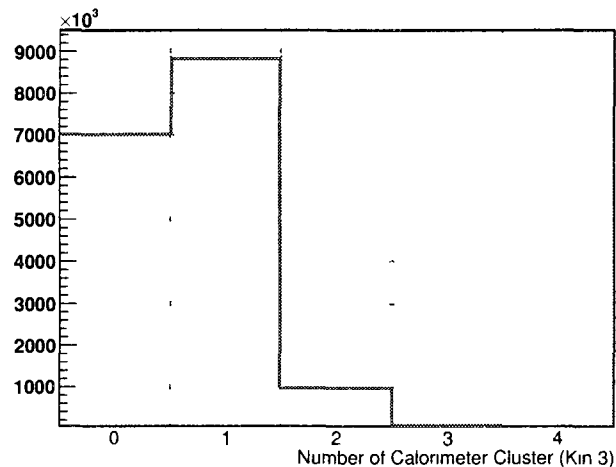


FIG. 56: Number of calorimeter clusters in the coincidence time window for kinematics 3.

of cluster is that the events having the number of calorimeter cluster equal to one selected. This selection provides more reliable information on DVCS events, because of the fact that the number of calorimeter cluster corresponding to two, can originate from the decay of a  $\pi^0$  to two photons. (This will be discussed in section VII.5.3)

#### VII.4.2 Geometrical Acceptance of Calorimeter

The geometrical cuts applied to the calorimeter is also applied as:

$$\begin{aligned}
 -15\text{cm} < x_{calo} < 12\text{cm}, \\
 -15\text{cm} < y_{calo} < 15\text{cm}.
 \end{aligned}
 \tag{102}$$

where  $x_{calo}$  and  $y_{calo}$  are reconstructed positions of clusters in the calorimeter. As it can be seen in Fig. (25) the geometrical center of the calorimeter is shifted from the beam line for about 1.5 cm. Therefore, the origin of these coordinates is the intersection point of a line parallel to the front face of the calorimeter with a normal passing through the center of the Hall.

This geometrical cut removes the edge blocks as can be seen in Fig. (58) which correspond to the events with poorly reconstructed as most of the electromagnetic showers are not detected. Moreover, this cut removes the edge blocks which have higher background rates.

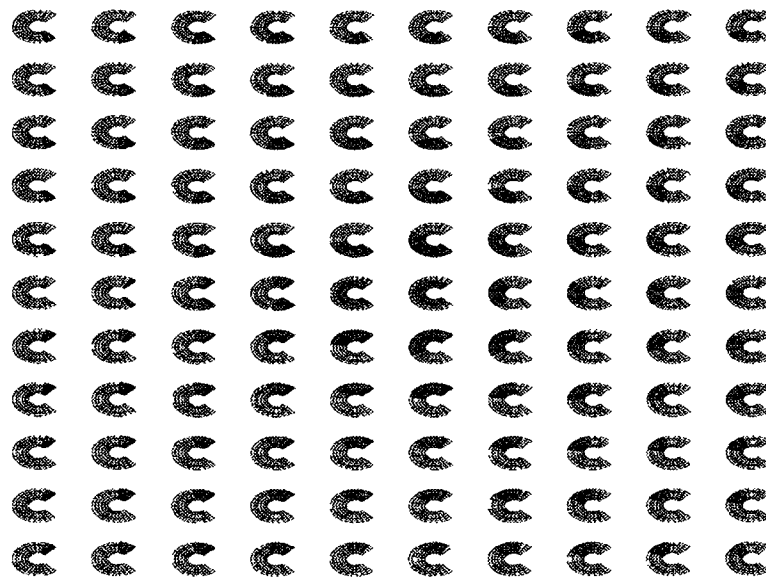


FIG. 57: Simulated triple coincidence events in corresponding calorimeter towers. The nature of the triple coincidence particle detection in E00-110 experiment causes the fact that not all DVCS photons, detected in the electromagnetic calorimeter, have the corresponding recoil proton detected in the proton array simply because of the detector's geometry. Furthermore, the geometrical acceptance of the calorimeter is affected by the core region cut that is applied to proton array.

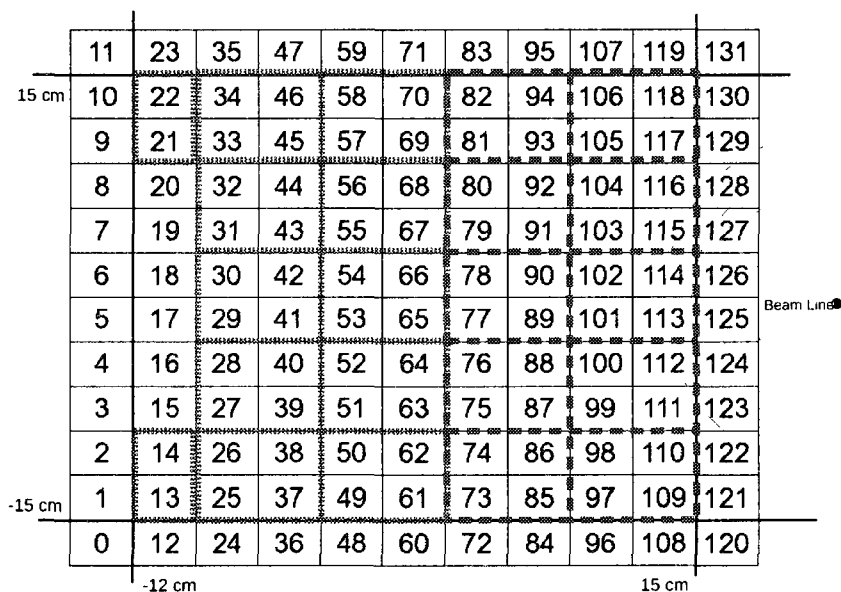


FIG. 58: The extended solid lines represent the geometrical limits expressed in (112) which removes 42 edge calorimeter blocks in total. The blocks in the dashed line region (blue) and the ultra-fine dashed line region (red) grouped in four in order to study the missing mass squared in the calorimeter. As can be seen in Fig. 57 not all calorimeter blocks have the triple coincidence event because of the proton array geometry. Therefore, the calorimeter blocks in the limits of (112) grouped in four to study the missing mass squared.



## VII.5 SELECTION OF PROTON EVENTS

Proton event selection is very much inter-related to missing mass squared study. Therefore, some part in this section will be discussed in the details later.

### VII.5.1 Photon Energy Exclusivity Re-Normalization and Proton Prediction

Following the electron and photon event selections, the missing mass squared

$$M_{ep \rightarrow e\gamma X}^2 = (k + p - k' - q'_{calo})_\mu^2 \quad (103)$$

is constructed for  $H(e, e', \gamma)X$  (double coincidence) with an initial cut of  $M_X^2 < 1.75 \text{ GeV}^2$ .

The photon energy of each event passing the missing mass cut is re-normalized as (illustrated in Fig. (59))

$$q'_{exc} = q'_{calo} \alpha_{exc}$$

$$q'_{exc} = q'_{calo} \frac{W^2 - M^2}{W^2 - M_X^2} \quad (104)$$

in order to obtain the corresponding exclusive  $H(e, e', \gamma)p$  kinematics. This re-normalization is the assurance of having the DVCS event in the double coincidence region. Thus, the direction of the recoiled proton then can be predicted by

$$p'_{exc} = p + q + q'_{exc}. \quad (105)$$

Utilizing the proton prediction, a directivity cut is applied to the direction of the recoil proton. This cut requires that the direction of  $\hat{p}'$ , from the vertex point to the *core* region of the proton array defined as

$$1 < y_i < 5,$$

$$2 < x_i < 19 \quad (106)$$

where the block coordinates  $(x_i, y_i)$  are defined for detector such that the tower index  $x_i$  varies from 1 to 20 and the polar index  $y_i$  varies from 1 to 5 for the 100 proton array elements. Fig. (60) shows the core region and block coordinates in details.

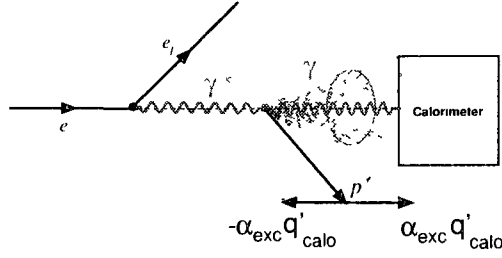


FIG. 59: Photon energy exclusivity re-normalization

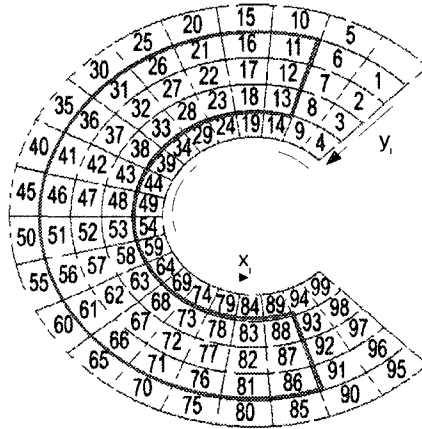


FIG. 60: Showing fiducial cut implemented to the proton array based on the fact that expressed in Fig (31) Thereafter in the text, the region displayed by solid lines is referred as the core region of the proton array. The coordinates shown as  $x_i$  and  $y_i$  proton array coordinates to extract block number.

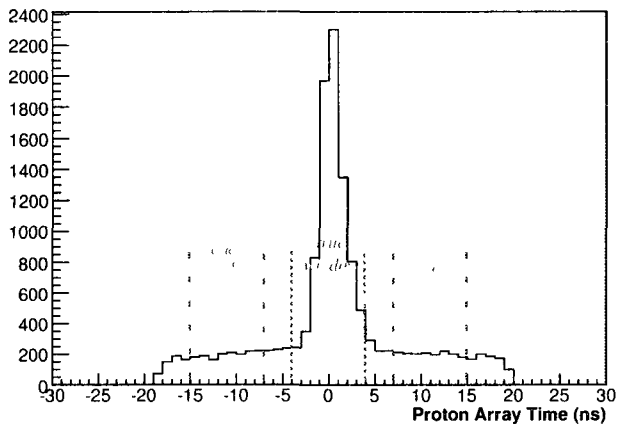


FIG. 61: Proton array time distribution displayed here is after the applied energy threshold is 30 MeVee (MeV electron equivalent, a deposited energy of 1 MeV generates 1 MeVee in light output at linear light yield).

### VII.5.2 Energy Threshold

Unlike the calorimeter, a high threshold can not be set for the proton array because of the fact that we are interested in detecting the very low energy momentum protons (can go down as low as 200 MeV). In order to determine the energy threshold for proton event selection, we performed a study on the ARS pulse heights in the PA which are converted to Energy Deposited (electron equivalent). The PMTs measures the light yield in the scintillator which is encoded in Birks' law [113] as

$$\frac{dL}{dx} = \frac{A dE/dx}{1 + k_B dE/dx} \quad (107)$$

$A$  and  $k_B$  are empirical constants that depend on the material and have to be determined from data.

For each accepted ( $H(e, e'\gamma)X$ ) event in the true triple coincidence window (Fig. 61), we look for a coincidence signal in the block  $(x_i^p, y_i^p)$  predicted by the recoil  $p'_{exc}$ . Moreover, we developed an algorithm such that any coincidence signal in 8 surrounding blocks  $(x_i^p \pm 1, y_i^p \pm 1)$  recorded so that because of the geometry of the detector recoil proton may hit the predicted block and deposit more energy to an adjacent block cases recorded as well (See Fig. 62).

The energy deposited for each nine blocks in our algorithm plotted after the background subtraction (this will be discussed in VII.5.3) and results can be seen

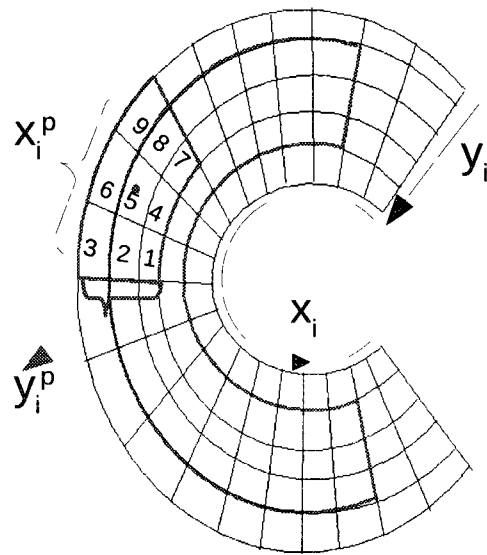


FIG. 62: Predicted block is the central block and we look for the eight surrounding blocks

in Fig. (63). Based on final deposited energy distributions in the predicted block, having a cut at 30 MeV for all triple coincidence events provides us cleaner data.

### VII.5.3 Background and Accidentals

In VII.5.2 a background subtraction implemented to the energy deposited in proton array block. This subtraction includes two separate sources: background and accidental.

#### Accidentals

Accidental event selection is performed for both calorimeter events and proton array events with same method. This is simply performed by identifying events in an accidental time window.

Calorimeter accidental time window, can be seen in Fig. (55), is

$$\begin{aligned} -11ns < t_{calorimeter} < -5ns, \\ 5ns < t_{calorimeter} < 11ns. \end{aligned} \tag{108}$$

The  $H(e, e'\gamma)X$  events are analyzed with same algorithm as they are analyzed in the true calorimeter time window.

Proton array accidental time window, can be seen in Fig. (61), is

$$\begin{aligned} -15ns < t_{proton\ array} < -7ns, \\ 7ns < t_{proton\ array} < 15ns. \end{aligned} \tag{109}$$

The  $H(e, e'\gamma)p$  events are analyzed in these time window in order to accidental distribution for triple coincidence events.

#### Backgrounds

There are several reaction that can intervene with DVCS or can mimic DVCS reaction so that it becomes necessary to separate these events from the data. Some reactions can be separated by a proper threshold on energy, or a missing mass squared cut. However, for reactions such as electroproduction of  $\pi^0$  an event by event subtraction is required to separate them from data.

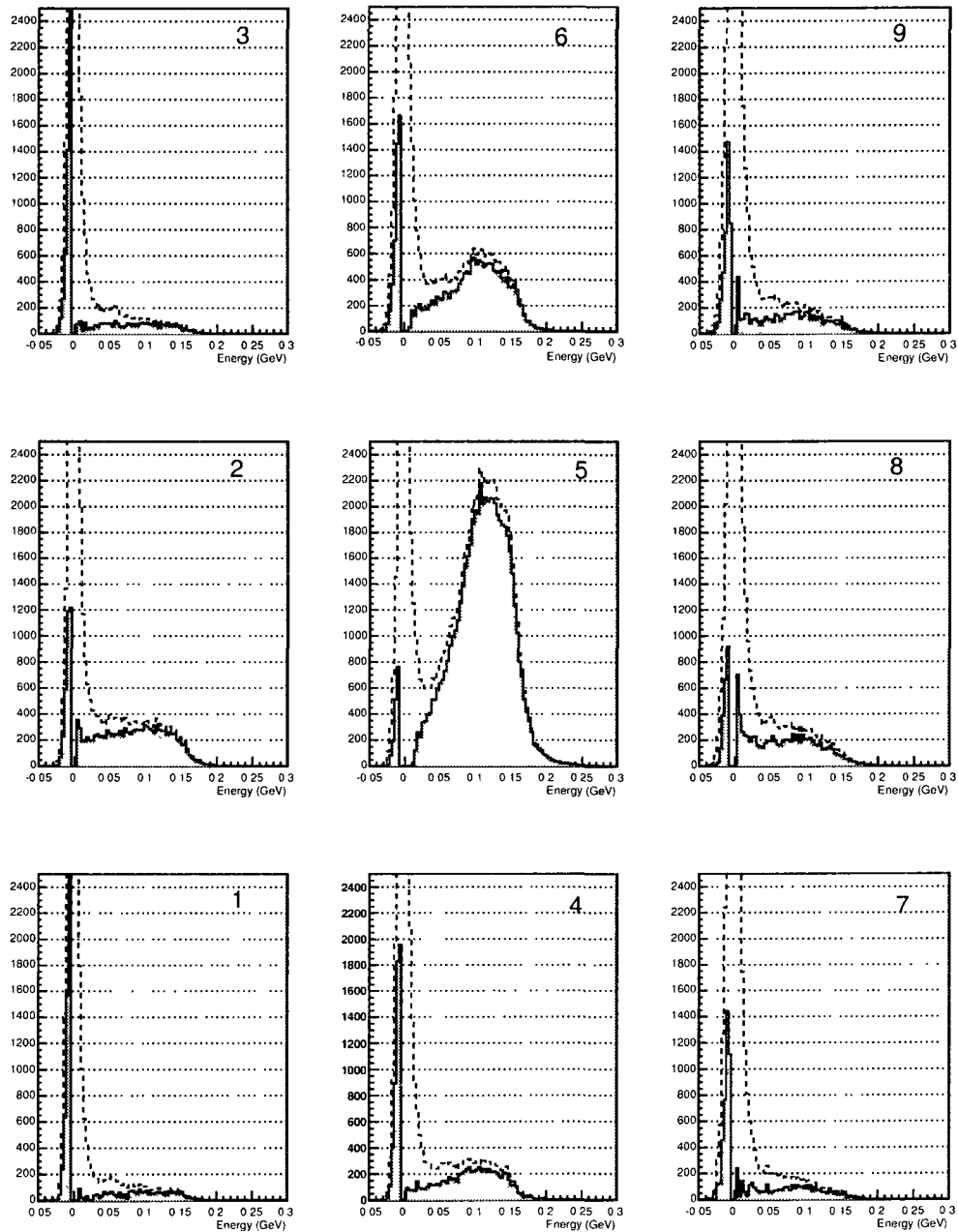
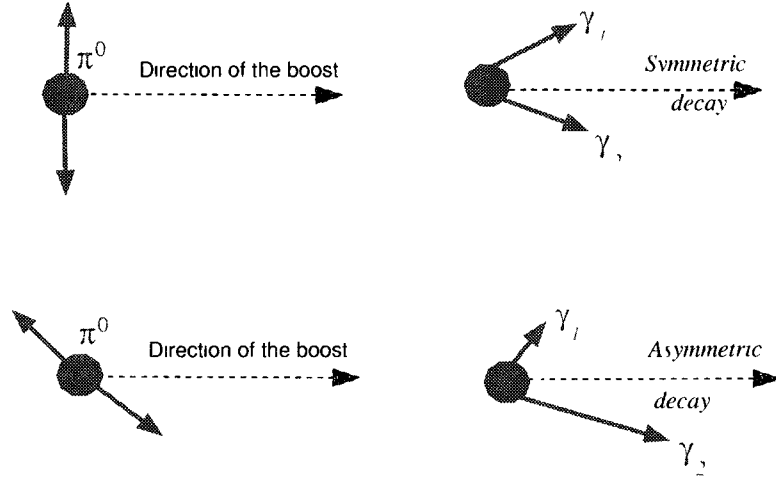


FIG. 63: Energy deposited in proton array blocks with grouping in nine algorithm. Corresponding block position to the numbers in each block can be seen in Fig. (62) Dashed curves are before the background subtraction and the filled curves is after the subtraction. The deposited energy distribution in the central block shows that algorithm that we developed works and an energy threshold value of 30 MeVee is reasonable to perform the analysis.

FIG. 64: Symmetric and asymmetric  $\pi_0$  decay

**Associated DVCS (non-resonant):** This reaction ( $ep \rightarrow e'p'\gamma\pi^0$ ) consists of the emission of an additional  $\pi^0$ [112]. This reaction has a missing mass squared starting at  $(M_p + m_{\pi^0})^2$  in which the  $\pi^0$  emitted collinear to the proton. Moreover, the higher the  $\pi^0$  momentum (relative to the recoil proton) the higher the missing mass squared. Therefore, having a missing mass squared cut at value of  $M_p + m_{\pi^0}$  on data removes this contamination. However, due to the resolution effects, a small fraction can not be removed especially for the double coincidence missing mass squared.

**Associated DVCS through a resonance:** The resonance in ( $ep \rightarrow e'(\Delta \text{ or } N^*)\gamma$ ) decays into a nucleon and a pion. In the case of  $\Delta(1232)$  resonance gives a contribution to the missing mass squared distribution at around  $1.5 \text{ GeV}^2$ . Having above mentioned missing mass squared ( $M_X^2 < (M_p + m_{\pi^0})^2$ ) cut on data will remove this contamination.

**Electroproduction of  $\pi^0$ :** The kinematics of this reaction ( $ep \rightarrow e'p'\pi_0$ ) is similar to DVCS where rather than having a real photon in the final state, it has a  $\pi_0$  which decays into two photons (Fig. (64)).

When the final state  $\pi_0$  decays through symmetric process, both photons hit calorimeter. In our experimental kinematics, the maximum  $\pi_0$  energy is around 3.5 GeV which entails the smallest angle value of  $4.4^\circ$  between the two photons. Consequently, this corresponds to  $\approx 9$  cm separation on the calorimeter surface. Each calorimeter block has a transverse size of 3cm which at distance of 1.1m correspond  $1.6^\circ$ . Thus, for  $\pi_0$  symmetric decay two photons are in the calorimeter and produce two cluster events. Since, the two clusters events in true calorimeter time window are more likely to be  $\pi_0$  events, they can easily be removed from the data.

As the  $\pi_0$  decay becomes more asymmetric, a substantial fraction of the  $\pi_0$  energy is taken by one of the two photons. Therefore, it mimics a DVCS photon in the calorimeter. Furthermore, the  $2^{nd}$  photon falls outside the calorimeter acceptance. This source of  $\pi_0$  contamination needs to be subtracted from the data.

The subtraction procedure can be summarized as:

- Kinematics of detected (two clusters events in calorimeter)  $\pi_0$  is computed.
- For each selected  $\pi_0$ , its decay is randomized for such that sample  $\cos\theta$  (the angle between the boost direction and high energy photon) randomly generated between  $[-1,1]$  for big number of times ( $\sim 5000$ )
- The ratio of two-clusters/one-cluster events of this simulation is computed.

This procedure is repeated for each detected  $\pi_0$  in the calorimeter. The resulting events are analyzed for energy background subtraction (results can be seen Fig. (63) and missing mass squared subtraction which will be discussed in VII.5.4

#### VII.5.4 Missing Mass Squared Study

In the  $H(e, e'\gamma)X$  reaction, we construct the missing mass from the Lorentz invariant quantity:

$$\begin{aligned}
 M_X^2 &= (q + p - q')_\mu^2 = (k - k' + p - q')_\mu^2 \\
 &= (q + p)^2 - 2q' \cdot (q + p) + 0 \\
 &= W^2 - 2q'_0[M + \nu - |q| \cos\theta_{\gamma\gamma}]
 \end{aligned} \tag{110}$$

where the virtual photon four momentum vector  $q_\mu = (\nu, q)$  and target proton four-momentum vector  $p_\mu^{lab} = (M, 0)$ .



In exclusive kinematics (neglecting bremsstrahlung),  $M_X^2 = M^2$ , and we can solve for the DVCS photon energy, given its polar angle  $\theta_{\gamma\gamma}$  relative to  $\mathbf{q}$ :

$$\begin{aligned}
 M^2 &= W^2 - 2q'_0[M + \nu - |q| \cos \theta_{\gamma\gamma}] \\
 q'_0 &= \frac{W^2 - M^2}{2[M + \nu - |q| \cos \theta_{\gamma\gamma}]} \\
 Q^2 &= -q_\mu^2 = q^2 - \nu^2 \\
 W^2 &= M^2 + 2M\nu - Q^2
 \end{aligned} \tag{111}$$

### $M_X^2$ Distributions

In this analysis there are three different sets of missing mass squared distributions:

- Double Coincidence  $H(e, e'\gamma)X$  : Using the electron and photon coincidence events, the missing mass squared distribution is constructed with the requirement that the predicted exclusive proton points to the core region of the proton array.
- Triple Coincidence  $H(e, e'\gamma p)$  group-of-nine: By looking for the maximum energy deposited in group-of-nine blocks with the requirement that prediction is in the core region of the proton array while the surrounding eight block can be out side of the core region (see Fig. 62).
- Triple Coincidence  $H(e, e'\gamma p)$ :the detected proton array signal is in the predicted exclusive  $H(e, e'\gamma p)$  block.

Previously discussed background and  $\pi_0$  events which remain after a  $M_X^2$  cut at  $(M_p + m_{\pi^0})^2$  can be removed by event by event subtraction. The notation of these events will be as:

- Calorimeter accidental events =  $N_{calo}^{acc}$ ,
- Proton array accidental events =  $N_{pa}^{acc}$ ,
- Electroproduction of  $\pi_0 = N^{\pi_0}$ .

The result of this initial iteration to the  $M_X^2$  distributions can be seen in:

- Double coincidence, Fig. (65):

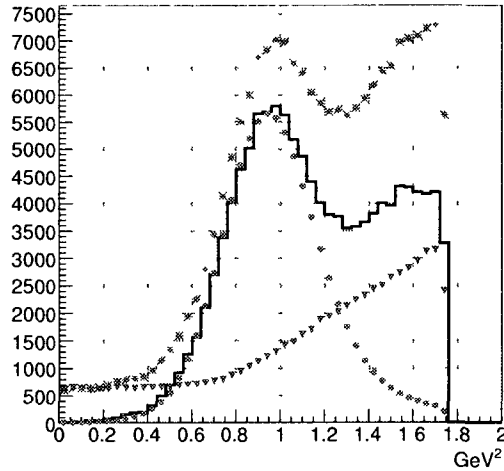


FIG. 65: Missing mass squared ( $M_X^2$ ) for  $H(e, e'\gamma)X$  events. The  $M_X^2$  denoted by star is the distribution which has no subtraction. The  $M_X^2$  denoted by triangle corresponds to the  $N_{calo}^{acc} + N^{\pi_0}$  events. The solid line is obtained from star distribution by subtracting the triangle distribution. The solid circle plot is obtained by Monte Carlo Simulation normalized to the same maximum value as the solid line.

- The  $M_X^2$  spectrum displayed by star has a left tail which becomes zero in the solid spectrum which means that these events are calorimeter accidental events. The achievement can be observed for the right tail of the same spectrum since the  $M_X^2$  constructed from the coincidence of electron and photon events inclusive events are still in this range. However, implementing the proposed  $M_X^2$  cut on this spectrum removes the inclusive events' contribution.
- Triple Coincidence for group-of-nine, Fig. (66):
  - The  $M_X^2$  spectrum resolution is improved with the subtraction of  $N_{pa}^{acc} + N^{\pi_0}$  from the star spectrum.
- Triple Coincidence for exclusive predicted block is the central block of group-of-nine, Fig. (67):
  - The  $M_X^2$  spectrum resolution is improved with the subtraction of  $N_{pa}^{acc} + N^{\pi_0}$  from the star spectrum.

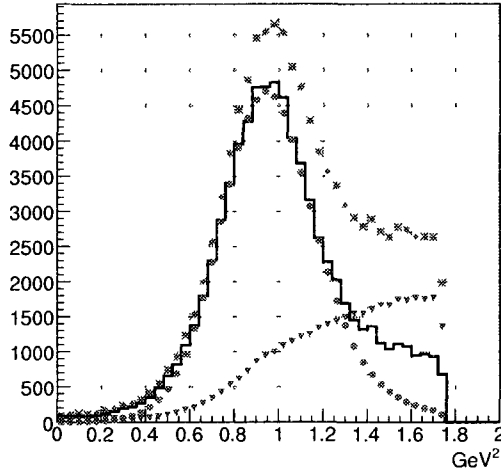


FIG. 66: Missing mass squared distribution of  $H(e, e'\gamma p)$  events for the group-of-nine selection. The  $M_X^2$  denoted by star is the distribution which has no subtraction. The  $M_X^2$  denoted by triangle corresponds to the  $N_{pa}^{acc} + N_{\pi^0}$  events. The solid line is obtained from star distribution by subtracting the triangle distribution. The solid circle plot is obtained by Monte Carlo Simulation normalized to the same maximum value as the solid line.

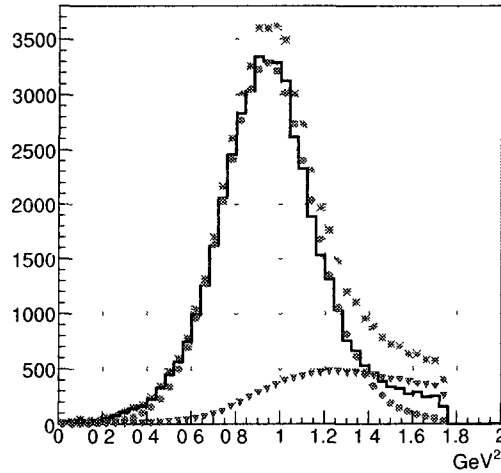


FIG. 67: Missing mass squared distribution of  $H(e, e'\gamma p)$  events with detected proton in the exclusive predicted block. The  $M_X^2$  denoted by star is the distribution which has no subtraction. The  $M_X^2$  denoted by triangle corresponds to the  $N_{pa}^{acc} + N_{\pi^0}$  events. The solid line is obtained from star distribution by subtracting the triangle distribution. The solid circle plot is obtained by Monte Carlo Simulation normalized to the same maximum value as the solid line.

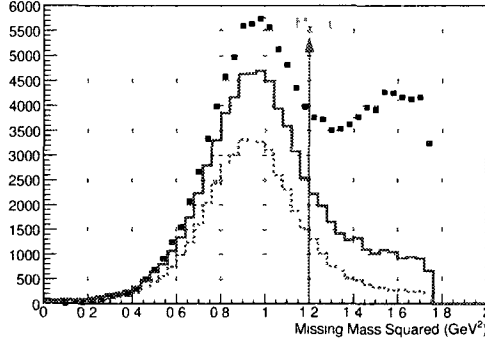


FIG. 68: The square  $M_X^2$  spectrum is the  $H(e, e'\gamma)X$  events after the subtraction of  $N_{calo}^{acc} + N^{\pi^0}$ . The solid line  $M_X^2$  spectrum is the  $H(e, e'\gamma p)$  events for the group-of-nine and after the subtraction of  $N_{pa}^{acc} + N^{\pi^0}$ . The dashed line  $M_X^2$  spectrum is the  $H(e, e'\gamma p)$  events with events with detected proton in the exclusive predicted block and after the subtraction of  $N_{pa}^{acc} + N^{\pi^0}$ .

The  $M_X^2$  spectrum of double coincidence and two exclusive sets can be compared in Fig. 68. As a matter of fact all three sets are in good agreement. However, the proceeding of this  $M_X^2$  study, which is binning the  $M_X^2$  spectrum of Fig. (68) in azimuth, introduces a systematic variation in the statistics, peak positions and the widths of the  $M_X^2$  spectrum with respect to block position in proton array (azimuthal angle).

Each histogram in Fig. (69) constitutes two neighbor blocks in the core region of proton array. The variation in statistics is obvious, however, most importantly the variation in peak position and width of the exclusive peak has more physics or experimental information regarding the experimental setup. Therefore, a Gaussian fit is implemented to  $M_X^2$  spectrum of  $H(e, e'\gamma p)$  events with the requirement of exclusive predicted block to be the central block in group-of-nine. The exclusive peak is fitted in the range of  $[0.2, 1.2] GeV^2$ . The Gaussian mean of the exclusive peak,  $\langle M_X^2 \rangle_G$ , and Gaussian width,  $\sigma(M_X^2)$ , extracted from the fit parameters which are plotted as a function of  $\phi_{pa}$  in Figs.(70), (71).

The mean position of the exclusive peak for the Monte Carlo Simulation is the left hand side graph in Fig. (70). The  $\langle M_X^2 \rangle_G$  is stable around a value of  $0.94 GeV^2$  for the inner ring. On the other hand, the middle ring and the outer ring values have a variation with the change in  $\phi_{pa}$ .

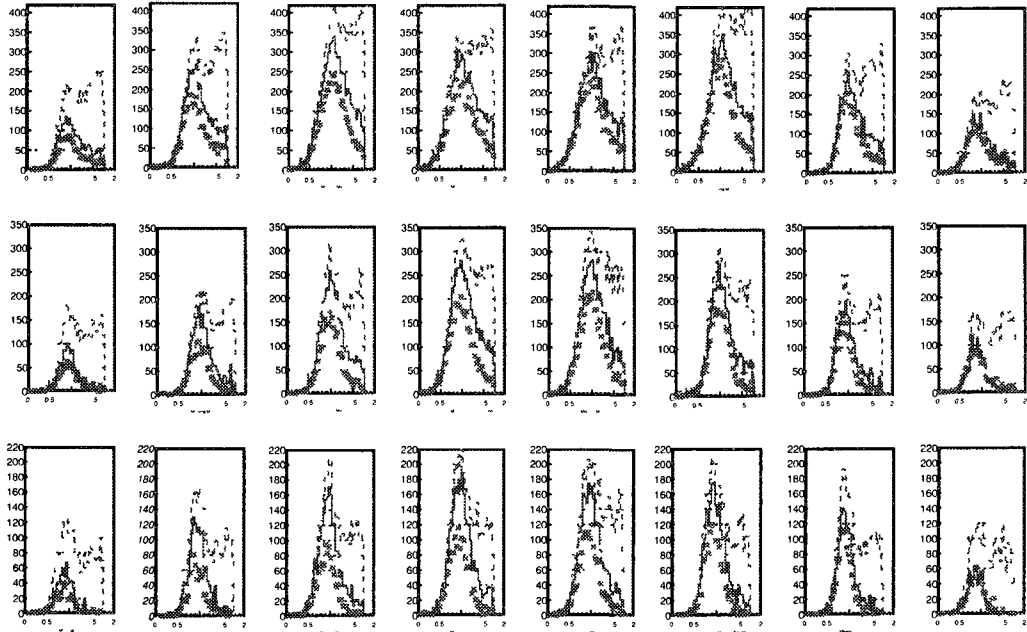


FIG. 69: The displayed spectrum is the  $M_X^2$  spectrum in Fig. 68 but binned in azimuth. The dashed  $M_X^2$  spectrum is the  $H(e, e'\gamma)X$  events after the subtraction of  $N_{calo}^{acc} + N^{\pi_0}$ . The solid  $M_X^2$  spectrum is the  $H(e, e'\gamma p)$  events for the group-of-nine and after the subtraction of  $N_{pa}^{acc} + N^{\pi_0}$ . The star  $M_X^2$  spectrum is the  $H(e, e'\gamma p)$  events with exclusive predicted block is the central block of group-of-nine requirement and after the subtraction of  $N_{pa}^{acc} + N^{\pi_0}$ . In this configuration, azimuthal angle increases from right to left, polar angle increases from bottom to top and each histogram constitutes two proton array blocks in core region.

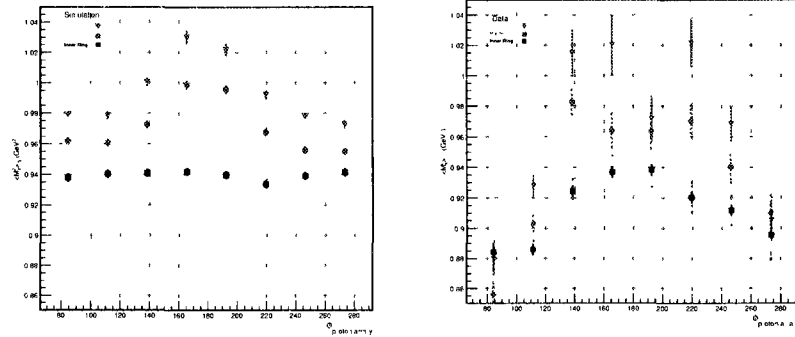


FIG. 70: The mean of the Gaussian fit of the  $M_X^2$  spectra of  $H(e, e'\gamma p)$  events for the proton detected in the exclusive predicted block. The left (right) spectra corresponds to simulation (data). The simulation mean values are stable relative to data. The variation in simulation mean values show consistent trend for the middle and outer ring. However, the variation in data mean values for all rings show inconsistent trend.

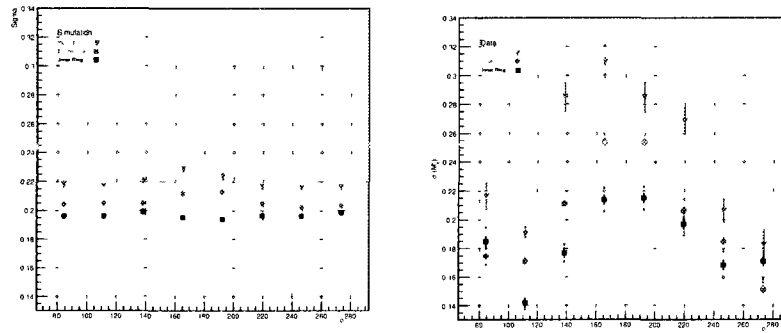


FIG. 71: The width of Gaussian fit ( $\sigma(M_X^2)$ ) of the  $M_X^2$  spectra of  $H(e, e'\gamma p)$  events for the proton detected in the exclusive predicted block. The left (right) spectra corresponds to simulation (data). The variation in these spectra shows inconsistent trend so much so that some blocks have smaller  $\sigma(M_X^2)$  than simulation

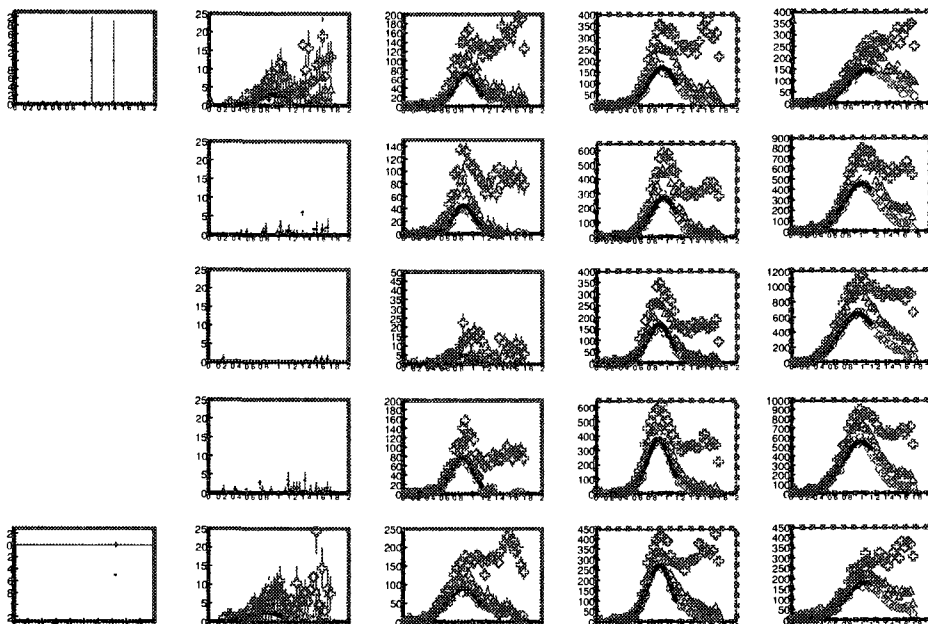


FIG. 72:  $M_X^2$  spectra in electromagnetic calorimeter. Each histogram constitutes four calorimeter blocks. The histogram with dashed line frame correspond to the dashed line region, and the histogram with solid lines correspond to the fine dashed line region of the calorimeter shown in Fig.(58)

The data  $\langle M_X^2 \rangle_G$  values, the right plot in Fig. (70), have a big variation as a function of  $\phi_{pa}$ . Although, the data inner ring pattern is similar to the outer and middle rings of the simulation, the behavior of proton array can not be properly understood from this information.

Moreover, the large discrepancy in between the simulation and data Gaussian widths in Fig. (71) entailed to scrutinize the  $M_X^2$  distribution in calorimeter.

## VII.6 $M_X^2$ IN ELECTROMAGNETIC CALORIMETER

The electromagnetic calorimeter response dominates the  $M_X^2$  distributions. Therefore, in order to better understand the proton array behavior (Figs. (70) and (71)), the  $H(e, e'\gamma)X$  and  $H(e, e'\gamma p)$  events  $M_X^2$  spectrum is studied in different calorimeter geometrical cut. The first geometrical cut is discussed in VII.4.2 and the geometrical boundaries are set as

$$-15cm < x_{calo} < 12cm,$$

$$-15cm < y_{calo} < 15cm. \quad (112)$$

Each calorimeter block dominates different region in proton array (details can be seen in Fig. (38)). As a consequence, calorimeter blocks grouped in four (58) and the  $M_X^2$  spectrum is checked for all calorimeter blocks. The corresponding spectra are displayed in Fig. (72). The proton array limits the calorimeter acceptance for triple coincidence events which can be seen in Fig. (72). The blocks in the far edge away from the beam line, have no events for the  $H(e, e'\gamma)p$  (where  $p$  projected to be in the core region of PA) or  $H(e, e'\gamma p)$  events, as a result of the proton array geometry. Moreover, statistics increase as the photon approaches the beam line. The intermediate conclusion is that proton array acceptance dominated the distribution of statistics block-by-block in the electromagnetic calorimeter. The  $M_X^2$  spectra evince that the exclusive peak position, the width of the exclusive peak, and statistics vary as a function of calorimeter block position. Therefore, to be able understand how proton array dominates the calorimeter, block-by-block variation of  $M_X^2$  spectrum is examined for the calorimeter blocks in the last four columns within the geometrical region shown in Eq. (112) and Fig. (58).

For example, as it can be seen in Fig.(73) the last two column of this region shows good exclusive peak and low statistics. To study the calorimeter response, a Gaussian fit is performed to  $M_X^2$  distribution of  $H(e, e'\gamma p)$   $M_X^2$  events with detected proton in the exclusive predicted block in the approximate range of

$$\begin{aligned} M_p^2 &\leq M_X^2 \leq (M_p + m_\pi)^2 \\ 0.4 &\leq M_X^2 \leq 1.15 GeV^2 \end{aligned} \quad (113)$$

The fitted peak position of the is denoted by  $\langle M_X^2 \rangle_G$  where the subscript  $G$  means result of the Gaussian fit, and I will denote with a superscript *data* or *sim* the position fitted to either the ensemble of data events or simulation events.

#### The Gaussian Mean $\langle M_X^2 \rangle_G$ :

As can be seen in Fig.(74) the trend of  $\langle M_X^2 \rangle_G$  in simulation and data is different. The data  $\langle M_X^2 \rangle_G$  values scattered in the range  $0.82 GeV^2$  to  $1.18 GeV^2$ . For the first two columns, the data values are shifted to smaller values than  $0.88 GeV^2$  whereas simulation values are stable around  $0.94 GeV^2$ . Although the simulation  $\langle M_X^2 \rangle_G$  values shows a stable trend, an interesting trend can be observed for the blocks corresponding to the top and bottom rows.



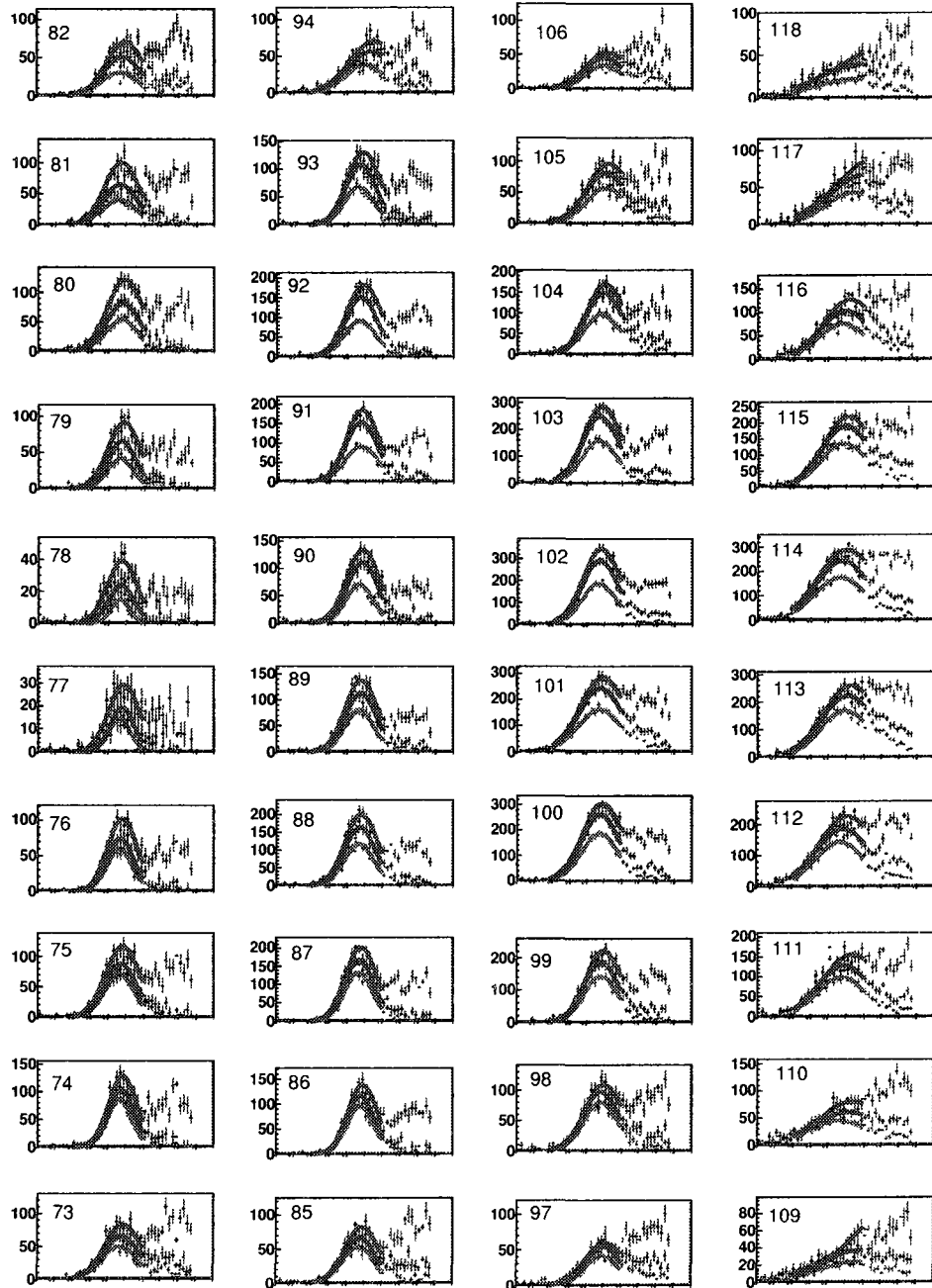


FIG. 73:  $M_X^2$  distribution in individual calorimeter blocks. These blocks correspond to the dashed line region in the calorimeter shown in Fig. 58.

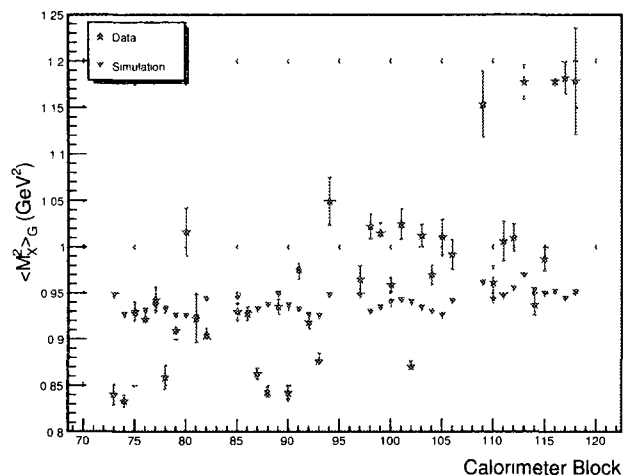


FIG. 74: The Gaussian fit peak,  $\langle M_X^2 \rangle_G$ , position before the re-calibration as a function of calorimeter block. The calorimeter blocks in this plot correspond to the dashed line region in calorimeter shown Fig. (58).

### The Gaussian RMS Width $\sigma(M_X^2)$

The  $\sigma(M_X^2)$  values displayed as a function of calorimeter block number in Fig. (75). The simulation values are stable around a  $\sigma(M_X^2)$  value of 0.19. However, there are significant number of blocks in the left two columns with narrower  $\sigma(M_X^2)$  data values than the simulation and third column data values are in relative agreement in simulation. As a result of the pile up, the last column data  $\sigma(M_X^2)$  values are scattered in between the range of 0.21 to 0.33

## VII.7 RE-CALIBRATION

The initial calibration of the calorimeter may have been done under conditions of different background noise in the calorimeter. Noise (e.g. from random  $\pi_0 \rightarrow \gamma\gamma$  decay) can affect both the the Gaussian width of the  $M_X^2$  distribution, and the peak position. In the present procedure, the shower distribution in the calorimeter is not re-examined. It is assumed that the full shower energy is associated with a single block. In particular, the reconstruction of the shower position in the block is not re-considered. Thus our reconstruction of the  $\pi_0$  mass will not necessarily be improved by the re-calibration.

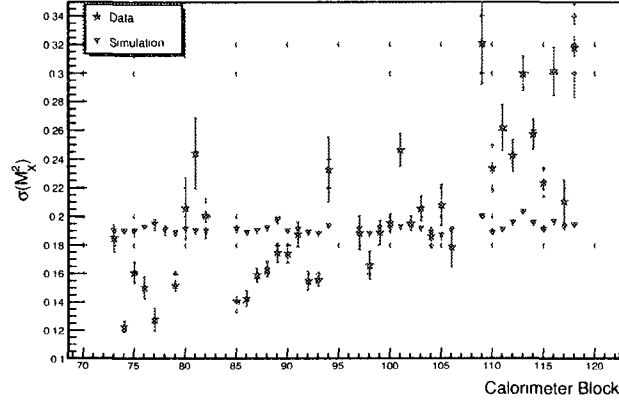


FIG. 75: The Gaussian width  $\sigma(M_X^2)$  for  $M_X^2$  distribution as a function of calorimeter block. The calorimeter blocks in this plot correspond to the dashed line region in calorimeter shown Fig. (58).

### VII.7.1 Re-Normalization Factor

For each block  $j$  a multiplicative re-calibration constant  $\alpha_j$  is sought such that the fitted mean  $\langle M_X^2(\alpha_j) \rangle$  approximate to a predetermined value of  $(M_X^2)_{ref}$ . Because of the simulation results, the predetermined value is set for  $(M_X^2)_{ref} = 0.94 \text{ GeV}^2$  rather than  $M_{proton}^2$ . The re-normalization factor is derived as follows:

$$\begin{aligned}
 M_X^2 &= (q + p - q')_\mu^2 = (k - k' + p - q')_\mu^2 \\
 &= (q + p)^2 - 2q' \cdot (q + p) + 0 \\
 &= W^2 - 2q'_0 [M_\nu - |q| \cos \theta_{\gamma\gamma}]
 \end{aligned} \tag{114}$$

$$\langle M_X^2 \rangle_{ref} \approx \langle M_X^2(\alpha_j) \rangle_G^{sim, data}, \tag{115}$$

where  $G$  subscript denotes the mean value of Gaussian fit. Then, re-writing the Eq. (114) with  $q'_0 \rightarrow \alpha q'$  by applying Eq.(115):

$$\begin{aligned}
 \langle M_X^2 \rangle_{ref} &= \langle W^2 - 2q'_0 \alpha_j [M_\nu - |q| \cos \theta_{\gamma\gamma}] \rangle_G^{sim, data} \\
 &= \alpha_j^{sim, data} \langle W^2 - 2q'_0 [M_\nu - |q| \cos \theta_{\gamma\gamma}] \rangle_G^{sim, data} \\
 &\quad + (1 - \alpha_j^{sim, data}) \langle W^2 \rangle^{sim, data} \\
 &= \alpha_j \langle M_X^2 \rangle_G^{sim, data} + (1 - \alpha_j) \langle W^2 \rangle^{sim, data}.
 \end{aligned} \tag{116}$$

Finally, the global normalization factor written as

$$\alpha_j^{sim, data} = \frac{\langle W^2 \rangle^{sim, data} - \langle M_X^2 \rangle_{ref}}{\langle W^2 \rangle^{sim, data} - \langle M_X^2 \rangle_G^{sim, data}} \quad (117)$$

### Data Re-Normalization Factor

The difference between the simulation and data re-normalization factors is that we dilute the data re-normalization factor with the error in each Gaussian mean ( $\langle M_X^2 \rangle_G^{data}$ ). Using the Eq. (117) the normalization coefficient for data can be written as

$$\alpha_j^{data} = \frac{\langle W^2 \rangle^{data} - \langle M_X^2(\alpha_j) \rangle_G^{data}}{\langle W^2 \rangle^{data} - \langle M_X^2 \rangle_G^{data}}. \quad (118)$$

Then a new variable, dilution factor is introduced as

$$\tilde{\Delta} = \langle M_X^2 \rangle_G^{data} - 0.94 \text{ GeV}^2, \quad (119)$$

where  $0.94 \text{ GeV}^2 = \langle M_X^2 \rangle_{ref}$ . By using the Eq. (118) and Eq. (119), the diluted normalization factor becomes

$$\begin{aligned} \alpha_j^{data} &= \frac{\langle W^2 \rangle^{data} - \langle M_X^2 \rangle_G^{data} + \tilde{\Delta}}{\langle W^2 \rangle^{data} - \langle M_X^2 \rangle_G^{data}}. \\ \alpha_j^{data} &= 1 + \frac{\tilde{\Delta}}{\langle W^2 \rangle^{data} - \langle M_X^2 \rangle_G^{data}} \end{aligned} \quad (120)$$

### Dilution of $\alpha_j$ with Error Bars ( $\sigma(\langle M_X^2 \rangle_G^{data})$ )

The dilution of the re-normalization factor is done according to error bars on the mean  $\sigma(\langle M_X^2 \rangle_G^{data})$  of each  $\langle M_X^2 \rangle_G^{data}$  value. Please note that  $\sigma(\langle M_X^2 \rangle_G^{data}) \neq \sigma(M_X^2)$ . The Eq. (120) can be written as

$$\alpha_j = 1 + \delta_j,$$

where

$$\delta_j = \frac{\tilde{\Delta}}{\langle W^2 \rangle^{data} - \langle M_X^2 \rangle_G^{data}}. \quad (121)$$

Finally, by comparing the  $|\tilde{\Delta}|$  with  $\sigma(\langle M_X^2 \rangle_G^{data})$  the way how the dilution will be implemented is chosen:

- if  $|\tilde{\Delta}| < \sigma(\langle M_X^2 \rangle_G^{data})$  then  $\tilde{\Delta} \rightarrow 0$ ,
- if  $\tilde{\Delta} > \sigma(\langle M_X^2 \rangle_G^{data})$  then  $\tilde{\Delta} \rightarrow \tilde{\Delta} - \sigma(\langle M_X^2 \rangle_G^{data})$ ,
- if  $\tilde{\Delta} < (-)\sigma(\langle M_X^2 \rangle_G^{data})$  then  $\tilde{\Delta} \rightarrow \tilde{\Delta} + \sigma(\langle M_X^2 \rangle_G^{data})$ .

## VII.7.2 Re-Normalization

In the remaining part of the text, re-normalization factor  $\alpha_j^{sim, data}$  is represented as  $RN_{j,i}^{sim, data}$ .

### Simulation

As discussed earlier not all blocks show discrepancy with respect to predetermined  $M_X^2$  value of  $0.94 \text{ GeV}^2$ . Therefore, the performed re-normalization is a block-by-block re-normalization of the simulation photon energy. The re-normalization factor for this iteration can be written as

$$RN_{j,1}^{sim} = \frac{\langle W^2 \rangle^{sim} - 0.94 \text{ GeV}^2}{\langle W^2 \rangle^{sim} - \langle M_X^2 \rangle_G^{sim}} \quad (122)$$

The denominator consists of two constants:

- The data ensemble average value of  $W^2$  is  $\langle W^2 \rangle^{sim} = 4.83 \text{ GeV}^2$

The re-normalization implemented as

$$q'_{norm} = RN_{j,1} \cdot q'. \quad (123)$$

### Data: First Re-Normalization

The first re-normalization is implemented based on the  $\sigma(\langle M_X^2 \rangle_G^{data})$  values extracted from the errors on each Gaussian mean  $\langle M_X^2 \rangle_G^{data}$  displayed in Fig. (74). Thus re-normalization factors used in first re-normalization are either

$$RN_{j,1} = 1 + \frac{\tilde{\Delta} - \sigma(\langle M_X^2 \rangle_G^{data})}{\langle W^2 \rangle^{data} - \langle M_X^2 \rangle_G^{data}}, \quad (124)$$

where  $\tilde{\Delta} > \sigma(\langle M_X^2 \rangle_G^{data})$  or

$$RN_{j,1} = 1 + \frac{\tilde{\Delta} + \sigma(\langle M_X^2 \rangle_G^{data})}{\langle W^2 \rangle^{data} - \langle M_X^2 \rangle_G^{data}}, \quad (125)$$

where  $\tilde{\Delta} < (-)\sigma(\langle M_X^2 \rangle_G^{data})$ . Similar to the simulation, the photon energy is re-normalized by

$$q'_{norm}(j) = RN_{j,1} \cdot q'. \quad (126)$$

### Data: Second Re-Normalization

The displayed results of the first re-normalization to the simulation and data can be seen in Fig. (76). Simulation Gaussian mean values become stable around the pre-determined value, however, data Gaussian mean values are still show discrepancies. Therefore, I decided to iterate the data one more time by another renormalization. The second re-normalization factors are calculated as the first one except that the new dilution factor of 0.5 to the extracted  $\sigma(\langle M_X^2 \rangle_G^{data})$ . Thus, if  $\tilde{\Delta} > (0.5) \cdot \sigma(\langle M_X^2 \rangle_G^{data})$  the re-normalization factor is

$$RN_{j,2} = 1 + \frac{\tilde{\Delta} - (0.5) \cdot \sigma(\langle M_X^2 \rangle_G^{data})}{\langle W^2 \rangle^{data} - \langle M_X^2 \rangle_G^{data}}. \quad (127)$$

Or, if  $\tilde{\Delta} < (-0.5) \cdot \sigma(\langle M_X^2 \rangle_G^{data})$  the re-normalization factor is

$$RN_{j,2} = 1 + \frac{\tilde{\Delta} + (0.5) \cdot \sigma(\langle M_X^2 \rangle_G^{data})}{\langle W^2 \rangle^{data} - \langle M_X^2 \rangle_G^{data}}. \quad (128)$$

This final iteration to the data implemented by

$$q'_{nom}(j) = RN_{j,1} \cdot RN_{j,2} \cdot q'. \quad (129)$$

### Numerical Stability

In Kinematics 3, the central HRS value of  $W^2$  is

$$W^2 = M^2 + Q^2 \left( \frac{1}{x_B} - 1 \right) = 4.97 GeV^2. \quad (130)$$

In the fits of this study (Fig. (73)) to data,

$$\left| \langle M_X^2 \rangle_G^{data} - M^2 \right| \leq 0.2 GeV^2 \quad (131)$$

The choice of definition of  $\langle W^2 \rangle$  will likely affect the re-normalization by 5 to 10% of the correction  $\delta_j$ . After all, The ensemble average value of  $W^2$ ,  $\langle W^2 \rangle^{data} = 4.972 GeV^2$  is used.

### VII.7.3 Smearing

The discrepancy between the data and simulation  $\sigma(M_X^2)$  values varies block-by-block (Fig.(75)). Therefore, a random Gaussian block-by-block smearing is implemented to the simulation until the one- $\sigma$  Gaussian widths fitted to the  $M_X^2$  distributions of the simulation agree with corresponding widths fitted to the data.

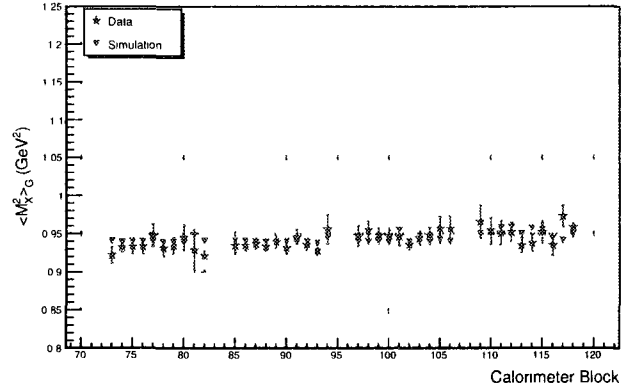


FIG. 76: The Gaussian fit peak position for  $M_X^2$  distribution after all iterations as a function of calorimeter block. The calorimeter blocks in this plot correspond to the dashed line region in calorimeter shown Fig. (58).

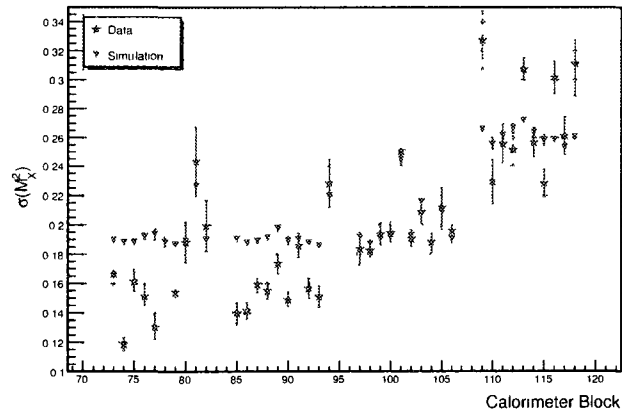


FIG. 77: The Gaussian width  $\sigma(M_X^2)$  for  $M_X^2$  distribution after all iterations as a function of calorimeter block. The calorimeter blocks in this plot correspond to the dashed line region in calorimeter shown Fig. (58).

Smearing is implemented with a width defined as a fraction of the photon energy. The fixed fractional width

$$q'_{sim} \leftarrow q'_{rms.sim}[1 + P_{Gaus}(0, \sigma_j)] \quad (132)$$

where  $P(\mu, \sigma)$  is a Gaussian distribution of mean  $\mu$  and rms  $\sigma$ .

The photon energy resolution has the same impact (Eq. 116, 117) as the photon energy calibration on the missing mass squared distribution. Using the Gaussian rms width (75) fitted to the  $M_X^2$  distribution for block- $j$  one can write

$$\Delta\sigma_j = \sqrt{(\sigma^2(M_X^2)_j^{data} - \sigma^2(M_X^2)_j^{sim})} \quad (133)$$

Using the fix fraction smearing of Eq. 132, the rms smearing to implement block-by-block to the simulation is;

$$\sigma_j = \frac{\Delta\sigma_j}{\langle W^2 \rangle^{sim} - \langle M_X^2 \rangle_{ref}} \quad (134)$$

where the ensemble average  $\langle W^2 \rangle^{sim} = 4.83 \text{ GeV}^2$ . The results of the smearing to simulation can be seen in Fig. (76) and Fig. (77).



## CHAPTER VIII

### RESULTS AND DISCUSSION

#### VIII.1 RESULTS

The triple coincidence Beam Spin Asymmetry measurement in the deeply virtual electro-production of a real photon on the proton is studied using a longitudinally polarized electron beam at  $E = 5.75\text{GeV}$  with the kinematics 3 shown in Tab.1. In II.5.3 the extraction of BSA shown by Eq. (61) is performed as

$$BSA_{LU} = \frac{N_{proton}^+ - N_{proton}^-}{N_{proton}^+ + N_{proton}^-} \quad (135)$$

where  $(N_{proton}^+)$  is the positive helicity number of true counts and  $(N_{proton}^-)$  is the negative helicity number of true counts Here, the true events are the events after all  $N_{pa}^{acc}$ ,  $N_{calo}^{acc}$ ,  $N_{\pi_0}$  events are subtracted from the raw counts in the missing mass squared distribution range of

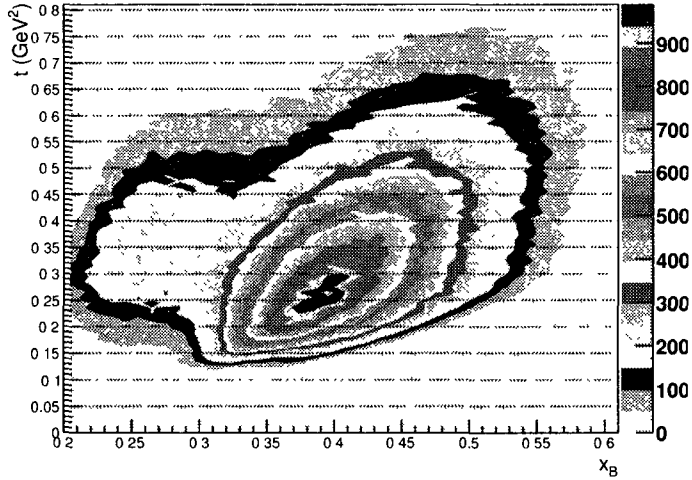
$$0.4 < M_X^2 < 1.2 \text{ GeV}^2 \quad (136)$$

for the following event  $M_X^2$  distributions:

- Double Coincidence  $H(e, e'\gamma)X$  : Using the electron and photon coincidence events, the missing mass squared distribution is constructed with the requirement that the predicted exclusive proton points the core region of the proton array.
- Triple Coincidence  $H(e, e'\gamma p)$  group-of-nine: By looking for the maximum energy deposited in group-of-nine blocks with the requirement that prediction is in the core region of the proton array while the surrounding eight block can be out side of the core region (see Fig. 62).
- Triple Coincidence  $H(e, e'\gamma p)$ :the detected proton array signal is in the predicted exclusive  $H(e, e'\gamma p)$  block.

The implemented bins are;

- 24 bins in azimuthal angle,  $\phi_{\gamma\gamma} \in [0, 2\pi]$ ,
- 5 bins in  $t_{min} - t \in [0.0, 0.25]$ .

FIG. 78:  $t$  dependence on  $x_B$ 

The BSA's azimuthal dependence is extracted in these 24 bins of  $\phi_{\gamma\gamma}$  which ultimately entail extraction of  $\sin\phi$  and  $\sin 2\phi$  structure. In the exclusive kinematics, the invariant moment transfer  $t$  and  $t_{min}$  relies on the positions of the reconstructed photons. Thus, the resolution in invariant moment transfer is better than any other electromagnetic calorimeter parameters.

The binning in  $t_{min} - t$  allows to examine the dependence of Fourier coefficients, in Eq. (57), (58) and (59), on scaling variables and transverse momentum transfer.  $t_{min}$  can be expressed as

$$t_{min} = \frac{-M_p^2 x_B^2}{1 - x_B + x_B M^2 / Q^2} \quad (137)$$

and the square of the transverse momentum transfer is given by

$$\Delta_{\perp}^2 \approx (t_{min} - t)(1 - \xi^2) \quad (138)$$

The extracted BSA results are displayed

- $t_{min} - t = [0.00, 0.05] \text{ GeV}^2$  Fig. (81)
- $t_{min} - t = [0.05, 0.10] \text{ GeV}^2$  Fig. (82)

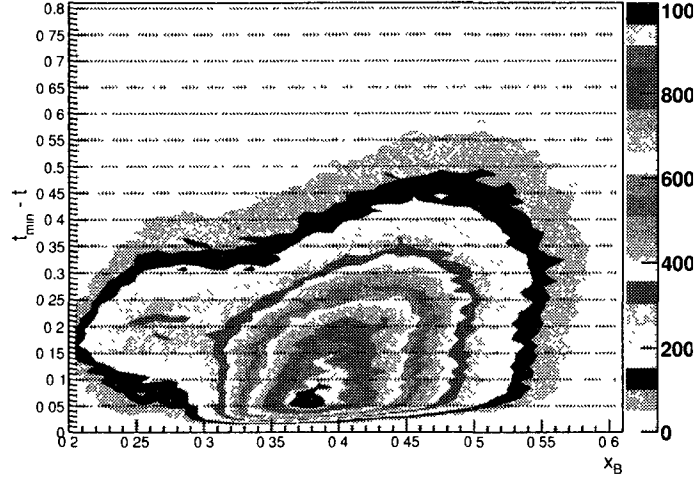


FIG. 79:  $t_{min} - t$  dependence on  $x_B$

- $t_{min} - t = [0.10, 0.15] \text{ GeV}^2$  Fig. (83)
- $t_{min} - t = [0.15, 0.20] \text{ GeV}^2$  Fig. (84)
- $t_{min} - t = [0.20, 0.25] \text{ GeV}^2$  Fig. (85)

## VIII.2 DISCUSSION

The BSA results are presented in bins of  $t_{min} - t$  rather than  $t$  because of the fact that  $t_{min}$  is correlated with  $x_B$  which is expressed in Eq.(137) and displayed in Fig.(78, 79). Moreover, as it is expressed in Eq. (138)  $\Delta_{perp}$ , the most significant physical interpretation of GPDs depends on  $t_{min} - t$ . The azimuthal dependence of the BSA is used to extract the BSA for the kinematics-3 of Table-1. In order to do so, the asymmetry dependence on azimuth was fitted with the function:

$$BSA_{fit}(\phi) = \frac{\alpha \sin \phi}{1 + \beta \cos \phi}. \quad (139)$$

The extracted BSA amplitudes by using the Eq. (139) are:

- $H(e, e'\gamma p)$  events with detected proton in the exclusive predicted block in Table-4,

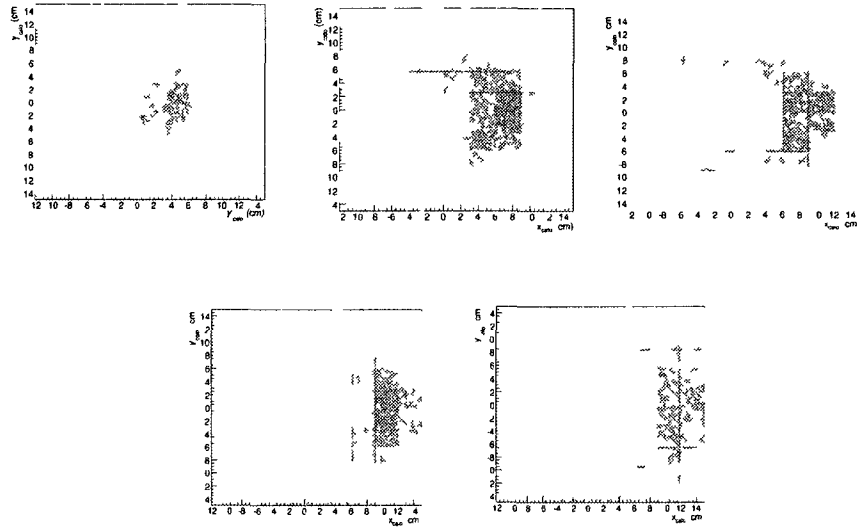


FIG 80 The projection of  $t_{min} - t$  on the surface of the calorimeter with the missing mass squared range of  $0.4 < M_X^2 < 1.2 \text{ GeV}^2$ . From left to right corresponding  $t_{min} - t$  intervals of  $[0, 0.05]$ ,  $[0.05, 0.1]$ ,  $[0.1, 0.15]$ ,  $[0.15, 0.2]$ ,  $[0.2, 0.25] \text{ GeV}^2$ .

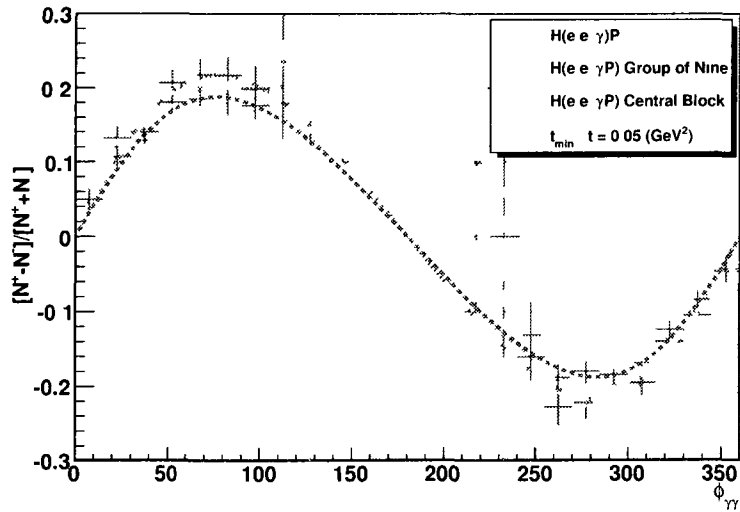


FIG 81 Beam Spin Asymmetry measurement for the  $t_{min} - t$  bin interval of  $[0.00, 0.05] \text{ GeV}^2$  which corresponds to the central region of the calorimeter (Fig 80).

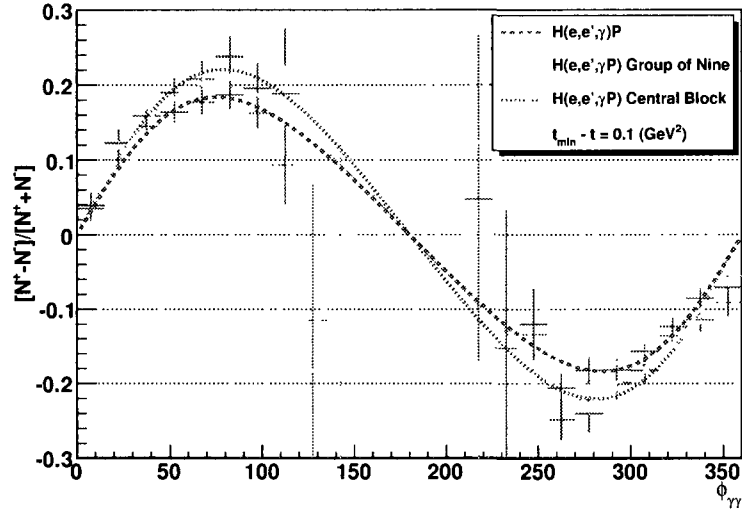


FIG. 82: Beam Spin Asymmetry measurement for the  $t_{min} - t$  bin interval of  $[0.05, 0.10] \text{ GeV}^2$ . Corresponding calorimeter region to bin interval, can be seen in Fig.(80).

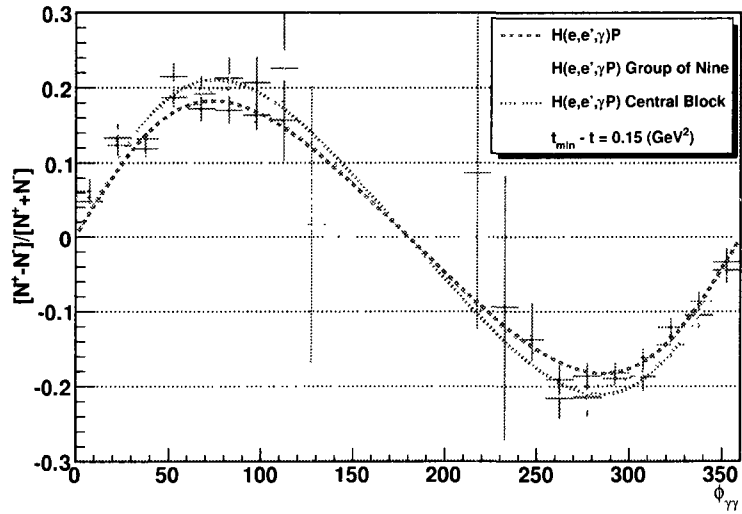


FIG. 83: Beam Spin Asymmetry measurement for the  $t_{min} - t$  bin interval of  $[0.10, 0.15] \text{ GeV}^2$ . Corresponding calorimeter region to bin interval, can be seen in Fig.(80).

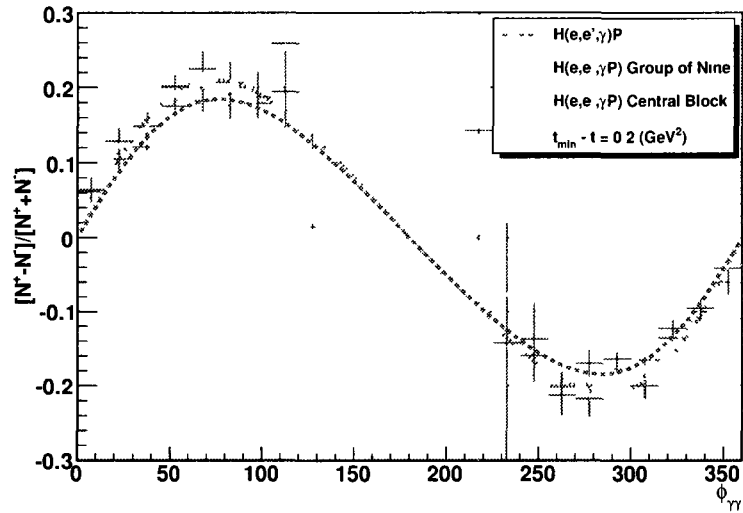


FIG. 84: Beam Spin Asymmetry measurement for the  $t_{\min} - t$  bin interval of  $[0.15, 0.20] \text{ GeV}^2$ . Corresponding calorimeter region to bin interval, can be seen in Fig.(80).

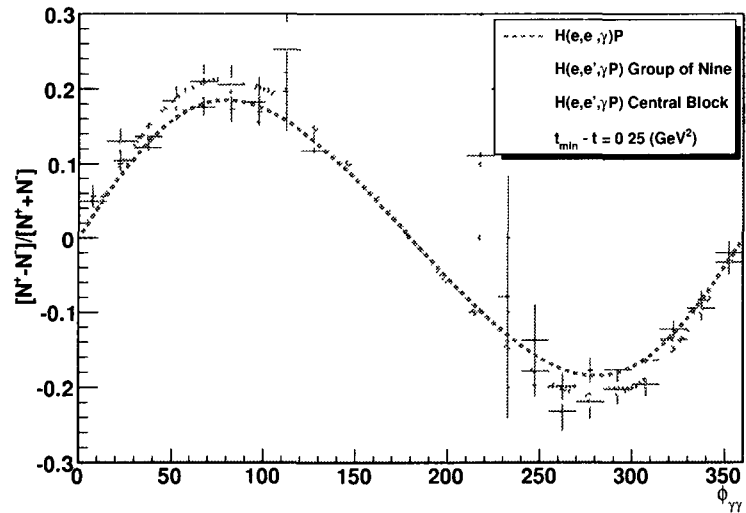


FIG. 85. Beam Spin Asymmetry measurement for the  $t_{\min} - t$   $[0.20, 0.25] \text{ GeV}^2$ . Corresponding calorimeter region to bin interval, can be seen in Fig (80).

- $H(e, e'\gamma p)$  events in the group of nine in Table-5,
- $H(e, e'\gamma)X$  events with the proton prediction in core region of proton array in Table- 6,

which listed for all bins in  $t_{min} - t$ . In the Fig. 86, the amplitudes of the asymmetries are displayed as a function of  $t_{min} - t$  bin for all sets of  $M_X^2$ .

The main objective of triple coincidence analysis is to check the exclusivity in the double coincidence data by comparing the  $H(e, e'\gamma p)$  events in the group of nine in the proton array and  $H(e, e'\gamma)X$  events with the proton prediction in core region of proton array. Deviation for each  $t_{min} - t$  is displayed in Fig. (87). The average deviation of triple coincidence BSA measurements from the double coincidence ones is  $1.3 \sigma$ . On the other hand, the variations in the asymmetry values of compared event sets have the same trend (the up and down triangles in Fig.(86) except the bin 2, all BSA measurements have the same variation). Moreover, the more exclusive cut is applied, the higher the BSA measurement. Furthermore, it is discussed that the  $M_X^2$ , which correlates with BSA measurement, spectra varies depending on the calorimeter block. In this regard, the projection of  $t_{min} - t$  on the surface of the calorimeter is displayed in Fig. (80). As it can be seen that, each  $t_{min} - t$  bin interval corresponds to the different blocks in the calorimeter. The consequence of this variation can be seen in Fig. (87) which displays the deviation  $\sigma$  as a function of  $t_{min} - t$ . As it can be seen that the deviation in bins 2 and 3 are less than the average value and these bins correspond to the calorimeter blocks where both the statistics and the resolution of the  $M_X^2$  spectrum are fairly good (see Fig. (73)). Therefore, considering not only BSA measurements but also the presented  $M_X^2$  spectra study confirms the exclusivity of the E00-100 experiment along with the consistent double and triple coincidences.

### VIII.3 VGG CALCULATION OF BSA

As indicated before, the GPDs studies are model dependent. A model calculation is performed based on the most widely used VGG [32, 33] model calculation is performed for the triple coincidence beam spin asymmetry measurement. The VGG model calculations are presented in Figs.(88, 89, 90, 91, and 92 ) for each  $t_{min} - t$  along with the fit to the exclusive triple coincidence data. The presented VGG calculation confirms the amplitude shape of the asymmetry. The shift in the peak

$t_{min} - t$ bin	$\alpha$	$\alpha_{error}$	$\beta$	$\beta_{error}$
[0.00-0.05]	$2.116 \times 10^{-1}$	$1.075 \times 10^{-2}$	$-2.290 \times 10^{-1}$	$7.508 \times 10^{-2}$
[0.05-0.10]	$2.163 \times 10^{-1}$	$1.212 \times 10^{-2}$	$-1.976 \times 10^{-1}$	$8.669 \times 10^{-2}$
[0.10-0.15]	$2.035 \times 10^{-1}$	$1.213 \times 10^{-2}$	$-2.561 \times 10^{-1}$	$8.601 \times 10^{-2}$
[0.15-0.20]	$2.014 \times 10^{-1}$	$1.213 \times 10^{-2}$	$-2.892 \times 10^{-1}$	$8.027 \times 10^{-2}$
[0.20-0.25]	$2.091 \times 10^{-1}$	$1.153 \times 10^{-2}$	$-1.933 \times 10^{-1}$	$8.534 \times 10^{-2}$

TABLE 4: Fit parameters of Eq.(139) for  $H(e, e'\gamma p)$  events with detected proton in the exclusive predicted block.

$t_{min} - t$ bin	$\alpha$	$\alpha_{error}$	$\beta$	$\beta_{error}$
[0.00-0.05]	$1.932 \times 10^{-1}$	$8.172 \times 10^{-3}$	$-2.775 \times 10^{-1}$	$6.018 \times 10^{-2}$
[0.05-0.10]	$1.918 \times 10^{-1}$	$9.230 \times 10^{-3}$	$-2.813 \times 10^{-1}$	$6.845 \times 10^{-2}$
[0.10-0.15]	$1.864 \times 10^{-1}$	$9.172 \times 10^{-3}$	$-3.157 \times 10^{-1}$	$6.697 \times 10^{-2}$
[0.15-0.20]	$1.909 \times 10^{-1}$	$9.065 \times 10^{-3}$	$-2.716 \times 10^{-1}$	$6.898 \times 10^{-2}$
[0.20-0.25]	$1.952 \times 10^{-1}$	$8.774 \times 10^{-3}$	$-2.037 \times 10^{-1}$	$7.062 \times 10^{-2}$

TABLE 5: Fit parameters of Eq.(139) for  $H(e, e'\gamma p)$  events in the group of nine.

$t_{min} - t$ bin	$\alpha$	$\alpha_{error}$	$\beta$	$\beta_{error}$
[0.00-0.05]	$1.825 \times 10^{-1}$	$7.258 \times 10^{-3}$	$-2.338 \times 10^{-1}$	$6.050 \times 10^{-2}$
[0.05-0.10]	$1.776 \times 10^{-1}$	$8.135 \times 10^{-3}$	$-2.558 \times 10^{-1}$	$6.782 \times 10^{-2}$
[0.10-0.15]	$1.753 \times 10^{-1}$	$8.069 \times 10^{-3}$	$-2.770 \times 10^{-1}$	$6.655 \times 10^{-2}$
[0.15-0.20]	$1.794 \times 10^{-1}$	$8.041 \times 10^{-3}$	$-2.334 \times 10^{-1}$	$6.965 \times 10^{-2}$
[0.20-0.25]	$1.818 \times 10^{-1}$	$7.770 \times 10^{-3}$	$-1.786 \times 10^{-1}$	$7.066 \times 10^{-2}$

TABLE 6: Fit parameters of Eq.(139) for  $H(e, e'\gamma)X$  events with the proton prediction in core region of proton array.



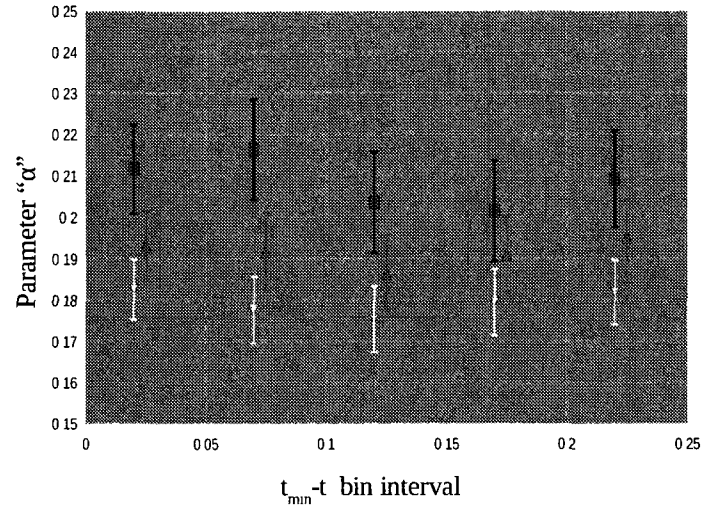


FIG. 86: Fit parameter  $\alpha$  of Eq. (139) as a function of  $t_{min} - t$ . The squares denotes the  $H(e, e'\gamma p)$  events with detected proton in the exclusive predicted block, the up pointing triangle denotes  $H(e, e'\gamma p)$  events in the group of nine, and the down pointing triangle denotes  $H(e, e'\gamma)X$  events with the proton prediction in core region of proton array.

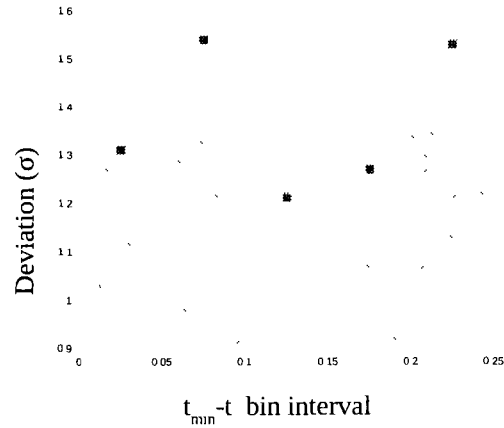


FIG. 87: The deviation of triple coincidence BSA measurements from the double coincidence BSA measurements as a function of  $t_{min} - t$  bin.

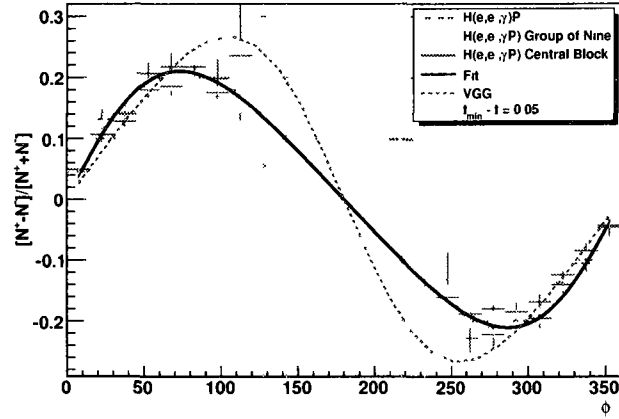


FIG. 88: VGG calculation for triple coincidence beam spin asymmetry. The  $t_{min} - t$  bin interval is  $t_{min} - t \in [0.00, 0.05] \text{ GeV}^2$ .

position is correlated with denominator  $\cos$  term. the numerator  $\sin$  behavior is confirmed with VGG calculation.

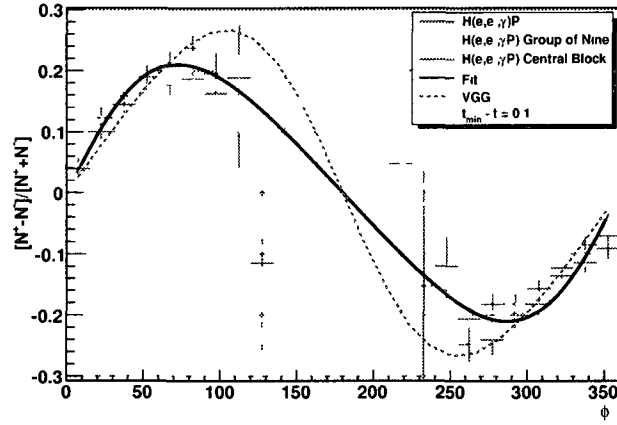


FIG. 89: VGG calculation for triple coincidence beam spin asymmetry. The  $t_{min} - t$  bin interval is  $t_{min} - t \in [0.05, 0.10] \text{ GeV}^2$ .

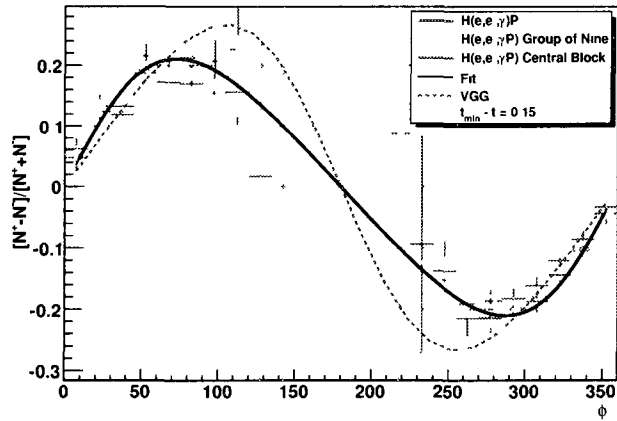


FIG. 90: VGG calculation for triple coincidence beam spin asymmetry. The  $t_{min} - t$  bin interval is  $t_{min} - t \in [0.10, 0.15] \text{ GeV}^2$ .

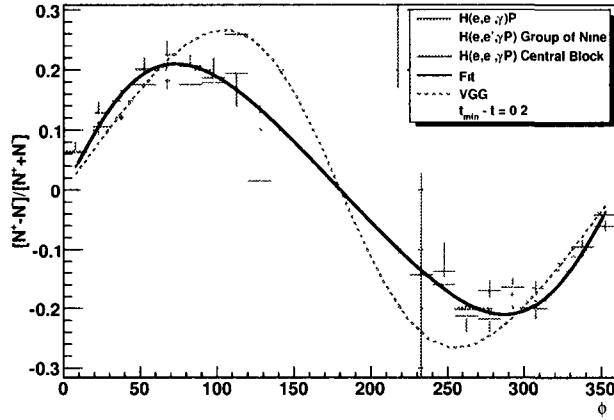


FIG. 91: VGG calculation for triple coincidence beam spin asymmetry. The  $t_{min} - t$  bin interval is  $t_{min} - t \in [0.15, 0.20] \text{ GeV}^2$ .

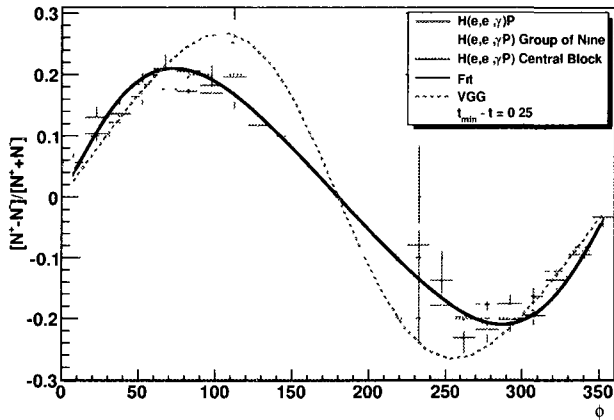


FIG. 92: VGG calculation for triple coincidence beam spin asymmetry. The  $t_{min} - t$  bin interval is  $t_{min} - t \in [0.20, 0.25] \text{ GeV}^2$ .

## CHAPTER IX

### POLARIZED DVCS OBSERVABLES

So far the discussed aspects of electro-production of real photon process are related to polarized beam and unpolarized target. Whereas experimental Hall A at JLab has the capacity to conduct experiments with polarized  $^3\text{He}$  target. In this chapter, the feasibility of DVCS with polarized target simulated asymmetry results will be discussed.

Certain types of GPDs such as  $E$  types are accessible only with polarized observables. Moreover, the sensitivity of asymmetry to all types of GPDs is improved with polarized observables. The polarized observables will be discussed in and presented in two different observable types;

- Double Spin Observables,
- Target Spin Observables.

#### IX.1 CROSS SECTIONS WITH POLARIZED AND ANGULAR DEPENDENCE

##### IX.1.1 Interference of Bethe-Heitler and DVCS Amplitudes

$$I = \frac{\pm e^6}{x_B y^3 t P_1(\phi) P_2(\phi)} \left\{ c_0^I + \sum_{n=1}^3 [c_n^I \cos(n\phi) + s_n^I \sin(n\phi)] \right\} \quad (140)$$

For the phenomenology of GPDs, the interference term (see II.5.2 and Eq. 140) is the most interesting quantity since it is linear in CFFs. This simplifies their disentanglement from experimental measurements. Among the Fourier harmonics formed in Eq. (140) the twist-2 case of  $s_1^I \sin(\phi)$  will be discussed to scrutinize the polarized observables.

Longitudinal polarized target:

$$s_{1,LP}^I = 8\Lambda K \{2 - 2y + y^2\} \Im m C_{LP}^I. \quad (141)$$

Transversely polarized target:

$$s_{1,TP}^I = \frac{8M\sqrt{1-y}}{Q} \times \left[ \cos(\varphi) \{2 - 2y + y^2\} \Im m C_{TP+}^I + \sin(\varphi) \{\lambda y(2 - y)\} \Re e C_{TP-}^I \right] \quad (142)$$

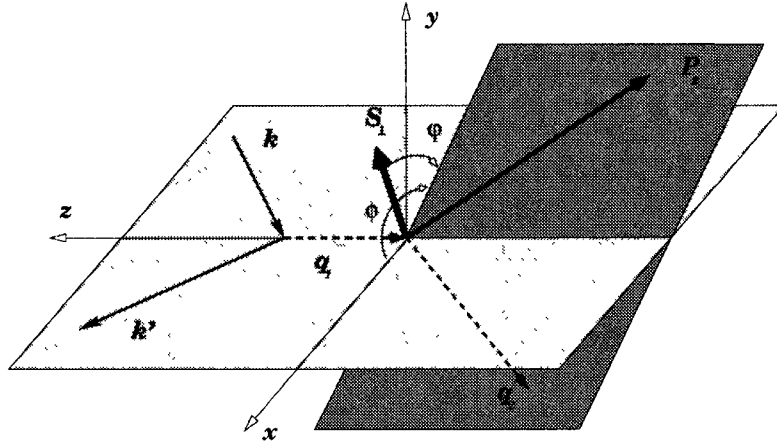


FIG. 93: The kinematics of the electro-production in the target rest frame. The  $z$  direction is chosen counter-along the three-momentum of the incoming virtual photon. The electron three momenta from the lepton scattering plane, while the recoiled proton and outgoing real photon define the hadron scattering plane. In this reference system the azimuthal angle of the scattered lepton is  $\phi_l = 0$ , while the azimuthal angle between the lepton plane and the recoiled proton momentum is  $\phi_N = \phi$ . When the hadron is transversely polarized (in this reference frame)  $S_{\perp} = (0, \cos \Phi, \sin \Phi, 0)$ , the angle between the polarization vector and the scattered hadron is denoted as  $\varphi = \Phi - \phi_N$ .

### IX.1.2 Angular Harmonics in terms of GPDs

The Fourier coefficients introduced in IX.1.1 are expressed in terms of the coefficients  $C$ . They depend on GPDs, integrated over the momentum fraction, and are functions of the kinematical variables  $x_B$ ,  $\Delta^2$ , and  $Q^2$ . For the harmonics involving  $H$ ,  $E$ ,  $\tilde{H}$  and  $\tilde{E}$ -type GPDs:

$$C_{unp}^I = F_1 \mathcal{H} + \frac{x_B}{2 - x_B} (F_1 + F_2) \mathcal{H} - \frac{\Delta^2}{4M^2} \mathcal{E}, \quad (143)$$

$$C_{LP}^I = \frac{x_B}{2 - x_B} (F_1 + F_2) \left( \mathcal{H} + \frac{x_B}{2} \mathcal{E} \right) + F_1 \tilde{\mathcal{H}} - \frac{x_B}{2 - x_B} \left( \frac{x_B}{2} F_1 + \frac{\Delta^2}{4M^2} F_2 \right) \tilde{\mathcal{E}}, \quad (144)$$

$$\begin{aligned} C_{TP+}^I = (F_1 + F_2) & \left\{ \frac{x_B^2}{2 - x_B} \left( \mathcal{H} + \frac{x_B}{2} \mathcal{E} \right) + \frac{x_B \Delta^2}{4M^2} \mathcal{E} \right\} - \frac{x_B^2}{2 - x_B} F_1 \left( \tilde{\mathcal{H}} + \frac{x_B}{2} \tilde{\mathcal{E}} \right) \\ & + \frac{\Delta^2}{4M^2} \left\{ 4 \frac{1 - x_B}{2 - x_B} F_2 \tilde{\mathcal{H}} - \left( x_B F_1 + \frac{x_B^2}{2 - x_B} F_2 \right) \tilde{\mathcal{E}} \right\}, \end{aligned} \quad (145)$$

$$\begin{aligned} C_{TP-}^I = \frac{1}{2 - x_B} & \left( x_B^2 F_1 - (1 - x_B) \frac{\Delta^2}{M^2} F_2 \right) \mathcal{H} \\ & + \left\{ \frac{\Delta^2}{4M^2} \left( (2 - x_B) F_1 + \frac{x_B^2}{2 - x_B} F_2 \right) + \frac{x_B^2}{2 - x_B} F_2 \right\} \mathcal{E} \\ & - \frac{x_B^2}{2 - x_B} (F_1 + F_2) \left( \tilde{\mathcal{H}} + \frac{\Delta^2}{4M^2} \tilde{\mathcal{E}} \right). \end{aligned} \quad (146)$$

The four CFFs  $\mathcal{F} = \{\mathcal{H}, \mathcal{E}, \tilde{\mathcal{H}}, \tilde{\mathcal{E}}\}$  are integrals of GPDs (Eq.67, 68, 69) such as,

$$\Im m \mathcal{H} = \pi \sum_q e_q^2 \{ H^q(\xi, \xi, t) - H^q(-\xi, \xi, t) \} \quad (147)$$

of which details can be seen in II.5. Moreover, in the case of the four CFFs  $\mathcal{F} = \{\mathcal{H}, \mathcal{E}, \tilde{\mathcal{H}}, \tilde{\mathcal{E}}\}$  there are eight observables given by the first harmonics  $\cos(\phi)$  and  $\sin(\phi)$  of the interference term (see Eq. 140) which are accessible away from the kinematical boundaries in polarized beam and target experiments. Thus, experiments with both longitudinally and transversely polarized target can measure all eight Fourier coefficients  $c_{1,\Lambda}^I$  and  $s_{1,\Lambda}^I$  and also  $\Re/\Im m C_\Lambda^I$  with  $\Lambda = \{unp, LP, TP_x, TP_y\}$  Moreover, the Eq. (144), (146) and (145) are more sensitive to all type of GPDs than

the unpolarized case (143). By knowing these  $\mathcal{C}$  functions, they can be inverted to obtain the CFFs:

$$\mathcal{H} = \Gamma \left\{ \left[ \left( 2 - x_B + \frac{4x_B^2 M^2}{(2 - x_B)\Delta^2} \right) F_1 + \frac{x_B^2}{2 - x_B} F_2 \right] \mathcal{C}_{unp}^I \right\} + \Gamma \left\{ -(F_1 + F_2) \left[ x_B \mathcal{C}_{LP}^I + \frac{2x_B^2 M^2}{(2 - x_B)\Delta^2} (x_B \mathcal{C}_{LP}^I - \mathcal{C}_{TP+}^I) \right] + F_2 \mathcal{C}_{TP-}^I \right\} \quad (148)$$

$$\mathcal{E} = \Gamma \left( 4 \frac{1 - x_B}{2 - x_B} F_2 - \frac{4M^2 x_B^2}{(2 - x_B)\Delta^2} F_1 \right) \mathcal{C}_{unp}^I + \Gamma \left[ \frac{4x_B M^2}{(2 - x_B)\Delta^2} (F_1 + F_2) (x_B \mathcal{C}_{LP}^I - \mathcal{C}_{TP+}^I) + \frac{4M^2}{\Delta^2} F_1 \mathcal{C}_{TP-}^I \right] \quad (149)$$

$$\tilde{\mathcal{H}} = \Gamma \left[ (2 - x_B) F_1 \mathcal{C}_{LP}^I - x_B (F_1 + F_2) \mathcal{C}_{unp}^I + \left( \frac{2x_B M^2}{\Delta^2} F_1 + F_2 \right) \right] \times (x_B \mathcal{C}_{LP}^I - \mathcal{C}_{TP+}^I) \quad (150)$$

$$\tilde{\mathcal{E}} = \Gamma \left[ \frac{4M^2}{\Delta^2} (F_1 + F_2) (x_B \mathcal{C}_{unp}^I + \mathcal{C}_{TP-}^I) \right] + \Gamma \left\{ \left( 4 \frac{1 - x_B}{x_B} F_2 - \frac{4x_B M^2}{\Delta^2} F_1 \right) \mathcal{C}_{LP}^I - \frac{4(2 - x_B) M^2}{x_B \Delta^2} F_1 \mathcal{C}_{TP+}^I \right\} \quad (151)$$

where

$$\Gamma = \frac{2 - x_B}{1 - x_B} \frac{1}{4(F_1^2 - \frac{\Delta^2}{4M^2} F_2^2)(1 - \frac{\Delta_{unp}^2}{\Delta^2})}$$

As discussed in II.5, GPDs can be extracted by utilizing the CFF as in Eq. (67), (68), (69), or (147). By the same token, by using the Eq.(148), (149), (150) and (151) one can test the sensitivity of each CFFs to polarized angular harmonics and GPDs as well.

## IX.2 VGG CALCULATION OF GPDS

GPD studies are model dependent and among the existing models, in this study I used the model presented by Vanderhaeghen, Guichon, Guidal (VGG) [33] and Goeke, Polyakov, Vanderhaeghen [32]. A re-parametrization of the  $x$  and  $\xi$  dependence of GPDs introduced [89] in terms of the momentum fractions  $\beta$  of  $P^+$  and  $\alpha$  of  $\Delta^+$  which allows to re-write the initial and final parton + components of momentum as

$$\beta P^+ \mp (1 \pm \alpha) \Delta^+ / 2. \quad (152)$$



Therefore,

$$GPD_{f,DD}(x, \xi, t) = \int_{-1}^{+1} d\beta \int_{-1+|\beta|}^{1-|\beta|} d\alpha \delta(x - \beta - \alpha\xi) F_f(\beta, \alpha, t) \quad (153)$$

and the  $H$ ,  $E$  and  $\tilde{H}$  Double Distributions parametrization can be written respectively:

$$F_f(\beta, \alpha, 0) = h(\beta, \alpha) q_f(\beta); \quad (154)$$

$$F_f(\beta, \alpha, 0) = h(\beta, \alpha) \frac{\kappa_f q_f(\beta) (1 - \beta)^{\nu_f}}{A_f} \quad (155)$$

$$F_f(\beta, \alpha, 0) = h(\beta, \alpha) \Delta q_f(\beta); \quad (156)$$

where  $\kappa_f$  is the flavor anomalous magnetic moment of the proton. The profile function  $h$  is introduced as:

$$h(\beta, \alpha) = \frac{\Gamma(2b + 2)}{2^{2b+1} \Gamma(b + 1)} \frac{[(1 - |\beta|)^2 - \alpha^2]^b}{(1 - |\beta|)^{2b+1}} \quad (157)$$

Here the parameter  $b$  characterizes the strength of the  $\xi$  dependence of the GPD.  $b$  is a free parameter for the valance quark contribution and for the sea/anti-quark contribution to the GPD, which can be used, for example, as fit parameters in the extraction of GPDs from the hard electroproduction observables. The DD form or Eq. (153) ensures the polynomiality conditions, however, D-term must be included in this model to produce the highest  $\xi^{N+1}$  power for  $x^N$  moment. Therefore, E type GPD can be written as:

$$E^q(x, \xi, t) = E_{DD}^{qval}(x, \xi, t) + B^q \frac{\Gamma(2b + 2)}{2^{2b+1} \Gamma^2(b + 1)} \frac{1}{\xi} \theta(\xi - |x|) D\left(\frac{x}{\xi}, t\right) \quad (158)$$

where the first term is the  $DD$  part originating from the valance contribution to  $e^q$  while the second term originates from sea contribution to  $e^q$ . The quark contributions to the proton spin  $J_u$  for up quarks, and  $J_d$  for down quarks are introduced in to the model via the parametrization of  $e^q$  in [32]:

$$\begin{aligned} e^u &= A^u u_{val}(x) + B^u \delta(x), \\ e^d &= A^d d_{val}(x) + B^d \delta(x), \\ e^s(x) &= 0 \end{aligned} \quad (159)$$

where the parameters  $A^u$ ,  $A^d$  are related to  $J^u$  and  $J^d$  as

$$A^q = \frac{2J^q - M_2^q}{M_2^{qval}}, \quad (160)$$

where

$$M_2^q = \int_0^1 dx x [q(x) + \bar{q}(x)] \quad (161)$$

and

$$M_2^{q_{val}} = \int_0^1 dx x q_{val}(x) = \int_0^1 dx x [q - \bar{q}]. \quad (162)$$

The  $B^u$  and  $B^d$  in Eq.159 can be written as

$$B^u = 2 \left[ \frac{1}{2} \kappa^u - \frac{2J^u - M_2^u}{M_2^{u_{val}}} \right]$$

$$B^d = \kappa_d - \frac{2J^d - M_2^d}{M_2^{d_{val}}}. \quad (163)$$

which allows  $J_{u,d}$  to enter into the  $E$  GPD (Eq. (158)) as parameters in the parametrization of Eq.(159). Therefore, such a parametrization as in Eq.(159) can be used to scrutinize the sensitivity of hard electroproduction observables on  $J_u$  and  $J_d$ . The physical interpretation of the sea quark part of  $e^q(x)$  in Eq. (159) can be understood as being due to the vector meson exchange because of  $e^q(x)$  in Eq.(159) is normalized to  $\kappa^q$ . As a consequence, in this calculation, the term  $b$  in profile function (Eq.(157)) is taken as  $b = 1$  to be in consistent to the physical interpretation of Eq. (159).

The summary of this VGG calculation is:

- $\xi$  dependent parametrization with MRST02 NNLO distribution at  $\mu^2 = 1 \text{ GeV}^2$ ,
- value for the power  $b$  in the profile function for the valance contribution to  $H$  equals to 1,
- value for the power  $b$  in the profile function for the sea contribution to  $H$  equals to 1,
- model for the  $t$  dependence of the GPD  $H$ 
  - R2 Regge ansatz model ( $t$ -dependence in DDs)[32],
- The  $\alpha = 1.098 \text{ GeV}^2$ ,
- Evaluated GPD  $E$ : Double distribution contribution + D-term contribution model for the double distribution part of the GPD  $E$

Kin.	$Q^2$ ( $GeV^2$ )	$k_2^{electron}$ ( $GeV$ )	$t$ ( $GeV^2$ )	$x_B$
1	3.05	8.8	0.213/0.313	0.36
2	4.8	8.8	0.437/0.537	0.5
3	4.5	11	0.217/0.317	0.36
4	6.5	11	0.450/0.550	0.5

TABLE 7: Kinematics for VGG calculation of polarized DVCS observables. Calculation is performed for each kinematics for two different  $t$  values shown in table. Besides, for each kinematical settings calculations are repeated for different  $J_u$  and  $J_d$  values.

– valence quark + VM contribution

- the  $\pi_0$  pole contribution included
- $\tilde{H}$  included,
- $J_u$  value for the calculation is 0.3,
- and two different  $J_d$  values are used: 0 and  $-0.3$

### IX.2.1 Kinematics

The kinematics that the observables calculated are in line with the JLab 12 -GeV upgrade programs. The kinematics can be seen in Table -7. In addition the kinematics, the following polarization, acceptance and luminosity are used in the calculation

- Target polarization: 70%
- Beam polarization: 80%
- HRS acceptance
  - $\Delta\Omega_e \sim 6 \times 10^{-3}$  sr
  - $\Delta k' \sim 0.08k'$
- Neutron luminosity
  - $10^{37}(\frac{1}{cm^2 \cdot sec})$
  - 7 days for each polarization

The calculation along with the polarization of  ${}^3\text{He}$  is performed by the VGG simulation method written M.Guidial. The polarization of  ${}^3\text{He}$  is calculated for each kinematics listed in Table-7 by the polarized observables for both neutron and proton. Then, by using

$$85\% n_{pol} - 2.8\% p_{pol} \quad (164)$$

the  ${}^3\text{He}$  polarization observables are calculated.

### IX.3 RESULTS

#### IX.3.1 Cross Sections

The presented cross section results here are unraveled through two observables. First one is the target-spin cross section difference ( $TS$ ), with unpolarized electron beam. This is completely analogous to the helicity dependent cross section of 14. The BH cross section cancels and one is left with the leading and higher-twist contributions from the interference term and power suppressed effects from the squared DVCS amplitude.

Second one is double electron-nucleon spin dependent cross section ( $DS$ ) where the target and the electron beam is polarized.

Each histogram includes, Neutron contribution to the displayed mechanism, and calculated  ${}^3\text{He}$  cross section. The theory calculation is displayed by solid line. The scattered distribution with error bars are generated by a random Gaussian to the calculated theory value at each bin. is not protected from the contributions of the BH process and DVCS. Thus, for  $DS$  figures the BH contributions are also displayed along with the cross sections.

The transversely target polarization along the  $x$  axis,  $TP_x$  for kinematics-one can be seen in Fig. (94), and the  $TP_y$  are displayed in Fig. (95). The longitudinally polarized target results are displayed in Fig. (96). (For the orientation of  $x$ ,  $y$  and  $z$  please see Fig.93.)

#### IX.3.2 Difference in Cross Section

The cross section difference for two different  $J_u$  and  $J_d$  value combination,

$$\left( \frac{d^4\sigma}{d^4\Phi} \right)_{[j_u, j_d]=[0.3, 0.0]} - \left( \frac{d^4\sigma}{d^4\Phi} \right)_{[j_u, j_d]=[0.3, -0.3]}, \quad (165)$$

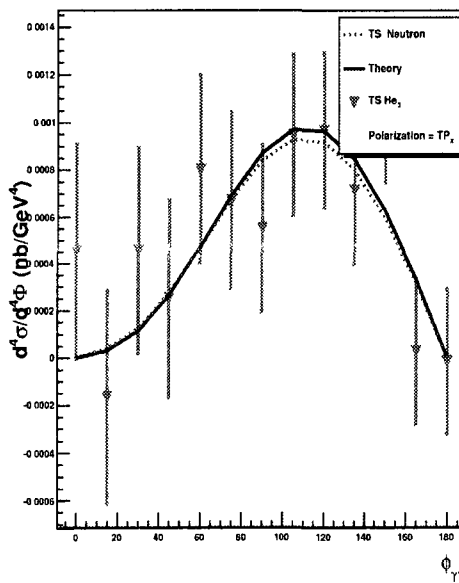
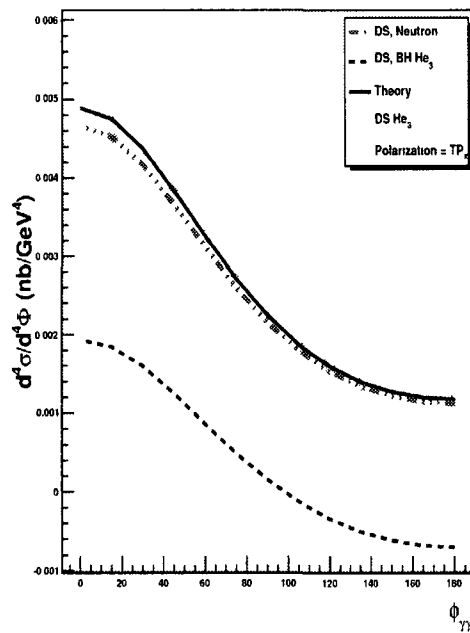


FIG. 94: Calculated cross section for target polarization of  $TP_x$ . The upper histogram displays the  $DS$  and bottom one displays  $TS$ .

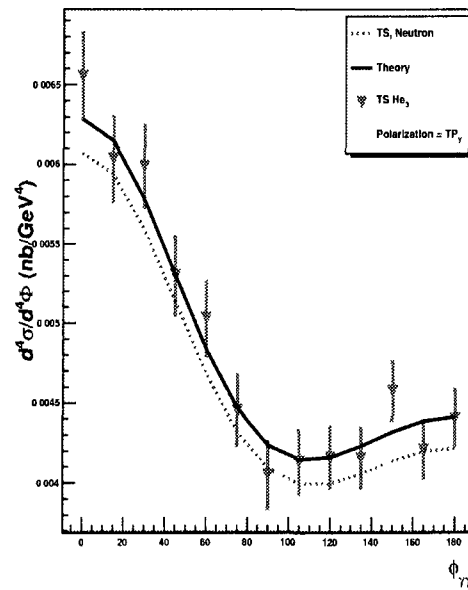
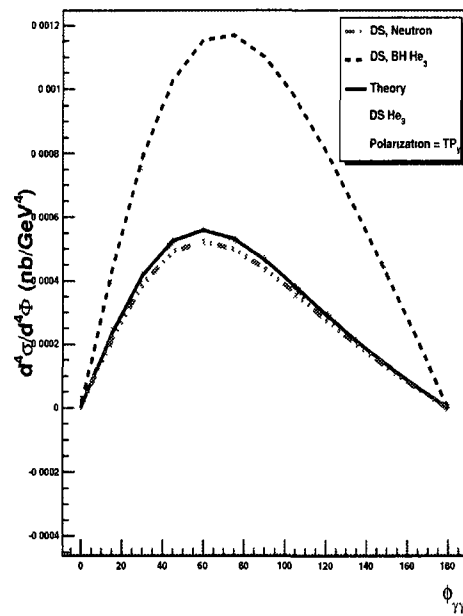


FIG. 95: Calculated cross section for target polarization of  $TP_y$ . The upper histogram displays the  $DS$  and bottom one displays  $TS$ .

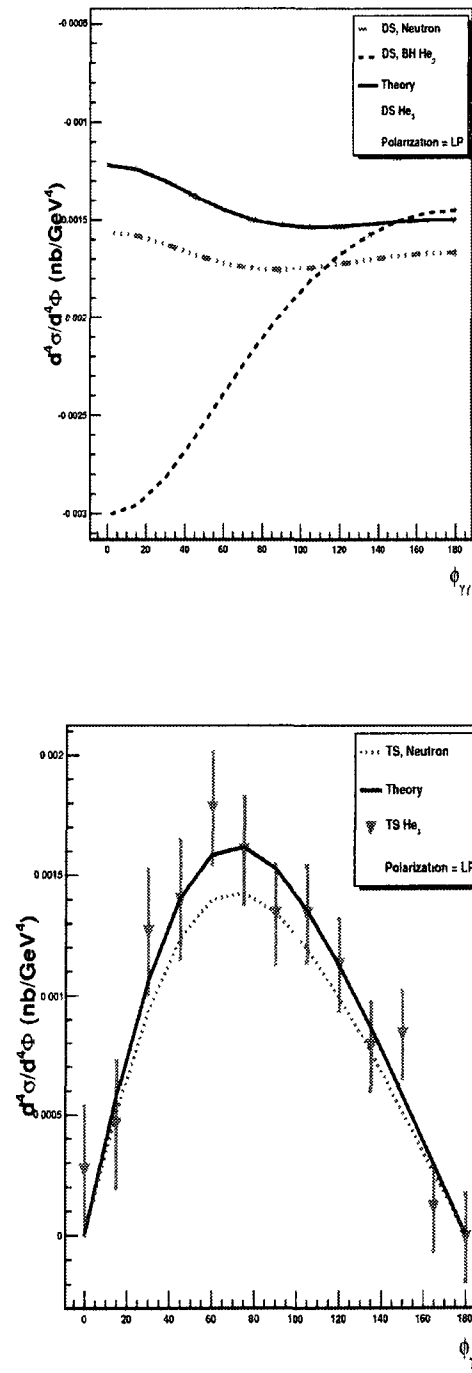


FIG. 96: Calculated cross section for target polarization of  $LP$ . The upper histogram displays the  $DS$  and bottom one displays  $TS$ .

is used to study the sensitivity to E-type GPD. The manifestation of this sensitivity emerged in studying the cross section for different values of  $J_u$  and  $J_d$ .

### IX.3.3 Discussion

Based on the presented VGG GPD calculation in this study the sensitivity to  $\Delta J_d = 0.3$  of

- $\sim 4.5\sigma$  for  $LP$  (longitudinally polarized target)
- $\sim 2\sigma$  for  $TP_x$  (transversely polarized target along the  $x$  axis)
- $\sim 8\sigma$  for  $TP_y$  (transversely polarized target along the  $y$  axis)

For the unpolarized or longitudinally polarized target higher harmonics [34] are suppressed by powers of  $K$  (Eq.64). In the case of transversely polarized target, it is observed that higher twist harmonics are suppressed by one power of  $K$  in the interference term. As discussed earlier, experiments with both longitudinally and transversely polarized target can measure all eight Fourier coefficients  $c_{1,\Lambda}^I$  and  $s_{1,\Lambda}^I$ . Because of the explicit expressions in the Fourier coefficients the magnitude of the asymmetry varies. For example, in Eq. 148 the main terms are  $C_{unp}^I$  and  $C_{LP}^I$ . One can observe that the CFF  $\mathcal{H}$ , dominating the  $C_{unp}^I$  at moderate and small  $x_B$ , now enters the amplitude with an additional power of  $x_B$  in  $C_{LP}^I$ . Thus, it becomes parametrically of the same order as the parity-odd CFF  $\tilde{\mathcal{H}}$ :  $|\tilde{\mathcal{H}}| \sim x_B |\mathcal{H}|$ . Thus, both of them play a distinctive role in building up the nucleon-spin asymmetry which is displayed in the bottom histogram in Fig. (96).

As discussed earlier, the  $DS$  is not protected from BH processes. In fact, this can be seen in Fig. (94 - 96) where the BH cross section alone generate a large asymmetry (displayed as dashed curve). However, due to relatively good knowledge of the BH process, subtracting it from data should not introduce any issue. In the VGG study that is performed here, varying the  $J_d$  value from 0.0 to 0.3 changes the observables. However, this modest sensitivity calls for precise calculation, measurements as well as detailed studies of higher-twist effects and NLO corrections.



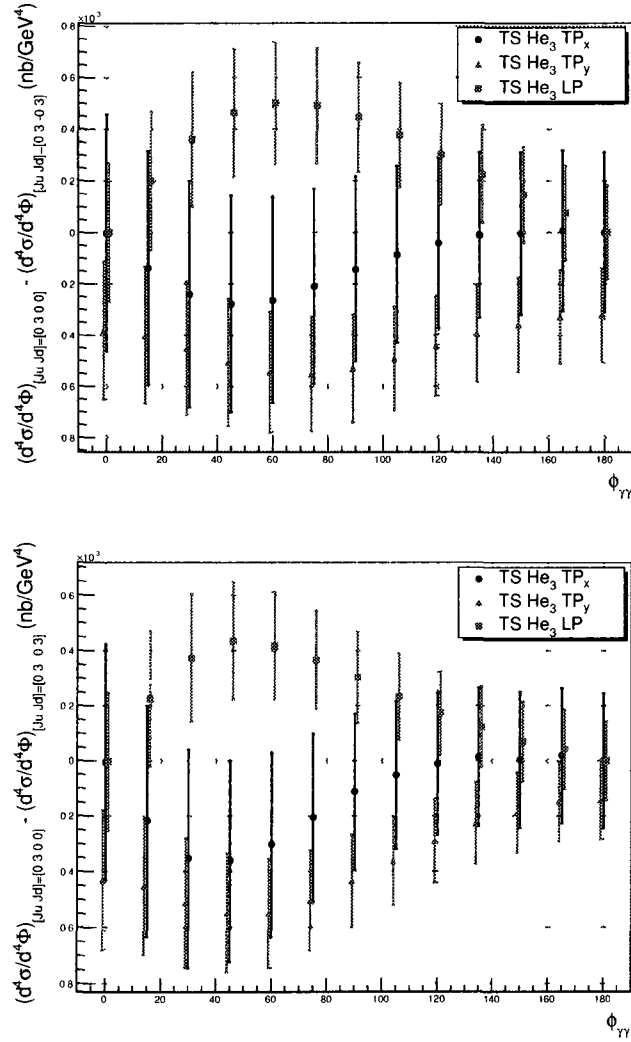


FIG. 97: Kinematics-1 difference in cross section. The upper histogram  $t_{min} - t$  value is  $0.05 \text{ GeV}^2$ , and the bottom histogram's  $t_{min} - t$  value is  $0.15 \text{ GeV}^2$

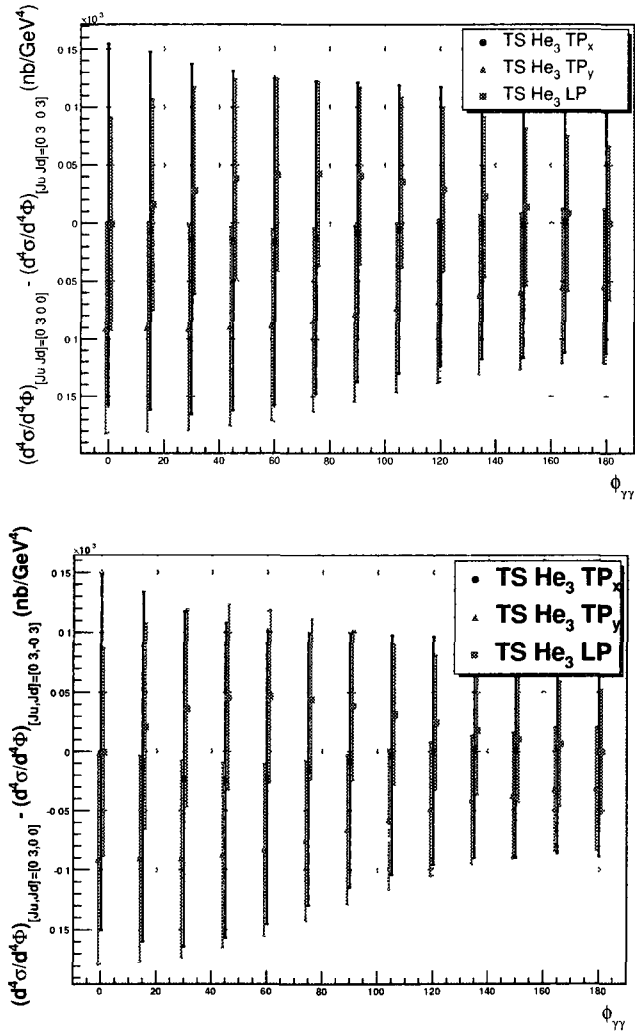


FIG. 98: Kinematics-2 difference in cross section. The upper histogram  $t_{min} - t$  value is  $0.05 \text{ GeV}^2$ , and the bottom histogram's  $t_{min} - t$  value is  $0.15 \text{ GeV}^2$

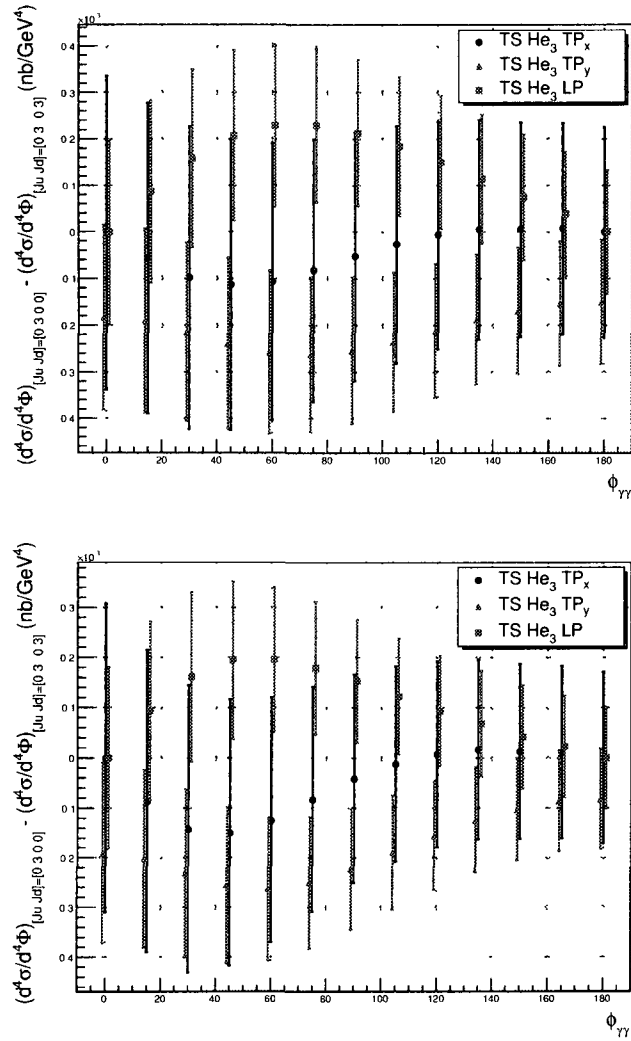


FIG. 99: Kinematics-3 difference in cross section. The upper histogram  $t_{min} - t$  value is  $0.05 \text{ GeV}^2$ , and the bottom histogram's  $t_{min} - t$  value is  $0.15 \text{ GeV}^2$

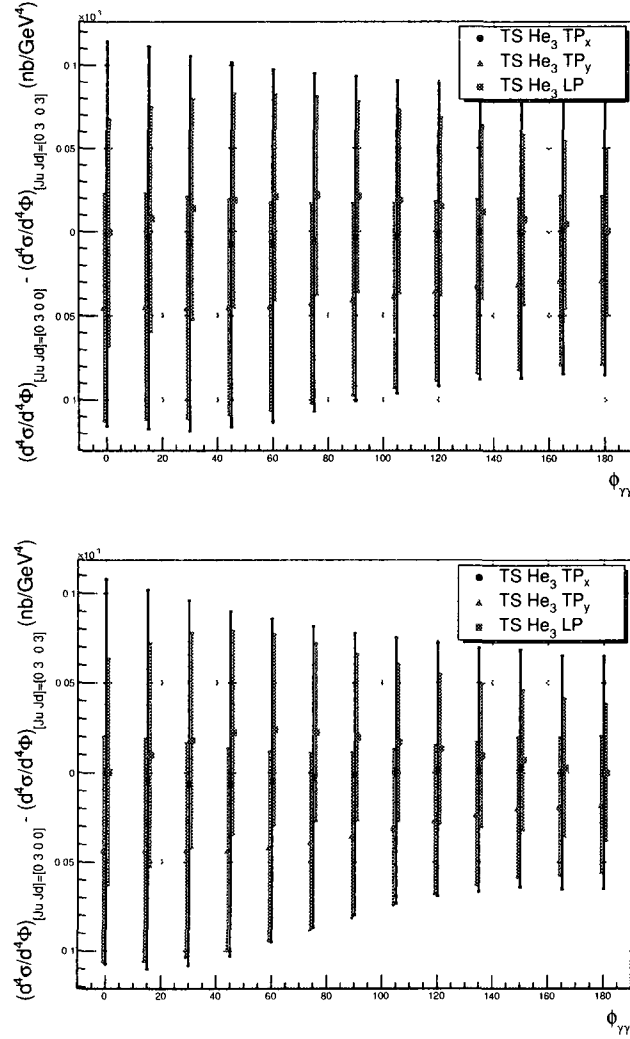


FIG. 100: Kinematics-4 difference in cross section The upper histogram  $t_{min} - t$  value is  $0.05 \text{ GeV}^2$ , and the bottom histogram's  $t_{min} - t$  value is  $0.15 \text{ GeV}^2$

## CHAPTER X

### SUMMARY

The analysis presented in this thesis is the triple coincidence  $H(e, e'\gamma p)$  beam spin asymmetry measurement of a dedicated deeply virtual Compton scattering experiment in Jefferson Laboratory experimental Hall A.

The experiment conducted with the standard experimental Hall A equipment along with two dedicated DVCS detectors. The 5.75 GeV beam was incident on a 15 cm liquid  $H_2$  target. The maintained luminosity was  $10^{37}/\text{cm}^2/\text{s}$  with 76% beam polarization. The scattered electrons detected in high resolution spectrometer. The emitted real photon detected in an electromagnetic calorimeter made of  $PbF_2$  crystals whose front face was located 1.1 m from the target chamber center. The calibration results show a  $PbF_2$  resolution of 2.4% and 2 mm in transverse position ( $1\sigma$ ).

In addition to electromagnetic calorimeter, a proton array of 100 plastics scintillators was built at Old Dominion University to detect the recoil proton. The proton array has challenges in many aspects such as high radiation background, having low energy recoil particles detected, not fully simulated and kinematical constraints. Thus, in the [72], the proton array was used to evaluate possible contamination of inclusive events to the exclusive region that was studied in.

On the other hand, the proton array in the context of this thesis is used to utilize the triple coincidence events to test the exclusivity by conducting  $M_X^2$  study and beam spin asymmetry measurements. The presented  $M_X^2$  spectra first led to recalibrate the calorimeter which dominates the  $M_X^2$ . With the performed calibration, asymmetries extracted for several 5 bins in  $t_{min} - t$  and 24 bins azimuthal angle. The extraction of asymmetry relies on the fitting method. The fitting function used in this analysis is  $BSA_{fit} = \frac{\alpha \sin \phi}{1 + \beta \cos \phi}$ . The asymmetry amplitudes vary in each bin of  $t_{min} - t$  which shows the correlation between the BSA and the exclusivity of the data. The average deviation of triple coincidence asymmetry from double coincidence asymmetry is  $1.3 \sigma$ . For the  $t_{min} - t$  bins that correspond to the middle columns in Fig. 73 have  $1.2 \sigma$  deviation while the first bin in  $t_{min} - t$  for example, has a deviation of  $1.5 \sigma$ .

The concept of GPDs has led to completely new methods of spatial imaging of the nucleon. The scrutinized studies in GPDs led to acquire vast amount of knowledge which have entailed mature theoretical and experimental framework about GPDs.

Unifying the concepts of parton distributions and of hadronic form factors, GPDs contain a wealth of information about how quarks and gluons form the hadrons. Moreover, GPDs allow to quantify how the orbital motion of quarks in the nucleon contributes to the nucleon spin which is revealed via Ji's sum rule that is nothing but second moment of GPDs. These widely recognized encoded physics are the key objectives of nuclear physics of next decade, and, in fact these are among the key justification argument for the Jefferson Laboratory energy upgrade to 12 GeV.

Among the utilized exclusive processes, DVCS, the cleanest process to access the GPDs, maintains an important role in the future of GPD phenomenology. The recently performed Jefferson Laboratory DVCS experiments along with the approved 12 GeV experiment will provide a stringent test of factorization, and quantify the contribution of higher twist terms. Moreover, the DVCS data will be expanded to a  $x_B$  range of 0.36 to 0.6 where the existing data is limited to certain  $X_B$  values, such as 0.36.

In this regard, in this thesis the sensitivity of polarized DVCS observables for E-type GPDs by VGG calculation method for the 12 GeV kinematics settings with polarized  ${}^3\text{He}$ . The cross section extracted from polarized targets show sensitivity to  $J_d$  which ultimately give access to E-type GPD. The sensitivity varies in between  $2\sigma$  to  $8\sigma$  depending on the polarization of the target. These observables are not only sensitive to E-type GPD but also improves the sensitivity to other GPDs which is accessible with unpolarized targets. Thus, an initial conclusion would be that polarized  ${}^3\text{He}$  target experiments will be the core concept in the next generation DVCS experiments in experimental Hall A at Jefferson Laboratory.

## BIBLIOGRAPHY

- [1] B.R. Martin & G.Shaw, Particle Physics Second Edition (John Wiley & Sons) (2002).
- [2] R.W. McAllister & R. Hofstadter, Phys Rev. **102** (1956) 851.
- [3] R.P. Feynman, Photon-Hadron Interactions, (Addison-Wesley) (1989).
- [4] F.E. Close, An Introduction to Quarks and Partons (Academic Press) (1974).
- [5] O.Stern, Nature **132** (1933) 169.
- [6] A. W. Thomas, W. Weise, The Structure of the Nucleon, (Wiley-VCH) (2001).
- [7] M.N. Rosenbluth, Phys.Rev. **79** (1950) 615.
- [8] F. Halzen, A.D. Martin, Quarks & Leptons, (John Wiley & Sons) (1984).
- [9] A.V. Belitsky and A.V. Radyushkin, hep-ph/054030 v3 (2005).
- [10] J.D Bjorken, in Proceedings 3rd International Conference on Electron and Photon Interactions, Stanford, 1967.
- [11] J. D. Bjorken, E. A. Paschos Phys. Rev. **185**, 19751982 (1969).
- [12] H.W. Kendall, Nobel Lecture, Rev. Mod. Phys. **63** (1991) 597.
- [13] W. Panofsky, in Proceedings International Symposium on High Energy Physics,Vienna (1968).
- [14] R.P. Feynman, Phys. Rev. Lett. **23** (1969) 1415.
- [15] D.J. Gross and F. Wilczek Phys. Rev. D **8**, 3633 (1973).
- [16] H.D. Politzer, Phys. Rev. Lett. **30**, 1346 (1973).
- [17] Mueller D, Robaschik D, Geyer B, Dittes F M and Horejsi J 1994 Fortschr. Phys. **42** 101 (Preprint hep-ph/9812448).
- [18] X.Ji, Annu. Rev. Nucl. Part. Sci. 2004.54:413-50.

- [19] J.C. Collins, L Frankfurt and M Strikman 1997 Phys. Rev. **D56** 29823006 (Preprint hep-ph/9611433).
- [20] M. Garçon, An Introduction to Generalized Parton Distributions, Eur. Phys. J.A 18, 389-394 (2003).
- [21] X.D. Ji, Phys. Rev. **D55**, 7114 (1997), hep-ph/9609381.
- [22] X. Ji, J. Phys. G: Nucl. Part. Phys. **24** (1998) 1181-1205.
- [23] F.M. Dittes, et al. Phys. Lett. **209:325** (1988); Müller, et al. Fortschr. Phys. **42:101** (1994).
- [24] M. Diehl 2003 Phys. Rept. **388** 41277 Habilitation Thesis (Preprint hep-ph/0307382).
- [25] Radyushkin A. V. 1999 Phys. Rev. **D59** 014030 (Preprint hep-ph/9805342).
- [26] J. Ashman, et al., European Muon Collaboration, Phys. Lett. **B206** (1988) 364.
- [27] X.Ji Phys. Rev. Lett **78** (1997) **610** [hep-ph/9603249].
- [28] M. Burkardt, Phys. Rev **D 62** 071503 (2000) hep-ph/0005108.
- [29] M. Diehl, Eur. Phys, J. **C 25**, 223-232 (2002).
- [30] J.P. Ralston and B. Pire, hep-ph/0110075.
- [31] M. Diehl, Proceedings of the International Conference on QCD and Hadronic Physics, Beijing, China, 2005 hep-ph/0509170v1.
- [32] K. Goeke, V.M. Polyakov and M. Vanderhaeghen 2001 Prog. Part. Nucl. Phys. **47** 401515 (Preprint hep-ph/0106012)
- [33] M Vanderhaeghen, P.A.M.Guichon and M.Guidal 1999 Phys. Rev. **D60** 094017 (Preprint hep-ph/9905372).
- [34] A.V. Belitsky, D Müller, A Kischner, Nucl. Phys. **B629** 323 (2002).
- [35] M. Diehl, T. Gousset, B. Pire, J.P. Ralston, Phys. Lett. **B411** (1997)193.



- [36] A.V. Belitsky, D Müller, L. Niedermeier, A. Schäfer, Nucl. Phys. **B593** (2001)289.
- [37] A.V. Radyushkin, Phys. Lett. **B380**, 417 (1996), hep-ph/9604317.
- [38] A.V. Radyushkin, Phys. Lett. **B385**, 333 (1996), hep-ph/9605431.
- [39] W.D. Nowak, Deeply Virtual Compton Scattering: Results and Future, hep-ex/05030110 v1 2005.
- [40] A.V. Belitsky, D. Müller, 1998, Phys Lett **B417** 129.
- [41] X. Ji and J. Osborne, 1998, Phys rev **D58** 094018.
- [42] L. Mankiewicz et al., 1998, Phys Lett **B425** 186.
- [43] I. V. Anikin et al. , 2000, Phys Rev**D61** 071501.
- [44] A.V. Radyushkin and C. Weiss, 2001 Phys Rev **D63** 114012.
- [45] A.V. Belitsky et al. ,2002 Nucl Phys **B629** 323.
- [46] A. Freund, Phys. Lett **B472**, 412 (2000).
- [47] P. Kroll, M. Schürmann and P.A.M. Guichon, Nucl. Phys. **A598**, 435 (1996).
- [48] Guichon P.A.M., and M. Vanderhaeghen, Prog. Part. Nucl. Phys. **41**, 125 (1998).
- [49] J.P Ralston and B. Pire, Phys. Rev **D 66**, 111501 (2002).
- [50] A.V. Belitsky, D Müller, Nucl. Phys. **A711,118** (2002).
- [51] C. Adloff et al. (H1) 2001 Phys. Lett. **B517** 4758 (Preprint hep-ex/0107005).
- [52] A. Aktas et al. (H1) 2005 Eur. Phys. J. **C44** 111 (Preprint hep-ex/0505061).
- [53] F.D. Aaron et al. (H1) 2008 Phys. Lett. **B659** 796806 (Preprint 0709.4114).
- [54] S. Chekanov et al. (ZEUS) 2003 Phys. Lett. **B573** 4662 (Preprint hep-ex/0305028).
- [55] S. Chekanov et al. (ZEUS) 2008 (Preprint 0812.2517).

- [56] A.Airapetian et al. (HERMES) 2001 Phys. Rev. Lett. **87** 182001 (Preprint hep-ex/0106068).
- [57] S.Stepanyan et al. (CLAS) 2001 Phys. Rev. Lett. **87** 182002 (Preprint hep-ex/0107043).
- [58] A. Freund, M. McDermott, M. Strikman, Phys. Rev. **D67**, 036001 (2002).
- [59] N.Kivel, M.V. Polyokav, M.Vanderhaeghen, Phys.Rev. **D63**1114014 (2001).
- [60] A.V. Beltsky, A. Kirchner, D.Mueller, A.Schafer, Phys. Lett. **B510**, 117 (2001).
- [61] Carlos Muñoz Camacho, PhD thesis, University of Paris VI, France, 2005.
- [62] A. Airapetian et al. (HERMES) 2007 Phys. Rev. **D75** 011103 (Preprint hep-ex/0605108).
- [63] A. Airapetian et al. (HERMES) 2008 JHEP **06** 066 (Preprint 0802.2499).
- [64] A. Airapetian et al. (HERMES) 2010 JHEP **06** 019 (Preprint 1004.0177).
- [65] A. Airapetian et al. (HERMES) 2009 JHEP **11** 083 (Preprint 0909.3587).
- [66] B. Seitz (HERMES) 2004 Nucl. Instrum. Meth. **A535** 538541.
- [67] Hermes Results On Hard-Exclusive Processes And Prospects Using The New Recoil Detector in the Proceedings of 11th International Conference on Meson-Nucleon Physics and the Structure of the Nucleon (MENU 2007), Julich, Germany, 10-14 Sep 2007.
- [68] B.A. Mecking et al. (CLAS) 2003 Nucl. Instrum. Meth. **A503** 513553.
- [69] S. Chen et al. (CLAS) 2006 Phys. Rev. Lett. **97** 072002 (Preprint hep-ex/0605012)
- [70] Y. Roblin et al. (the Hall A DVCS Collaboration) 2000 E00-110 jLab Experiment E00-110, Deeply Virtual Compton Scattering at 6 GeV URL <http://hallaweb.jlab.org/experiment/DVCS/dvcs.pdf> .
- [71] Voutier E et al. (the Hall A DVCS Collaboration) 2003 E03-106 jLab Experiment E03-106, Deeply Virtual Compton Scattering on the Neutron URL <http://hallaweb.jlab.org/experiment/DVCS/dvcs.pdf> .

- [72] C. Munoz Camacho et al. (Jefferson Lab Hall A) 2006 Phys. Rev. Lett. **97** 262002 (Preprint nucl-ex/0607029).
- [73] M. Mazouz et al. (Jefferson Lab Hall A) 2007 Phys. Rev. Lett. **99** 242501 (Preprint 0709.0450).
- [74] E. Fuchey, Alexandre Camsonne, Carlos Munoz Camacho, Malek Mazouz, and the Hall A DVCS Collaboration Phys. Rev. C83:025201, 2011.
- [75] S.Ahmad, H. Honkanen, S. Liuti and S.K. Taneja 2007 Phys. Rev. **D75** 094003 (Preprint hep-ph/0611046).
- [76] M. Gockeler et al. (QCDSF) 2004 Phys. Rev. Lett. **92** 042002 (Preprint hep-ph/0304249).
- [77] D. Brommel et al. (QCDSF-UKQCD) 2007 PoS **LAT2007** 158 (Preprint 0710.1534).
- [78] P. Hagler et al. (LHPC) 2008 Phys. Rev. **D77** 094502 (Preprint 0705.4295).
- [79] W.A. Thomas 2008 Phys. Rev. Lett. **101** 102003 (Preprint 0803.2775).
- [80] X.F. Girod et al. (CLAS) 2008 Phys. Rev. Lett. **100** 162002 (Preprint 0711.4805).
- [81] M. Guidal 2008 Eur. Phys. J. **A37** 319332 (Preprint 0807.2355).
- [82] C. Munoz Camacho et al. (the Hall A DVCS Collaboration) 2007 JLab E07-007 complete Separation of Deeply Virtual Photon and Neutral Pion Electroproduction Observables of Unpolarized Protons.
- [83] M. Mazouz et al. 2008 JLab E08-025 Measurement of the Deeply Virtual Compton Scattering cross-section off the neutron.
- [84] V. Burkert, L. Elouadrhiri, M. Garcon, R. Niyazov, S. Stepanyan et al. (the CLAS Collaboration) 2006 JLab E06-003 Deeply Virtual Compton Scattering with CLAS at 6 GeV.
- [85] A. Biselli, L. Elouadrhiri, K. Joo, S. Niccolai et al. (the CLAS Collaboration) 2005 JLab E05-114 Deeply Virtual Compton Scattering at 6 GeV with polarized target and polarized beam using the CLAS detector.

- [86] Guidal M 2010 Phys. Lett. **B689** 156162 (Preprint 1003.0307).
- [87] F. Klein, A. Sandorfi et al. (the CLAS Collaboration) 2006 JLab E06-101.
- [88] H. Egiyan, X.F. Girod, K. Hafidi, S. Liuti, E. Voutier et al. (CLAS) 2008 Deeply Virtual Compton Scattering off  $^4\text{He}$  JLab E08-024.
- [89] N. d'Hose, E. Burtin, P.A.M Guichon and J. Marroncle 2004 Eur. Phys. J. **A19** Suppl14753.
- [90] J. Alcorn et al. Basic Instrumentation for Hall A at Jefferson Lab. Nucl. Instrum. Meth, A522:294-346, 2004.
- [91] M. Baylac et al. "First Electron Beam Polarization Measurement with a Compton Polarimeter at Jefferson Laboratory", Phys. Let. Vol B539, pp. 8-12, 2002.
- [92] A.V. Glamazdin et al. Electron Beam Møller Polarimeter at JLab Hall A, hep-ex/9912063v1, 1999.
- [93] A. Camasonne, PhD thesis, University Blaise Pascal, 2005.
- [94] F. Feinstein, Proc. 2002 Conference on advances in Photon Detection, France.
- [95] A. Chantelauze. Master degree thesis report. [www.jlab.org/astrid](http://www.jlab.org/astrid), 2004.
- [96] K.G. Fissum et al. Nucl. Instr. and Meth, **A 474** (2001) 108; Vertical drift chambers for the hall a high resolution spectrometers at Jefferson Lab, JLab-TN-00-016,2000
- [97] R.H. Wechsler, B.S. Thesis, Massachusetts Institute of Technology, 1996.
- [98] K.L. Brown, SLAC Report 75 (1970) revised edition, 1982, unpublished.
- [99] N. Liyanage, Optics calibration of the Hall A High Resolution Spectrometers using the new C++ optimizer, JLab-TN-02-012, 2002.
- [100] P.Y. Bertin, Internal Collaboration Report (2003).
- [101] M. Mazouz. P.Y. Bertin and E. Voutier, JLab Technical Note JLAB-05-042, 2005.
- [102] V. Breton, et al., Nucl. Inst. and Meth. **A362**, 478 (1995).

- [103] G. Laveissiere et al., Phys. Rev. Lett. **93**, 122001 (2004).
- [104] M. Rvachev, JLab Technical Note JLAB-01-055, (2001).
- [105] R. Brun et al., CERN Program Library W5015, (1990).
- [106] J. Roche et al., Phys. Rev. Lett. 85,708 (2000).
- [107] M. Vanderhaeghen, J.M. Friedrich, D. Lhuillier, D. Marchand, L. Van Hoorebeke, J. Van de Wiele, Phys Rev. C62, 025501 (2000).
- [108] J. Schwinger, Phys. Rev. 76, 790 (1949).
- [109] Y.S. Tsai, Phys. Rev. 122, 1898 (1961).
- [110] L.W. Mo, Y.S. Tsai, Rev. Mod. Phys. **41**, 205 (1969).
- [111] R. Burn, F. Rademakers, Nucl. Inst. and Meth. **A 389**, 81 (1997).
- [112] P.A.M Guichon, L. Mossé and M. Vanderhaeghen, Phys. Rev. (2003).
- [113] J. B. Birks, Theory and Practice of Scintillation Counting, Pergamon, 1967.

## VITA

Mustafa Canan  
Department of Physics  
Old Dominion University  
Norfolk, VA 23529

### Education

- Ph.D., Department of Physics Old Dominion University, Norfolk, Virginia, May, 2011
- M.S. , Department of Physics Old Dominion University, Norfolk, Virginia, May, 2006
- B.S. , Department of Physics Middle East Technical University, Ankara, Turkey, June 2003

### Talks & Conference

- APS 2011 April Meeting, Anaheim, California.
- HUGS 2005, Newport News, Virginia.

### Publications

- Exclusive Neutral Pion Electroproduction in the Deeply Virtual Regime. E. Fuchey et al. Phys.Rev.**C83**:025201,2011.
- Hard Photodisintegration of a Proton Pair. JLab Hall A Collaboration (I. Pomerantz et al.). Phys.Lett.**B684**:106-109,2010.